2024

Characterizing The Material Response Of The Passive Myocardium

Mehlil Ahmed
University of Central Florida

CHARACTERIZING THE MATERIAL RESPONSE OF THE PASSIVE MYOCARDIUM

by

MEHLIL AHMED
M.S. University of Central Florida, 2021

A dissertation submitted in partial fulfilment of the requirements
for the degree of Doctor of Philosophy
in the Department of Mechanical and Aerospace Engineering
in the College of Engineering and Computer Science
at the University of Central Florida
Orlando, Florida

Spring Term
2024

Major Professor: Luigi Perotti

ABSTRACT

Cardiovascular diseases remain a major public health concern worldwide, with heart failure emerging as a significant contributor to morbidity and mortality. Among heart failure cases, Heart Failure with preserved Ejection Fraction (HFpEF) presents a substantial clinical challenge due to its poor understanding and diagnostic complexity. Despite its prevalence, HFpEF lacks accurate diagnostic tools, hindering effective prognosis and therapy planning. This study addresses the knowledge gap surrounding HFpEF and diastolic dysfunction by focusing on the passive myocardial response during atrial systole, a critical yet understudied aspect of cardiac function. Current clinical measures, such as left ventricular ejection fraction, have limitations in assessing HFpEF and diastolic dysfunction due to their lack of specificity and focus on active myocardial contraction. Additionally, existing studies on myocardial deformation primarily evaluate ventricular systole, overlooking the passive response during atrial systole. This study proposes to characterize the passive myocardial response by investigating left ventricular deformation during atrial systole and integrating motion data with intraventricular pressure to estimate myocardial material properties. By enhancing our understanding of the passive myocardium, this research aims, in the future, to enable more accurate diagnosis and therapy planning for patients affected by diastolic dysfunction and HFpEF.

To my Ammu, Abbu, Baba, and Ma, for their endless support, wisdom, love, and encouragement.

To my elder sister and brother-in-law, for their resilience, intellect, and boundless love.

To my youngest sister, niece, and nephew, for their love, laughter, and joy.

To my husband, for being my confidant, and an eternal source of support, motivation, and encouragement through the challenges of graduate school and life.

"*Life is like riding a bicycle. To keep your balance, you must keep moving.*"

-Albert Einstein

ACKNOWLEDGMENTS

I would like to acknowledge my supervisor, Dr. Luigi Perotti. His continued support, motivation, and keen insight into the field inspired me for this study. More than a mentor, Dr. Perotti has consistently been a true inspiration and source of encouragement. I would also like to extend my gratitude to the committee members, Dr. Hansen Mansy, Dr. Robert L. Steward Jr., and Dr. Thomas Kean for their brilliant comments and suggestions.

TABLE OF CONTENTS

LIST OF FIGURES

LIST OF TABLES

CHAPTER 1: INTRODUCTION

Problem Definition and Motivation

In the US, one person dies every 36 seconds and 659,000 people die every year due to cardiovascular disease (CVD) [67]. CVD is a major public health concern in the US and worldwide, representing a leading cause of morbidity and mortality. Among CVDs, heart failure is a growing health problem [46].

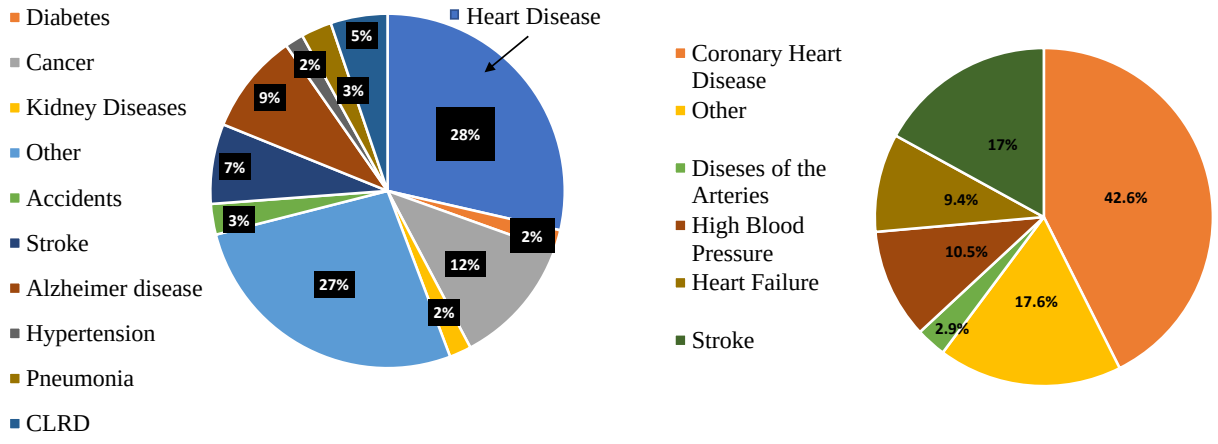

Figure 1.1: (a) Percentage of leading causes of death, USA, 2017.Source: CDC; (b) Percentage of deaths due to cardiovascular diseases (CVD), USA, 2017 [67]

Heart failure refers to a condition where the heart is unable to pump blood efficiently. It does not mean that the heart has stopped working, but rather that it is not pumping effectively. Heart failure can result from various cardiovascular conditions. Roughly 50% of patients affected by heart failure suffer from Heart Failure with preserved Ejection Fraction (HFpEF) [36], a condition with

the same symptoms of heart failure (i.e., shortness of breath, exercise intolerance, and fatigue), but with preserved ejection fraction (a measure of the amount of blood pumped through the circulatory system during each heartbeat). Despite several studies and clinical trials [108], HFpEF is still poorly understood and diagnosed. The inability to accurately diagnose HFpEF hinders prognosis and therapy planning, consequently compromising the outcome for patients affected by HFpEF. Several studies suggest that HFpEF is related to diastolic dysfunction and abnormalities in the passive response of the myocardium [16, 114]. Although the passive myocardial response is discussed in detail in the section 'The Cardiovascular System and the Heart' (chapter 1), in brief, it refers to the myocardium's behavior in response to mechanical forces when the heart is not actively contracting. Despite the significance of the passive myocardial response, there are currently no accurate material models of the passive myocardium, no accepted passive myocardium material properties, and no accurate description of the cardiac kinematics during atrial systole, when the response of the myocardium is (mostly) passive. This knowledge gap poses challenges in understanding the mechanism of diastolic dysfunction and HFpEF.

Available clinical measures, such as left ventricular ejection fraction (LVEF) are frequently used to evaluate cardiac function. However, LVEF has limitations, as it cannot quantify regional changes in cardiac function (e.g., regional changes in myocyte contractility) and is mostly linked to the active myocardial response. In addition to LVEF, myocardial deformation imaging techniques (e.g., strain echocardiography) have emerged as crucial tools for evaluating cardiac functions and dysfunctions [94]. Although these tools are very promising, they have been primarily applied to asses cardiac function during ventricular systole, not atrial systole when the myocardium response is mainly passive.

This thesis aims to better characterize the response of the passive myocardium by investigating the left ventricle (LV) deformation during atrial systole and by combining motion data (acquired using imaging) and intraventricular pressure to estimate the myocardium material properties and laws.

This study may help improve our understanding of the passive myocardial response and therefore enable a more timely and effective diagnosis and therapy planning for millions of patients affected by diastolic dysfunction and HFpEF.

The Cardiovascular System and the Heart

The cardiovascular system or blood circulatory system includes the heart and a closed system of vessels consisting of arteries, veins, and capillaries. This system is responsible for carrying the blood from and to the different parts of the body.

The fundamental organ of this system is the heart, which is essentially a muscular pumping machine. This machine is responsible for maintaining blood pressure. It is located between the two lungs and slightly left of the sternum or breastbone and is protected by the rib cage. Fig. 1.2 represents a schematic of the human cardiovascular system.

The heart is divided into four chambers. The two upper chambers are the right and the left atria (RA and LA, respectively). The two lower chambers are the right and the left ventricles (RV and LV respectively). Each of these chambers plays a crucial role in the heart's proper functioning. The RA receives deoxygenated blood and delivers it to the RV through the tricuspid valve. The RV pumps the deoxygenated blood through the pulmonary valve to the lungs where carbon dioxide is exchanged for oxygen. Next, the oxygen-rich blood reaches the LA from which it flows to the LV through the mitral valve (MV). Once the LV receives the blood, it pumps it through the aortic valve (AV) and ultimately throughout the rest of the circulatory system and the body. The contraction of the ventricles (corresponding to the pumping function of the heart) happens during systole. In contrast, the relaxation of the ventricles happens during diastole, which corresponds to the active relaxation and passive filling of the ventricles. Both active contraction and relaxation are key to

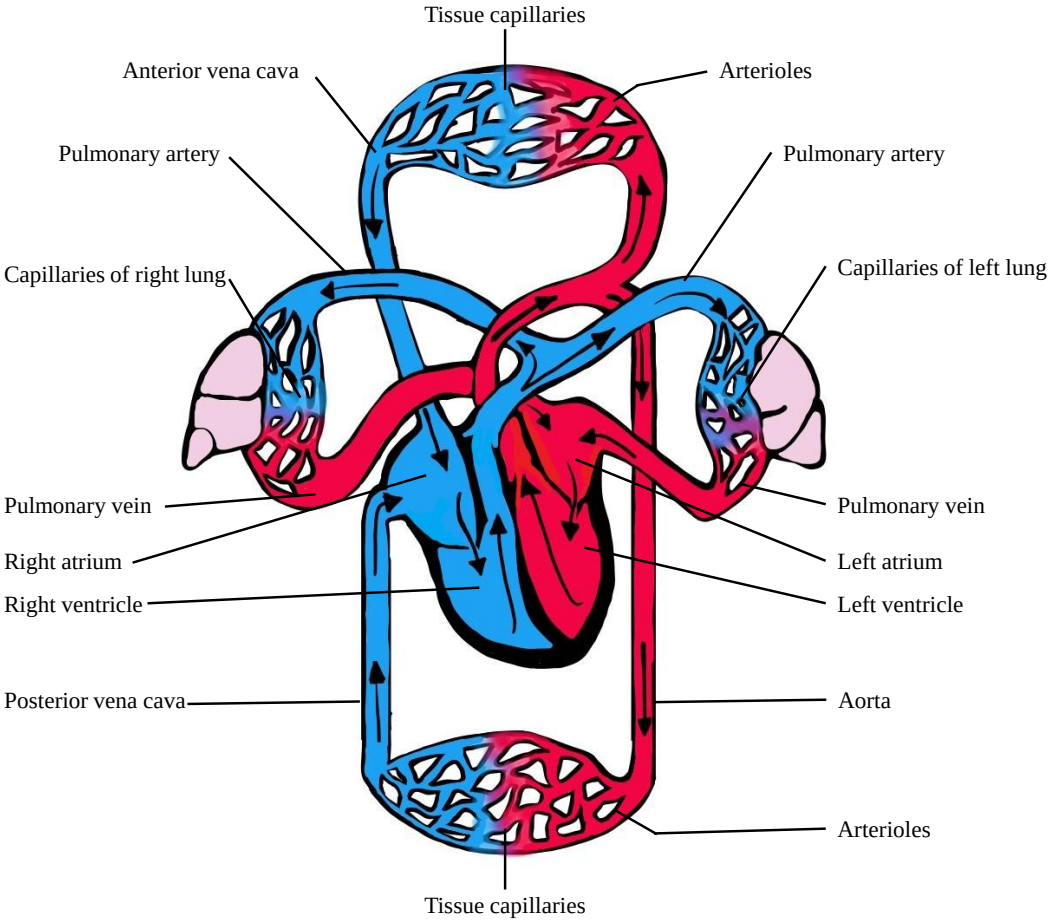

Figure 1.2: Schematic of the human cardiovascular system (Image was drawn starting from [17]).

the proper function of the heart. In this thesis, I will focus on the latter, where the response of the myocardium is mostly passive.

The passive response of the myocardium, as mentioned earlier, refers to the mechanical behavior of the myocardium when no active contraction is present. The passive myocardium response governs the ventricles filling phase (diastole) and therefore is critical in determining the amount of blood filling the ventricles that can be subsequently pumped through the circulatory system during each heartbeat. A healthy passive myocardium response enables the heart to efficiently relax and fill with blood in between contractions [38]. In addition, the passive myocardium

behavior plays a crucial role in determining how the ventricles respond to changes in volume and pressure throughout the entire cardiac cycle.

The passive behavior of the myocardium is due, in part, to the extracellular matrix which acts as a scaffold for the cardiomyocytes and therefore contributes to the overall mechanical strength and elasticity of the heart [45]. To understand and model the passive myocardium response, it is important to consider the multi-scale nature of the cardiac tissue. Fig. 1.3 illustrates the structural organization of the myocardium at different scales. At the macroscopic scale, the overall structure and function of the heart muscle is observed. This includes its gross anatomy, such as the arrangement of chambers, valves, and blood vessels. Techniques used at this scale include medical imaging modalities like echocardiography, magnetic resonance imaging (MRI), and computed tomography (CT), which provide detailed images of the heart's macro-scale structure and function. Studies at this scale often focus on understanding global heart function, such as cardiac output (CO), ejection fraction (EF), and contractile properties of the myocardium [152]. The meso-scale lies in between the macroscopic and microscopic scales and involves the study of tissue organization and properties at an intermediate level [152, 138]. This scale delves into the overall cardiomyocyte orientation (helix angle) and sheetlet organization. It also includes studying the mechanical properties of the tissue which can help determine the diseased state (e.g., loss of aggregate cardiomyocyte organization) [152]. Techniques such as cardiac diffusion tensor MRI with a voxel resolution of approx 2 mm and mechanical tissue testing can be used to investigate the meso-scale structure and function of the myocardium. At the micro-scale, we examine the myocardium at the cellular scale. This involves studying cardiac muscle cells individually at the sheetlet and sub-sheetlet levels. Techniques such as histology (which involves examining thin slices of tissue under a microscope) may be used in this context.

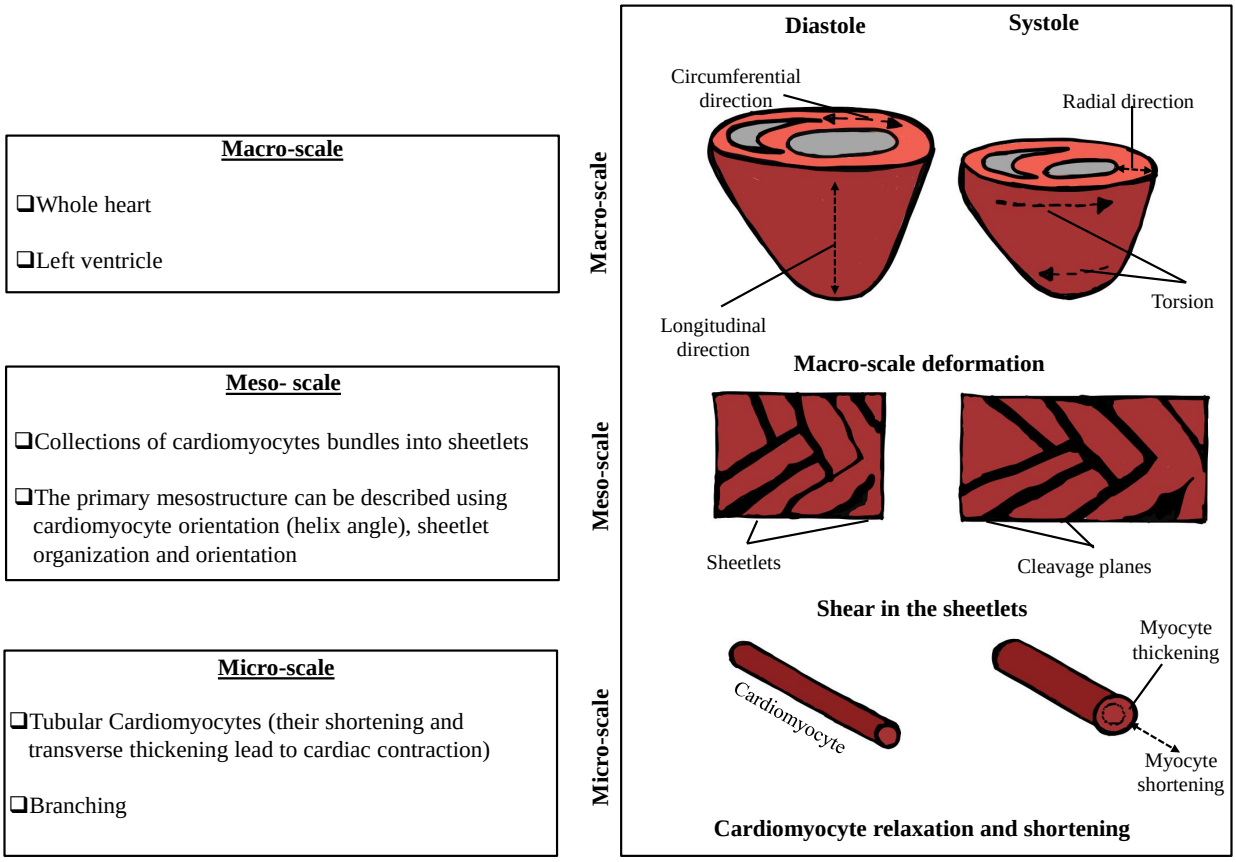

Figure 1.3: The multi-scale structure and function of the ventricles (Images were drawn starting from [152])

The study of the myocardium can involve the sub-cellular level as well, where the various components within the cardiomyocytes are investigated, e.g., the myofibrils (see Fig. 1.4). Techniques such as electron microscopy and molecular biology methods (e.g., Immunofluorescence Microscopy, Immunohistochemistry (IHC)) are used to investigate the sub-cellular structure and function within the myocardium [31]. Research at this scale may focus on the shortening and transverse thickening of single cardiomyocytes and the actin-myosin cross-bridge cycling mechanism [12, 33, 7], which is the basic functional unit governing contraction. Indeed, muscle contraction occurs through the sliding filament mechanism, where

the actin filaments slide past the myosin filaments leading to the shortening of the sarcomeres. Fig. 1.4a represents the structural hierarchy at the sub-cellular scale [7] and Fig. 1.4b represents a schematic of actin-myosin binding [117] (further discussed in chapter 2).

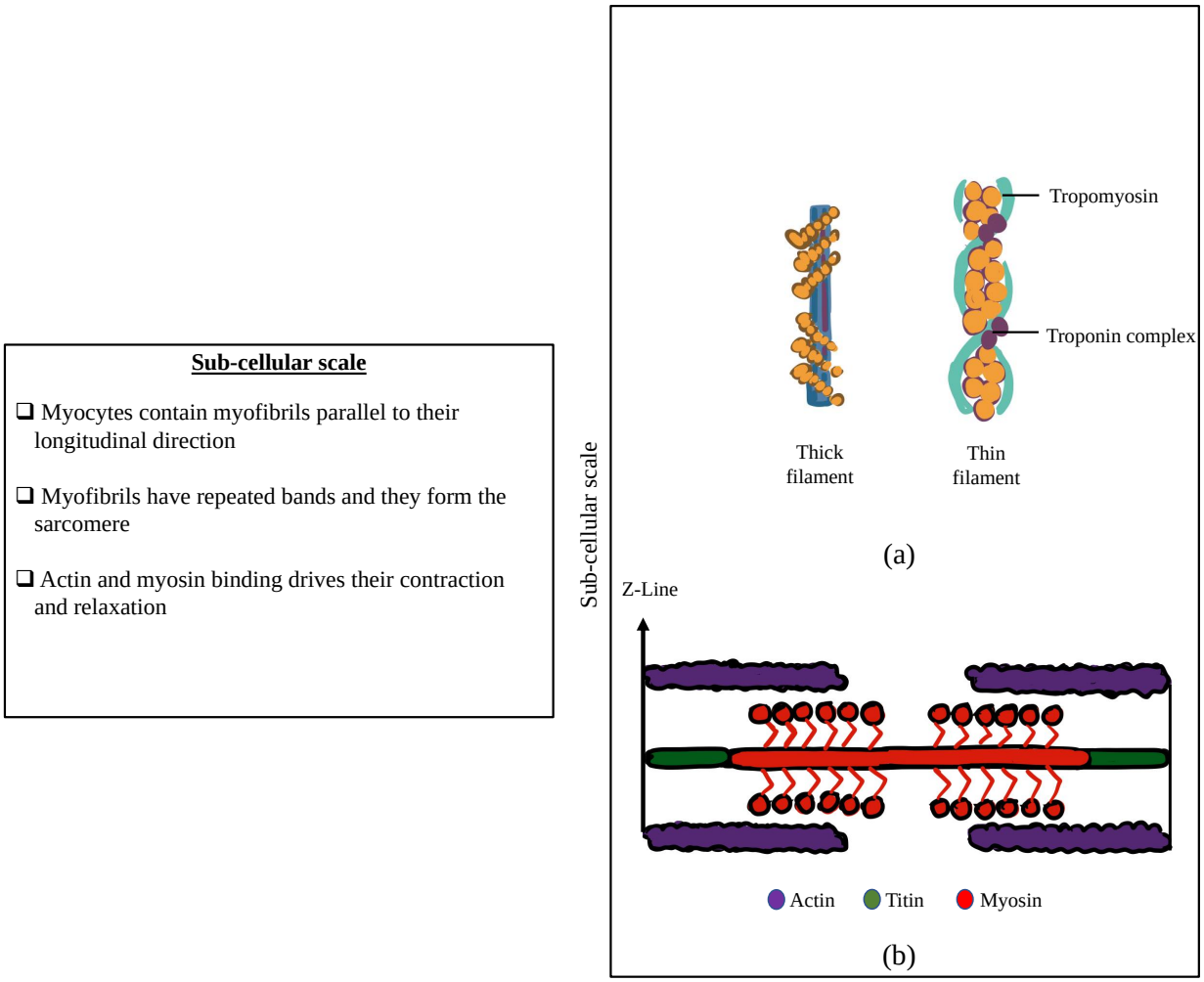

Figure 1.4: (a) Structural hierarchy at the sub-cellular scale; (b) Schematic of actin-myosin binding (Images were drawn starting from [7, 117])

Understanding the multi-scale structure is crucial for comprehending how changes at the molecular

and cellular levels, and alterations in the composition, organization, and geometry of the heart tissue affect its passive mechanical behavior and impact the overall mechanical properties of the myocardium.

Objective and Primary Contributions of Current Study

The goal of this research is to better characterize the response of the passive myocardium so that passive myocardium material properties and strains during atrial systole can be adopted in the future to detect the onset and progression of diastolic dysfunction and HFpEF. These new biomarkers may pave the way for earlier diagnosis and more accurate prognosis and therapy planning for millions of patients. To achieve this overarching goal, we pursue three objectives: 1) We evaluate the pressure-volume relation during end diastole and provide a model to characterize changes in the passive left ventricular response; 2) We characterize cardiac strains during atrial systole to define a normal range of expected circumferential, longitudinal, and radial strains during late filling where the response of the myocardium is mostly passive; and 3) We calibrate a passive myocardium material law to improve the quantification of myocardium passive stiffness. We derived and tested these measures using preclinical data acquired in swine subjects.

Organization of Dissertation

This dissertation is divided into six chapters of which this is the first. This chapter provides the motivation for this study, a brief general overview, and the objectives and primary contributions of this thesis. Chapter 2 summarizes the previous work in the literature and contextualizes the current research. Chapter 3 reports a summary of the dataset used in this study and provides a detailed description of the derived pressure-volume (PV) loops and end-diastolic pressure-volume

relationship (EDPVR) models. Chapter 4 describes the cardiac kinematics during atrial systole and analyzes radial and circumferential strains during late filling. Chapter 5 presents the methodology for deriving passive myocardium material laws and for estimating material properties from measured kinematics and intraventricular pressure during atrial systole. Chapter 6 summarizes the major findings of this study, its limitations, and suggestions for future work.

CHAPTER 2: BACKGROUND AND LITERATURE REVIEW

The main goal of this study is to characterize the response of the passive myocardium. Computing the material properties and the material laws describing the passive myocardium material response will involve 1) The analysis of the LV pressure-volume (PV) loops and the end-diastolic pressure-volume relation (EDPVR); 2) The study of cardiac deformation during atrial systole; 3) The optimization of the equilibrium between external (i.e., LV pressure from PV loop) and internal forces (due to the myocardium deformation). Thus, with the intent of situating this research in the current literature, this chapter will review previous studies on LV PV loops, EDPVR, the estimation of cardiac deformation and strains, and computational models using different material models in health and disease.

Pressure Volume loop

The LV PV loop is an important tool for quantifying both LV systolic and diastolic performances [19] and provides direct information relating to LV chamber pressure and volume. From the early 80's, LV PV loops have been serving this purpose [22, 122] and recently they have become a gold standard for in vivo hemodynamic quantification in animal models [18, 78]. Conventionally, invasive methods, such as cardiac catheterization, can be used to measure the LV chamber pressure directly. Using conductance catheters [134], pressure and volume data can be acquired simultaneously, but this procedure is laborious and also has limited accuracy [49, 151]. Many studies use a combination of cardiac catheterization for pressure data and imaging for volume data [24, 49, 147]. Imaging data may be acquired from echocardiographic or cardiac magnetic resonance imaging (CMR). Because of their invasive nature, PV loops are not yet considered a gold standard for clinical research or analysis in human subjects [66, 119]. However,

there are promising new studies in this area to enable PV loop estimation in a broader patient population. For example, recent studies proposed an experimentally validated noninvasive method to compute PV loops, which enables the quantification of systolic and diastolic cardiac functions using LV volume curves from cardiac magnetic resonance (CMR) images and brachial pressure [125, 127].

Systolic/diastolic functions from LV PV loops

The LV PV loop can be subdivided into four phases and from each of these phases, different LV chamber properties can be derived [19, 121]. LV systolic function consists of the contraction of the LV followed by the diastolic function, which involves the active relaxation and the passive filling of the ventricles. These functions are essential to understanding and assessing the LV pathophysiology, especially in heart failure [19]. HFpEF is a form of heart failure characterized by abnormalities in diastolic function (also defined as diastolic dysfunction or DD). DD is characterized by abnormal ventricular relaxation and filling patterns (abnormal mechanical function during diastole) regardless of preserved or reduced EF [106]. In DD, LV diastolic chamber stiffness increases, thus resulting in incomplete pump function [90]. The intrinsic resistance of the LV to stretch or expand during diastole is characterized as LV diastolic chamber stiffness. Another study showed that, in patients with normal EF, increased diastolic chamber stiffness is also an indicator for diastolic abnormalities [151]. These patients may or may not be symptomatic.

From LV PV loops several key parameters can be derived to assess the LV systolic and diastolic functions, e.g., the End-Systolic Pressure-Volume Relationship (ESPVR), the End-diastolic Pressure-Volume Relationship (EDPVR), the stroke volume (SV), LVEF, the LV relaxation time constant (Tau or τ), the LV diastolic chamber stiffness (dPdV), and the diastolic filling pressure.

The indices of diastolic function and dysfunction are discussed in detail in the next sections as they are most relevant to the current research.

Computation of indices of diastolic function

There are several indices of the LV diastolic function that can be computed from the LV PV loops. The maximum rate of increase in volume during diastole (computed as $dVdt_{max}$) and the maximum rate of pressure decline during diastole (computed as $dPdt_{min}$) can be calculated by computing the first derivative of LV volume and pressure respectively with respect to time [53, 106]. As DD progresses the $dVdt_{max}$ and absolute value of $dPdt_{min}$ have been reported to increase [53, 61, 118].

From the isovolumic relaxation phase of the PV loop, the isovolumic relaxation time or IVRT — defined as the time interval between the closing of the aortic valve (AV) and the opening of the mitral valve (MV) — can be calculated [101]. The diastolic volume recovery time or DVRT can be computed by analyzing the isovolumic relaxation and diastolic filling phase. DVRT is defined as the time interval between the end of systole (ES) and the time when the volume is equal to 80% of the stroke volume (SV) [102]. In disease — e.g., in the presence of DD, myocardial infarction (MI), or HFpEF — both IVRT and DVRT are reported to increase [123, 23, 74].

Next, the slope of the end-systolic PVR (written as E_{es}) — an index of cardiac contractility — can be determined from different methods available in the literature (e.g., Senzaki et al.'s single beat estimation method [126]). The arterial system properties can be determined as E_a. E_a is defined as the effective arterial elastance [132, 55]. After calculating both indices, the ventricular-arterial coupling (VAC) can be computed as the ratio of E_a to E_{es} [132, 55]. VAC describes how well the ventricles and arteries work together to efficiently deliver blood to the body's tissues and organs. Therefore VAC is an expression of global cardiovascular efficiency. In healthy humans, VAC has been reported in the range of 0.6 to 1.2 [131, 34]. Studies involving DD reported an elevated

VAC [4], which corresponds to decreased ventricular efficiency.

Another important indicator of LV diastolic function and dysfunction is the time constant of relaxation Tau (τ), which measures the rate of fall in pressure during the isovolumic relaxation phase. Several methods are reported in the literature to compute Tau, e.g, τ_{Weiss}, [150], τ_{Glantz} [59], $\tau_{Logistic}$ [92]. Each of these methods has both advantages and disadvantages. τ_{Weiss} is the first method to compute this time constant of relaxation and uses a mono-exponential assumption. τ_{Weiss} assumes that the LV relaxes to zero pressure, which is not generally true. Compared to τ_{Weiss}, τ_{Glantz} accounts for the changes in the baseline pressure and therefore has reduced sensitivity to an increasing preload. However, both τ_{Weiss} and τ_{Glantz} models depend greatly on the pressure cut-off point. This point is typically defined as the time when LV pressure reaches a certain percentage of its peak value during systole. Specifically, the pressure cut-off point is often set at 10% of the LV peak systolic pressure. This is based on the assumption that by this point, most of the isovolumetric relaxation phase has occurred, and LV pressure has significantly decreased from its peak systolic value. Matsubara et al. showed that $\tau_{Logistic}$ remains constant across different cut-off points and it does not depend on the pressure cut-off values. In DD and HFpEF, significantly prolonged τ has been reported in the literature [118].

In HFpEF, while EF is preserved, abnormalities in diastolic function and impaired ventricular filling can also lead to decreased EF [74]. Variation in one or more of the indices reported above can indicate diastolic abnormalities and impaired relaxation and therefore offer insight into the causes of HFpEF.

Computation of LV end-diastolic pressure-volume relationship (EDPVR)

Another indicator of LV diastolic function and dysfunction is the LV passive chamber stiffness of the myocardium. This property is related to the "resistance" of the LV to stretching during

early (rapid) and late filling [81, 135]. This can be quantified *in vivo* from the (EDPVR) [19, 82]. Considering both invasive and non-invasive methods for measuring pressure (see section 'Pressure Volume loop', chapter 2), clinical application of the EDPVR is not considered feasible yet. Indeed, invasive pressure measures can be acquired only in a small patient population given the risks involved with this procedure. On the other hand, the non-invasive setting still has limitations due to the several assumptions necessary for its application.

Nevertheless, when feasible, EDPVR serves as one of the key indicators for characterizing diastolic ventricular function [151]. Mathematical models are commonly utilized to predict the PV relationship when direct measurements are unavailable [73, 134]. These models provide insights into the underlying pathophysiology, including parameters related to LV chamber stiffness, such as the diastolic chamber stiffness coefficient [129, 142, 149]. Studies indicate that both LV diastolic operating chamber stiffness (dPdV) — it refers to the rate of change of pressure (dP) with respect to volume (dV) during diastole and quantifies how much the pressure inside the LV changes in response to changes in volume — and diastolic chamber stiffness coefficients — derived from the mathematical models and representing the overall stiffness of the LV chamber during diastole — increase in various cardiac diseases (e.g., MI, HFpEF, HF, LV remodeling, DD) [11, 13, 129, 157]. Understanding the critical assumptions and factors affecting LV diastolic properties is crucial for evaluating LV diastolic and systolic functions.

The most widely accepted model to fit the EDPVR is an exponential model. According to this model, the LV intraventricular pressure P can be written as $P = be^{kV}$ [52, 53, 116, 151], where 'b' and 'k' are curve fitting parameters and V is the LV cavity volume. Although useful and widely accepted, this model also presents disadvantages, e.g., it depends on the patient ventricle size and loss of exponential PV relation at low pressure [96]. Despite these disadvantages, the exponential model is still being used to predict the EDPVR in many studies [106]. To overcome the loss of exponential PV relation at low pressure, some studies considered a power model, i.e., $P = b + cV^{\gamma}$

or $P = dV^{\gamma}$ [19, 73], where 'b', 'c', 'd' and γ are curve fitting parameters. In this context, one of the widely accepted curve fitting methods is the Klotz model [76], which is a single-beat approach to evaluate the whole EDPVR from one measured pressure and volume point. The equation is written as $EDP = \alpha EDV^{\beta}$ [76] where, α and β are curve-fitting parameters. Klotz model also can be written as $EDP = A_n(EDV)_n^{B_n}$ where volume and curve-fitting parameters A_n, B_n are normalized [76]. In a more recent study, Wang et al. proposed a cubic polynomial model to obtain a more accurate fit to the pressure-volume experimental data [49]. Despite predicting a better fit to the EDPVR, this model needed more than one parameter.

Though most of these models fit the EDPVR from the minimum pressure during diastole to the end of diastole (ED) [73, 76, 84, 135, 151], some studies have considered fitting the model to predict EDPVR from diastasis to ED [156]. The hypothesis behind doing so is to capture only the response of the myocardium where the LV is relaxed [75, 89, 156]. Physiologically, LV diastole is divided into active relaxation (which includes isovolumic relaxation and rapid recoil or early filling phase), diastasis or slow filling phase, and the late filling phase (during atrial contraction) [135, 159]. Thus, diastolic dysfunction refers to the disruption in any phase or the combination of the LV relaxation and filling phases during diastole [82, 159]. In HFpEF and DD, 'stiff' cardiomyocytes are identified as one of the main contributors [15, 140]. The giant cytoskeletal protein titin extends the sarcomere from the Z disk to the M disk [26, 64, 85]. Titin serves as a spring (it acts as a spring-like element in both directions of stretch and recoil during the cardiac cycle) which in turn is responsible for both early diastolic recoil and late diastolic distensibility [64, 69, 85]. During the 'recoil' phase titin helps to restore the cardiac sarcomere to its reference configuration [69, 160]. Further, titin is the fundamental contributor to passive tension, which determines the extent of LV filling and the shortening velocity of the cardiomyocytes [60, 81]. The PEVK segment (a region of the titin protein molecule characterized by the presence of proline (P), glutamate (E), valine (V), and lysine (K) amino acids) is one of the key regions of titin responsible for its elastic

properties. A recent study investigating the effect of titin's PEVK segment deletion concluded a significant reduction in viscosity during the early rapid filling phase, indicating its crucial role in regulating diastolic function [27, 25, 79]. Alterations in the titin structure, such as the PEVK segment deletion, may influence myocardial stiffness. In conditions like MI and DD, compromised active relaxation due to reduced elastic energy stored in titin following myocyte contraction has been observed [135], highlighting the importance of including the active relaxation phase (e.g., early filling or rapid recoil) phase for the calculation of LV diastolic chamber stiffness and for the prediction of the EDPVR model. Based on these observations, this research follows a similar approach and includes the active relaxation phase in proposing a novel LV EDPVR model that retains the simplicity of the Klotz approach while providing a more direct assessment of passive myocardial stiffness and a better approximation of the experimental data.

Cardiac deformation (strain) mapping during atrial systole

The LV ejection fraction (EF) or LVEF is one of the most common clinical measures to evaluate cardiac function [44]. Despite its widespread use and ability to be computed through routine clinical exams (e.g., echocardiography, computed tomography (CT), magnetic resonance imaging (MRI) [44]), EF is not a sensitive measure and is incapable of quantifying *regional* changes in cardiac function that are linked to cardiovascular disease (CVD), e.g., due to myocardial infarction [128].

Aside from LVEF, other measures of cardiac kinematics could be readily computed. For example, LV strain and strain rate could be computed from echocardiography or MR images to assess the function of the heart, particularly the LV. They provide detailed information about myocardial deformation. Studies showed that radial LV wall thickening closely correlates with EF. Yet, impaired longitudinal strain can still result in preserved radial and circumferential strain in

patients with DD [104]. In this same study, LVEF was also reported with no significant differences between the patient (type II diabetes mellitus) and the control group. In contrast, LV strain and strain rate can detect subtle changes in myocardial mechanics even before significant alterations in LVEF occur. This sensitivity is particularly important in the early detection of DD, which may precede systolic dysfunction in certain cardiac conditions. Numerous studies have concluded that strain and strain rates are more sensitive indices of LV function and dysfunctions compared to LVEF [40, 143, 41]. Additional research, such as [145, 99], suggests that LVEF alone may not be sufficient for identifying diastolic heart failure, emphasizing the importance of considering strain measurements [100].

Since HFpEF has been associated with impaired passive myocardial behavior [21, 158], strains during the passive filling phase may be an important indicator of the onset and progression of HFpEF. During early diastole, blood flows passively from the left atrium (LA) to the LV through the mitral valve (MV), accounting for approximately 70% of the total ventricular filling [57]. Atrial systole occurs late in ventricular diastole, during which the remaining filling (approximately 30%) occurs passively [57]. Understanding the changes occurring during this late filling becomes important in many heart diseases (e.g., Ischaemia, Myocardial Hypertrophy [128], Ventricular Hypertrophy [100], Systolic and Diastolic dysfunction [136], Angina pectoris [14]). An increased stiffness of the cardiac muscle may hinder ventricular deformation during the passive filling phase and therefore reduced strains during atrial systole may be a marker of HFpEF. Part of my work focuses on assessing strains during atrial systole (late diastole) to provide insight into their magnitudes and their potential use in assessing DD.

To enhance the understanding of LV function, several quantitative strain imaging techniques have been developed, e.g., Tissue Doppler echocardiography (TDE), Speckle-tracking echocardiography (STE), Feature tracking cardiac magnetic resonance imaging (FT-CMR)). Among them, DENSE (Displacement Encoding with Stimulated Echoes) MRI encodes tissue

displacements by utilizing the phase of the MRI signal [2] and has demonstrated high reproducibility [88]. In DENSE voxel phase values are related to voxel displacements. DENSE MRI has been used to primarily evaluate and quantify LV motion during ventricular systole [148] and minimal analysis using DENSE during atrial systole has been carried out. Although direct studies are scarce, there is some data available for comparison from 2D echocardiography, which measures strain rates during atrial systole. These studies reported strain rates during atrial systole in both healthy and diseased groups.

From these studies, it is evident that impaired LV relaxation in the longitudinal direction (Peak atrial systolic LV longitudinal strain rate) can be an early predictor in patients with hypertension (HT) [98]. The longitudinal, radial, and circumferential strain rates found from 50 control individuals reported in this study were $1.1 \pm 0.2s^{-1}$, $-1.8 \pm 0.7s^{-1}$ and $0.7 \pm 0.3s^{-1}$ during atrial systole. Whereas, the longitudinal, radial, and circumferential strain rates reported in the HT group were $1.2 \pm 0.3s^{-1}$, $-1.9 \pm 0.8s^{-1}$ and $0.9 \pm 0.3s^{-1}$ during atrial systole [98]. In a study involving patients with left ventricular hypertrophy (LVH), compromised regional diastolic function has been observed, while the systolic function was preserved [37]. Notably, a reduced LV circumferential strain rate was reported in the LVH group during atrial systole ($1.4 \pm 1.0s^{-1}$) versus the control group ($1.7 \pm 0.9s^{-1}$). This underscores the importance of evaluating atrial systolic strain, even in cases where systolic function is preserved. Another study reported a stronger correlation between carotid arterial stiffness and diastolic LV longitudinal strain rate [97]. The existence of cardiovascular risk factors stimulates not only vascular structural changes but also functional changes with aging. These changes result in a correlation between LV relaxation and arterial stiffness. This study reported longitudinal, radial, and circumferential strain rates as $1.3 \pm 0.3s^{-1}$, $-1.4 \pm 0.9s^{-1}$ and $1.2 \pm 0.3s^{-1}$ respectively during atrial systole in the control group. Whereas, the longitudinal, radial, and circumferential strain rates were reported to be $1.2 \pm 0.3s^{-1}$, $-1.5 \pm 0.6s^{-1}$, and $1.1 \pm 0.3s^{-1}$, respectively, among patients with

cardiovascular risk factors and heart diseases. In a study by Mizuguchi et al. [99], the strain rates obtained during atrial systole among healthy individuals in the longitudinal, radial, and circumferential directions were $1.1 \pm 0.3s^{-1}$, $-1.4 \pm 0.9s^{-1}$, and $1.1 \pm 0.3s^{-1}$. In this same study, the patient group was divided into two groups (according to the ratio of early diastolic to atrial systolic velocity, E/A). In the $E/A \geq 1$ group the longitudinal, radial and circumferential strain rates were $1.2 \pm 0.2s^{-1}$, $-1.4 \pm 0.5s^{-1}$ and $1.0 \pm 0.3s^{-1}$ respectively. Among the $E/A < 1$ group, the longitudinal, radial, and circumferential strain rates were $1.4 \pm 0.2s^{-1}$, $-1.8 \pm 0.8s^{-1}$ and $1.4 \pm 0.4s^{-1}$ respectively. This study reported LV strain rates during atrial systole greater in all three directions in the $E/A < 1$ group compared to the values obtained in the $E/A \geq 1$ group [99]. In another study by Mizuguchi et al., the longitudinal, radial, and circumferential strain rates found in 22 control subjects were $1.3 \pm 0.3s^{-1}$, $-1.2 \pm 0.8s^{-1}$ and $1.2 \pm 0.3s^{-1}$, respectively. However, the task of translating strain rates into equivalent strain measures remains challenging due to the variability of strain rates during atrial systole and potential differences in atrial systole duration among patients and healthy subjects. This study aims to address this challenge by quantifying values of ventricular strain during atrial systole.

Material Parameters of the Passive Myocardium

Numerical modeling using the Finite Element Method (FEM) has become increasingly popular to understand the complex cardiac mechanics in health and disease. However, the results obtained from FEM simulations greatly depend on the constitutive model, whose selection and validation remain challenging.

The material or constitutive law for the passive myocardium

The material properties of the cardiac muscle are typically described in the context of constitutive laws that relate stress (force per unit area) to strain (deformation) under different loading conditions. The selection of the constitutive laws and their material properties describe the mechanical response of the tissue that is being observed. Regarding the passive myocardium material response, the work of Demer et al. [35] and Yin et al. [153] showed with biaxial experiments that the passive myocardium is anisotropic. In agreement with these early observations, some of the widely used constitutive laws (e.g., the models of Guccione et al. [62] and Holzapfel et al. [70]) describe the passive myocardium as an orthotropic material. For example, the strain energy density function for the passive myocardium material model of Guccione et al. [62] is written as

$$W_{\text{Guccione}} = \alpha_1 \exp\left[\alpha_2(E_{ff}^2 + \alpha_3(E_{ss}^2 + E_{nn}^2 + 2E_{sn}^2) + 2\alpha_4(E_{fs}E_{sf} + E_{fn}E_{nf})\right] \tag{2.1}$$

where E_{ff}, E_{ss}, and E_{nn} are the Green-Lagrange strains in the fiber $\mathbf{f}$, sheetlet $\mathbf{s}$, and normal-to-the-sheetlet $\mathbf{n}$ directions, respectively; E_{sn}, E_{fs}, and E_{fn} are the Green-Lagrange shear strains between the fiber, sheetlet, and normal directions; and finally α_i are material parameters.

The Holzapfel-Ogden model is a hyperelastic constitutive model that also captures the anisotropic and nonlinear response of the myocardium [70]. This model is often used when a more detailed representation of the microstructure is required and has the following strain energy density function:

$$\begin{aligned} W_{\text{Holzapfel}} = \frac{\alpha_1}{2\alpha_2}\exp\left(\alpha_2(I_1-3)\right) + \frac{\alpha_3}{2\alpha_4}\left(\exp\left[\alpha_4(I_{4f}-1)^2\right]-1\right) + \\ \frac{\alpha_5}{2\alpha_6}\left(\exp\left[\alpha_6(I_{4s}-1)^2\right]-1\right) + \frac{\alpha_7}{2\alpha_8}\left(\exp\left(\alpha_8 I_{8fs}^2\right)-1\right), \end{aligned} \tag{2.2}$$

where $I_{4f} = \mathbf{f} \cdot \mathbf{Cf}$, $I_{4s} = \mathbf{s} \cdot \mathbf{Cs}$ and $I_{8fs} = \mathbf{f} \cdot \mathbf{Cs}$ and α_i are material parameters.

In the above strain energy function $\mathbf{E}$ is the Green-Lagrange strain tensor $\mathbf{E} = \frac{1}{2}(\mathbf{C} - I)$. $\mathbf{C}$ in turn can be written in terms of the deformation gradient tensor, $\mathbf{F}$ as $\mathbf{C} = \mathbf{F}^T\mathbf{F}$. In this study, I will investigate how to calibrate a constitutive law to describe the response of the passive myocardium.

LV microstructure-based models

In addition to an accurate material model, two of the key elements necessary to model the LV mechanical response using FEM are the LV geometry and the microstructure of the myocardium. For patient-specific simulations, the LV geometry should appropriately represent the distinct size and shape of the patient's LV. Patience-specific LV geometry can be extracted from routine MRI exams (e.g., cardiac CINE and DENSE MRI). Next, to formulate an accurate model of the LV, it is necessary to incorporate the myocardium microstructure to capture its anisotropy. The microstructure of the myocardium can be incorporated by considering the myofiber orientation. Myocardial fiber orientation is a critical element for modeling cardiac function and dysfunction as it can be an indicator of health and disease. It can be estimated from diffusion tensor MRI (DT-MRI), although acquiring this data remains challenging. As an alternative, in the absence of experimental data, different rule-based models for the 3D architecture of the myocardium could be adopted.

CHAPTER 3: PRESSURE VOLUME LOOPS AND END DIASTOLIC PRESSURE VOLUME RELATION

This chapter discusses the calculation and analysis of LV pressure-volume loops from experimental MR and intraventricular pressure data. This includes the development of a model for the end-diastolic pressure-volume relation (EDPVR). By the end of this chapter, we will achieve the first objective of this study, which involves the analysis of left ventricular PV loops and the EDPVR.

Experimental data

The data set utilized in this study was part of a larger study intended to identify the material behavior of the passive myocardium [115] and to characterize cardiac mechanics [141]. As part of the research, an infarct model was established using female Yorkshire swine subjects. For the first objective of this study, both subject groups control and myocardial infarction (MI) are used. Figure 3.1, represents a flow chart that summarizes the data acquisition procedure.

Initially, the study included a total of 16 (N=16) female Yorkshire swine (n=9 control, n=7 with MI). In each of the groups (control and MI), two subjects had pericarditis. Among the MI group, one had infarction mostly in the RV and thus all 3 subjects were excluded from further analysis. For the final study, a total of thirteen (N=13) subjects are considered. Eight (n=8) subjects were healthy (control group) while infarction was successfully induced in five (n=5) subjects (MI group). The types of acquired images can be divided into two groups: *in vivo* and *ex vivo*. The work presented in this chapter primarily used cardiac CINE MRI along with pressure data obtained through *in vivo* cardiac catheterization. Intraventricular pressure was recorded throughout the MRI data acquisition [87]. *Ex vivo* T1 weighted images were used to quantify the percentage of infarct

in each subject in the MI group for the validation study of the proposed EDPVR model.

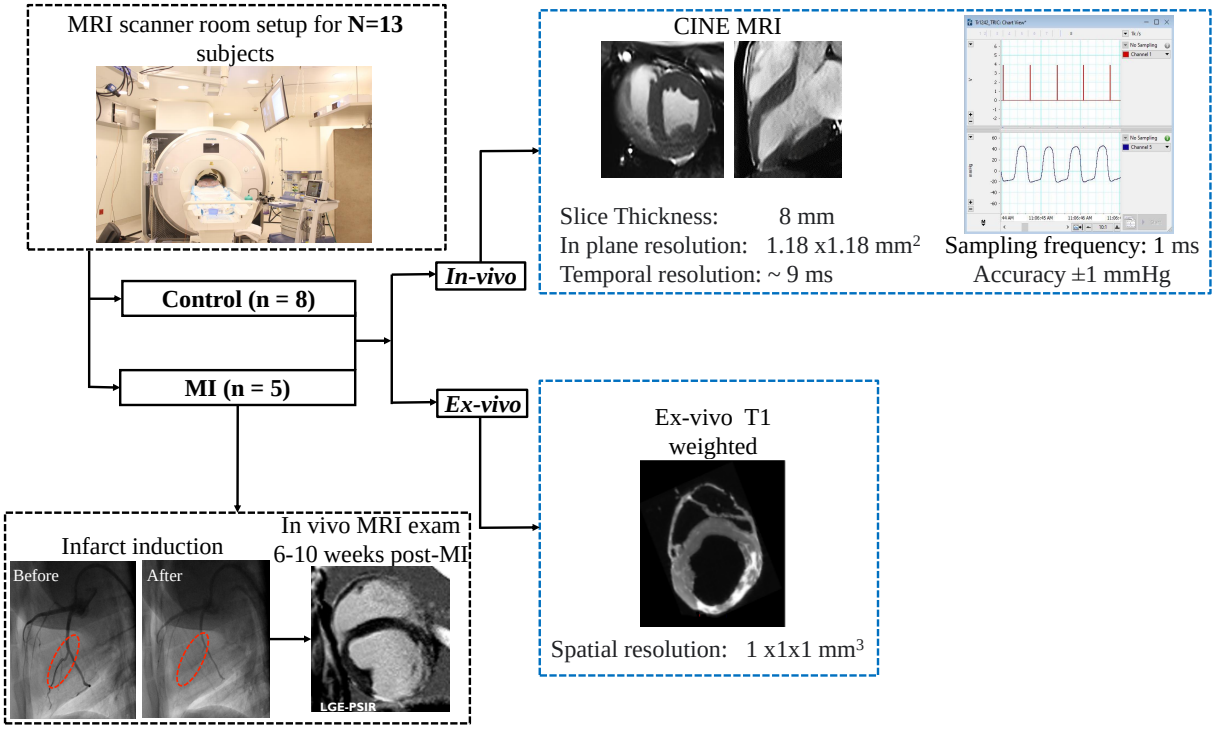

Figure 3.1: Flow chart representing the acquisition of the data used in the reconstruction of the PV loops and EDPVR model

Methodology and Data Analysis

The following sections describe the methodology that led to the computation of the intraventricular pressure during the cardiac cycle, the generation of the LV PV-loops, and lastly the prediction of the EDPVR models. This is briefly divided into

1. Generation of the pressure curve;

2. Generation of volume data from CIM using cardiac CINE MRI;

3. Registration of pressure and volume data and *in vivo* LV PV-loops generation;

4. *In vivo* end-diastolic pressure-volume relations (EDPVR);

5. Quantification of *in vivo* LV cardiac indices;

6. Statistical analysis.

Generation of pressure curve

Intraventricular pressure data was acquired via cardiac catheterization for the subject group control and MI (N=13). The PowerLab data acquisition system and LabChart software (ADInstruments, Colorado Springs, CO, USA) were utilized for this purpose and the data was saved as a LabChart data file (.adicht). These data files contain multiple blocks acquired during different times of the day and throughout the MRI acquisition period. A dedicated Matlab code [91] was built and used. The purpose of this code was to load and read the pressure data from the LabChart data files according to the beginning and end of the acquisition time of the cardiac CINE MRI for each subject. This procedure guarantees that the pressure data is synchronized with the cine MRI data utilized for estimating LV cavity volume during the cardiac cycle. As each cine MRI data acquisition encompasses numerous heartbeats, the calculation of the pressure trace corresponding to the cardiac cycle during the cine MRI acquisition involved the following:

1. The duration of each cardiac cycle was measured;

2. Each pressure trace was interpolated to the median cardiac cycle duration;

3. The median pressure profile was extracted along with its 95% confidence intervals, which were acquired at end-expiration.

Figures 3.2a and 3.2c show LV pressure traces with concurrent cardiac cycle signal (trigger) and Fig. 3.2b and Fig. 3.2d show beat-averaged LV pressure traces with CI for subject groups control and MI, respectively. In our study, we used the pressure data at the end-expiration phase to limit the variation in pressure due to the respiratory motion [147].

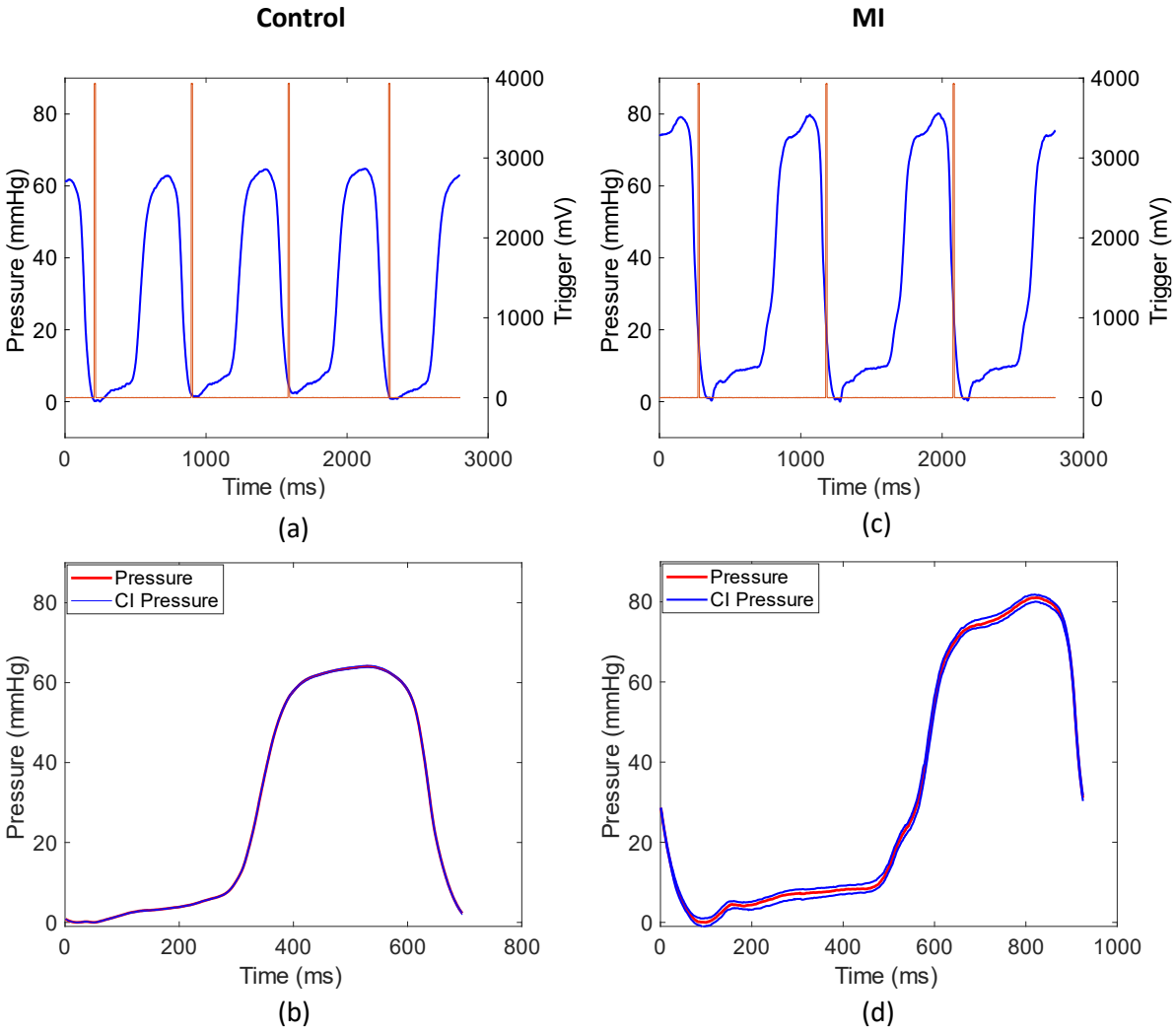

Figure 3.2: Intraventricular pressure with concurrent cardiac cycle signal (trigger) for subject groups control (a) and MI (c). Beat-averaged left ventricular pressure for subject groups control (b) and MI (d).

Generation of volume data from CIM using cardiac CINE MRI

A previously validated image segmentation software, 'The Cardiac Image Modeller (CIM, v8.2, University of Auckland) [86, 154]' was used to segment the cardiac CINE MRI data and compute the LV endocardial or cavity volume during the cardiac cycle. The input for CIM is CINE MR images acquired during the acquisition procedure. Segmentations were done following the procedures described in [86, 154]. For the validation of inter-observer variability of the volume data, each segmentation was done twice by an observer.

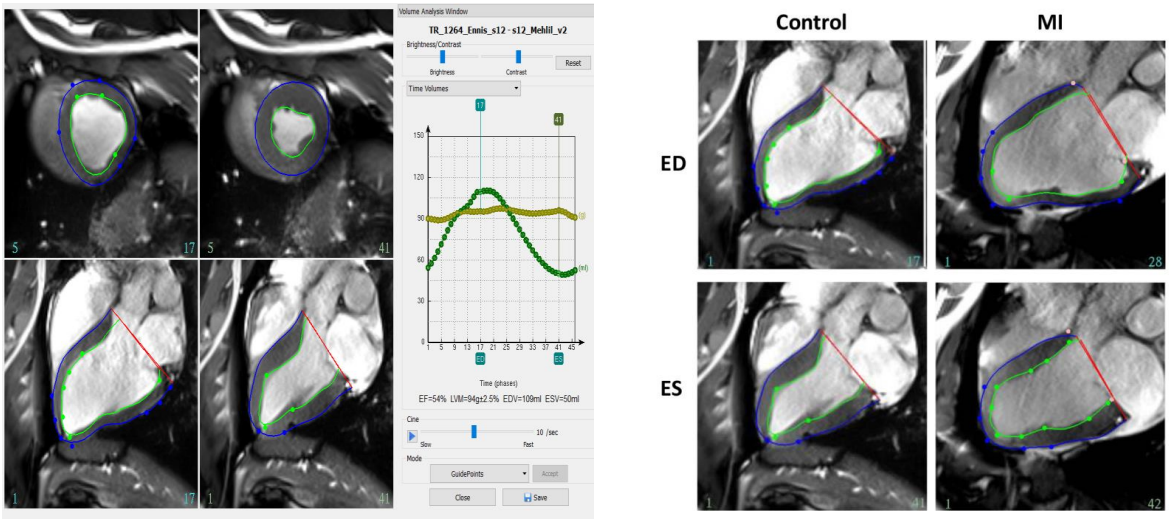

(a) (b)

Figure 3.3: (a) LV anatomy segmentation in CIM; (b) LV anatomy segmentation using guide-point modeling for subject groups control and MI shown at ED and ES phases.

Fig. 3.3a represents the LV anatomy segmentation procedure in CIM and Fig. 3.3b represents the long axis (LA) images using guide-point modeling in CIM for both subject groups. Fig. 3.3b shows the end-diastole (ED) and end-systole (ES) phases selected during the segmentation procedure.

The LV volume data and EF were extracted from the LV model for each time frame and then saved from CIM for further analysis. From each of the segmentations, total epicardial, endocardial (cavity), and wall volumes were also computed. The cavity volumes were further used in the generation of *in vivo* PV loops as described in the section 'Registration of pressure and volume data and *in vivo* pressure-volume loop generation' (chapter 3) and later shown in Figures 3.4b and 3.4d.

Registration of pressure and volume data and in vivo pressure-volume loop generation

For the registration of the generated pressure following the procedure detailed in the section 'Generation of pressure curve' (chapter 3) and the volume data detailed in the section 'Generation of volume data from CIM using cardiac CINE MRI' (chapter 3), a MATLAB code [91] was built. The volume generated from CIM was interpolated according to the median cardiac cycle length of each healthy and MI subject. Thus, an equal number of pressure and volume data points were generated for each subject. The pressure cycles were previously calculated in milliseconds while generating beat-averaged pressure curves. These pressure points were plotted against volume points to get beat averaged LV PV loops for each subject as depicted in Figure 3.4. After the generation of LV PV loops, the opening and closure of the mitral (MV) and aortic (AV) valve as observed in the cardiac CINE MRI images [63, 133, 144] were identified. These events allow to separate diastolic filling, isovolumic contraction, systolic (ventricular) ejection, and isovolumic relaxation.

In vivo end-diastolic pressure-volume relations (EDPVR)

To evaluate the LV EDPVR and diastolic properties between subject groups control and MI, we focus on the diastolic filling segment of the LV PV loops. As previously discussed (see section

'Computation of LV end-diastolic pressure-volume relationship (EDPVR)', chapter 2), there are different types of equations – e.g., exponential, cubic, and power fit – available for fitting the EDPVR. These equations are summarized in [19].

In our study, we isolated the segment from the minimum pressure (P=0 mmHg) during diastole to the end of diastole (ED). The rationale for doing so is to capture diastolic abnormalities in any of the regions of the EDPVR curve (e.g., rapid recoil or early filling phase, diastasis or slow filling, filling due to atrial contraction), as diastolic dysfunction may be due to impairment in any of these phases (see detailed discussion in section 'Computation of indices of diastolic function', chapter 2). Next, we fitted the pressure curve from minimum pressure during diastole to ED versus normalized volume using the Klotz and cubic polynomial models (as described in [76] and [49], respectively). Regarding the Klotz model, as suggested in [76], first, we used coefficients A_n and B_n proposed in their study for normalized volume with the equation $EDP = A_n(EDV)_n^{B_n}$. The values used from the Klotz study were $A_n = 28.2$ and $B_n = 2.79$ for normalized volume in swine data as used in many studies [76, 105]. Using these coefficients, we calculated the predicted pressure values for this segment by implementing the Klotz method. Furthermore, as outlined in the Klotz method, we computed the coefficients α and β separately for each subject utilizing their provided algorithm [76] to calculate the predicted pressure values.

Finally, we fitted the pressure-volume data during diastole using a cubic polynomial as suggested in [49]. In our case, the Klotz model poorly represented the experimental data. For the cubic polynomial model, the fitting was better than the Klotz model. However, the cubic polynomial equation is a representation with 3 coefficients and a constant term for which the physiological interpretation is difficult. Furthermore, both models fit more than one parameter through the curve-fitting process.

In this study, we wanted to use a model that can both represent the *in vivo* LV pressure and

volume measurements accurately portraying the LV EDPVR and depends only on one parameter to represent the EDPVR. Using a normalized volume, we fitted the diastolic PV relation with the following equation

$$P = \alpha V_n^{\beta} \tag{3.1}$$

where,

- P = Pressure from minimum pressure during diastole to the ED;
- $V_n = \frac{V - V_0}{V_{ED} - V_0}$ where V_n is the normalized Volume, V is the LV cavity volume from minimum pressure during diastole to ED, V_0 is the volume at minimum pressure during diastole, and V_{ED} is the volume at ED.
- α is the end-diastolic pressure (EDP).
- β is the only parameter to be fitted.

The independently fitted parameter β is related to the LV passive chamber stiffness.

Quantification of in vivo LV cardiac indices

To evaluate LV indices of cardiac function, LV pressure, and volume traces were used. ED and ES points were identified as described in the section 'Registration of pressure and volume data and *in vivo* pressure-volume loop generation' (chapter 3). From the LV pressure and volume traces, I calculated many LV indices such as ejection fraction (EF), Body surface area (BSA), mean arterial pressure (MAP), stroke volume (SV), cardiac output (CO), cardiac index (CI), ventricular-arterial coupling (VAC), isovolumic relaxation time (IVRT), diastolic volume recovery time (DVRT) [55, 68, 113]. The slope of the ESPVR, E_{es} was determined using Senzaki et al.'s single beat estimation

method [126]. Effective arterial elastance, E_a was calculated using Sunagawa et al.'s method [132]. Following these calculations, VAC was evaluated using VAC=E_a/E_{es} [48]. We calculated the isovolumetric relaxation time constant, τ using Weiss et al.'s (τ_{Weiss}) method described in [150]. The calculation of IVRT (the time interval between AV closure and MV opening [101]) and DVRT (the time interval between ES and the time when the volume is equal to 80% of the stroke volume [102]) were also carried out. To quantify the LV infarct size (%) in subject group MI, open-source software '3D Slicer' (http://www.slicer.org) [43] was used. Cardiac T1 weighted images acquired during the experimental procedure (see section 'Experimental data', chapter 3, figure 3.1) were used as input in 3D Slicer. Segmentations were carried out using both manual and semi-automatic algorithms. At first, regions were selected manually to calculate the mean and the standard deviation (SD) of the signal intensity of healthy and infarcted myocardium. Utilizing these values, the infarcted myocardium was identified as the region with value $\geq$ mean+ 5SD for the healthy myocardium) [65, 71]. After completing the segmentation, a whole model (including both RV and LV) was built in 3D Slicer. Finally, the LV was manually separated and myocardial infarct volume (in % with respect to LV volume) was quantified.

Statistical analysis

We analyzed the data between two subject groups (control and MI) using an unpaired Student's t-test. To do that, first, we tested if our data approximately follows a normal distribution. To test if the data is normally distributed, statistical tests for normality, e.g., the Shapiro-Wilk test, are used along with visual inspection through Q-Q plots, which becomes particularly important considering the small sample size. Q-Q plots, short for Quantile-Quantile plots, compare the quantiles of data to the quantiles of a theoretical normal distribution. If the tested data points fall along a straight line in the Q-Q plot, it suggests that the data is approximately normally distributed. After confirming that the data approximately follows a normal distribution, we proceeded to employ the

two-sample t-test. This test was chosen due to the normal distribution assumption in both groups. The tests were performed in MATLAB. A power analysis was conducted using a two-sample t-test approach. The analysis was performed in G*Power software (latest ver. 3.1.9.7; Heinrich-Heine-Universität Düsseldorf, Düsseldorf, Germany) [42]. G*Power is a free software designed to aid researchers in ensuring their studies have adequate sample sizes to detect meaningful effects and draw reliable conclusions in statistical analyses [42]. The mean, SD, and pooled SD of β were calculated for both subject group control and MI. With a significance level of α=0.05, using a 2-tail t-test and post hoc analysis, the computed achieved power was 0.96 [72]. A post hoc power value of 0.96 with a significance level of 0.05, indicates that, given the observed effect size, sample size, and significance level, there is a 96% probability of detecting a statistically significant result if one exists, given the chosen alpha level. We used a total of N=13 subjects combining both subject groups (n=8 control and n=5 MI) and reported a statistically significant difference in β (p-value = 0.001 $<\alpha$ = 0.05) between the two subject groups. Reporting the Pearson correlation coefficient along with the p-value is crucial while dealing with smaller sample sizes. While the p-value's interpretation varies with sample size, the correlation coefficient provides additional insight into the relationship's strength and direction, enriching the interpretation within the sample size constraints. Thus, correlation coefficients were evaluated using the Pearson correlation coefficient to examine the degree of correlation of identified β from the proposed EDPVR model with different LV diastolic and systolic indices for validation purposes. All values are reported as Mean $\pm$ SD. A p-value level $<$0.05 was considered statistically significant.

Results

All quantified values are reported as Mean $\pm$ SD. The mean body mass for control and MI groups were 46.96 ± 3.80 kg and 59.66 ± 7.43 kg, respectively. The mean LV ejection fraction was

50.53 ± 7.35 (%) and 41.70 ± 10.72 (%) for the control and MI group respectively. The mean heart rate (HR) was 87.28 ± 3.24 beats/min and 89.82 ± 18.91 beats/min for the control and MI group, respectively. We also calculated many LV systolic and diastolic functional indices. Statistically significant differences were observed between the two groups and reported.

LV pressure-volume loops and diastolic pressure-volume relation

Starting from the pressure and volume data, we reconstructed beat-averaged PV loops for each of the healthy and infarcted subjects. All the PV loops had key features showing the validity of the proposed pipeline. Each PV loop showed evident isovolumic contraction, an ejection phase, and isovolumic relaxation followed by ventricular filling. Fig. 3.4a and Fig. 3.4c show LV pressure and volume plotted with their first derivatives for subject groups control and MI, respectively. Fig. 3.4b and Fig. 3.4d show the corresponding PV loops for the same subjects. Here the median pressure profile along with its 95% confidence interval was plotted against the volume that was generated from CIM and later interpolated according to the median cardiac cycle length. As previously described in the section 'Registration of pressure and volume data and *in vivo* pressure-volume loop generation' (chapter 3), the beginning of the atrial systole, ED, and ES phases were identified in the CINE MRI images and shown in Fig. 3.4. The mean end-diastolic pressure (EDP) and end-systolic pressure (ESP) calculated for the control group were 7.36 ± 1.42 mmHg and 67.15 ± 9.80 mmHg respectively. Whereas, the mean EDP and ESP calculated for the MI group were 15.75 ± 9.82 mmHg and 93.66 ± 9.07 mmHg respectively. The mean end-diastolic volume (EDV) and end-systolic volume (ESV) calculated for the control group were 100.21 ± 13.87 ml and 49.73 ± 11.61 ml respectively. Whereas, the mean EDV and ESV calculated for the MI group were 165.34 ± 27.29 ml and 98.42 ± 32.61 ml respectively. The mean slope of the ESPVR (E_{es}) for the subject group control and MI were 1.42 ± 0.53 and 1.07 ± 0.47, respectively. Effective arterial elastance (E_a) computed for the subject group control and MI were 1.39 ± 0.40 and 1.41 ± 0.17, respectively.

Finally, the ventricular-arterial coupling (VAC=E_a/E_{es}) calculated for the subject group control and MI were 1.05 ± 0.35 and 1.54 ± 0.65, respectively. The mean isovolumic relaxation time (IVRT) computed for the subject group control and MI were 99.50 ± 8.96 ms and 113.8 ± 10.38 ms, respectively. The mean diastolic volume recovery time (DVRT) was 235.88 ± 39.05 ms in the subject group control and 339.2 ± 193.55 ms in the group with MI. The mean maximum rate of increase in volume during diastole ($dVdt_{\text{max}}$) was 358.525 ± 45.26 ml/s and 536.24 ± 72.34 ml/s in the subject group control and MI, respectively. The mean maximum rate of pressure decline during diastole ($dPdt_{\text{min}}$) and τ calculated in subject group control were -1287.51 ± 271.60 mmHg/s and 31.71 ± 5.20 ms respectively. The mean $dPdt_{min}$ and τ were -2009.30 ± 208.72 mmHg/s and 35.73 ± 3.40 ms respectively in the MI group.

Klotz predicted fit, Cubic polynomial fit, and Proposed fit of diastolic pressure-volume relation (PVR)

We fitted the diastolic PV relation using the Klotz method, a cubic polynomial, and the proposed models (Figure 3.5). The Klotz models with normalized coefficients A_n and B_n fitted the data poorly with respect to the Klotz equation obtained by calculating the coefficients α and β separately for each subject. Thus, the fitted EDPVRs with normalized coefficients A_n and B_n for the Klotz model were not shown in Figure 3.5.

We computed the root-mean-squared error (RMSE) between the *in vivo* measurements and the Klotz predicted LV pressure, the cubic model, and the proposed model. We also calculated R^2 and adjusted R^2 for all cases. For the subject group control, the cubic polynomial fit of the EDPVRs resulted in smaller errors (0.30 ± 0.08 mmHg) compared to the Klotz model (0.98 ± 0.44 mmHg) and the proposed model (0.38 ± 0.13 mmHg), although the difference between the cubic polynomial and the proposal model is small. For the subjects with MI, the cubic polynomial fit of

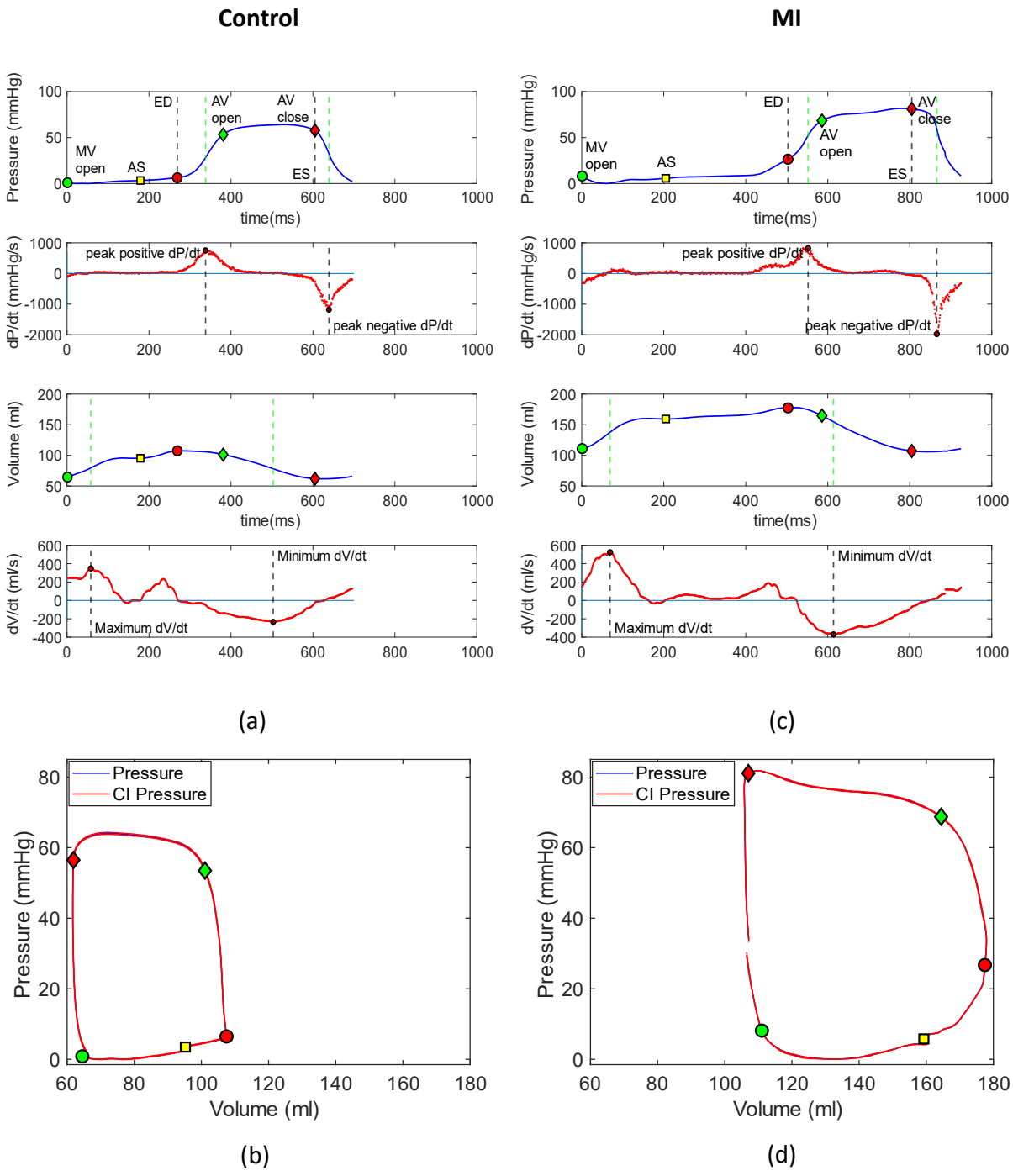

Figure 3.4: LV pressure and its first derivative, LV volume and its first derivative (a), and PV loop for a control subject (b). LV pressure and its first derivative, LV volume and its first derivative (c), and PV loop for a subject with MI (d).

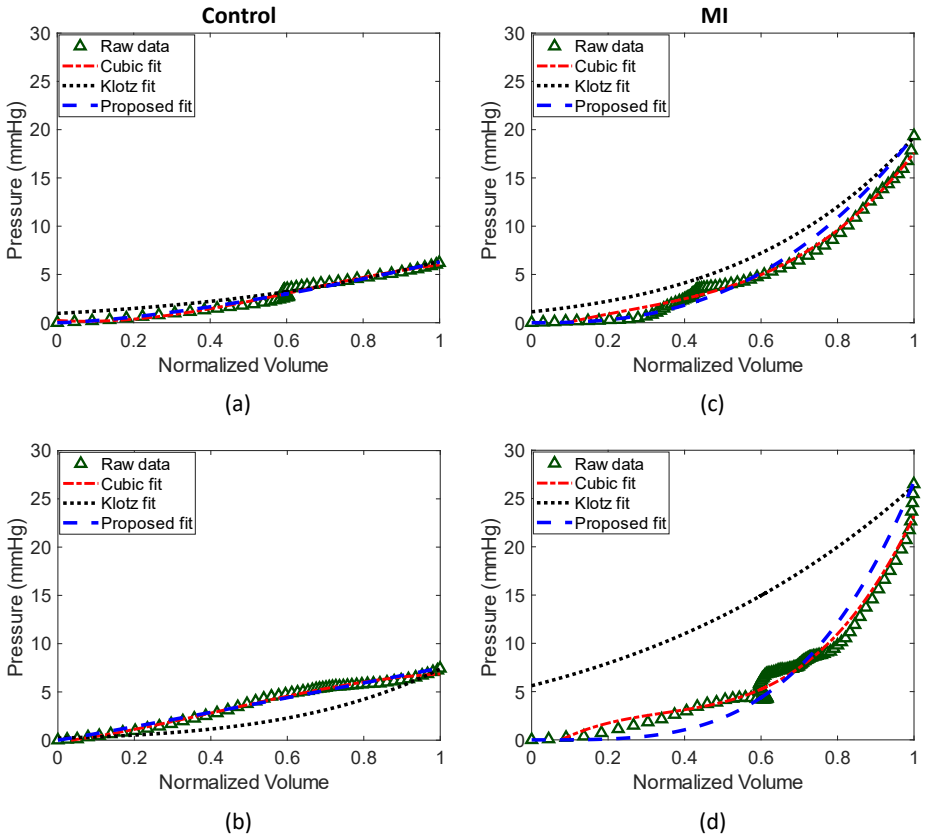

Figure 3.5: Raw diastolic PV data overlaid to the Klotz model [76], a cubic polynomial model [49], and the proposed model for two control subjects (a, b) and two subjects with MI (c, d)

the EDPVRs again resulted in smaller errors (0.43 ± 0.28 mmHg) compared to the Klotz model (3.79 ± 3.74mmHg) and the proposed model (0.79 ± 0.53). In particular, the Klotz model did not represent well the *in vivo* EDPVRs for the subjects with MI. The proposed model, despite fitting only one parameter, resulted in an error comparable to the cubic model, although slightly larger.

The calculated RMSE values from the fitted models are also reflected in Figure 3.5. Figure 3.5a and Figure 3.5b represent EDPVR fits for two control subjects and Figure 3.5c and Figure 3.5d represent EDPVR fits for two subjects with MI. In all these cases, the cubic polynomial and the proposed model represented the experimental data more closely compared to the Klotz model.

Next, in Fig. 3.6a, we plotted all the EDPVR's for subject groups control and MI together using the proposed model representing the relationship between LV pressure and normalized volume. Three out of five LV EDPVRs for subjects in the MI group shifted to the left compared to the LV EDPVRs for subjects in the control group.

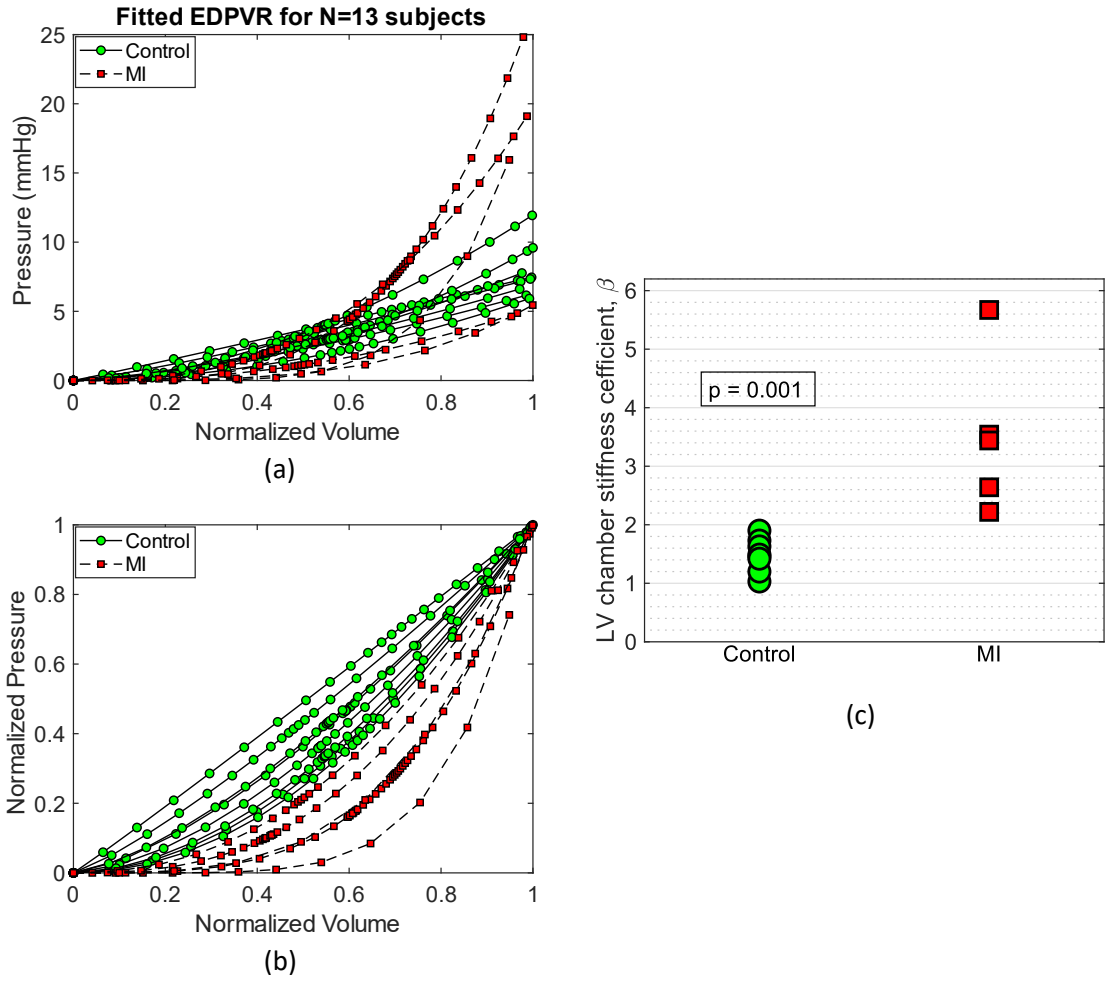

Figure 3.6: Fitted EDPVR with (a) normalized volume, (b) normalized pressure and normalized volume, and (c) LV passive chamber stiffness coefficient β calculated from the proposed model for subject group control and MI

From the EDPVR curves of the MI group, the increased slope becomes evident which supports

what has been previously reported in various studies regarding MI [47, 9, 93]. Next, in Fig. 3.6b we normalized both pressure and volume and plotted all the EDPVRs for subject groups control and MI together using the proposed model. By normalizing pressure and volume and plotting the EDPVR curves together, one can directly compare the diastolic properties of the myocardium between the control and MI groups, independently of absolute pressure and volume values. In the normalized plot, the EDPVR curves for the control group are closer to a straight line. In contrast, the EDPVR curves for the MI group exhibited a more non-linear trend with a steeper ED slope. This suggests that the myocardium in the MI group has altered diastolic properties, such as increased stiffness or decreased compliance at ED, compared to the control group. The steeper slope indicates that a greater increase in pressure occurs for a given increase in volume, reflecting impaired diastolic function and reduced myocardial distensibility. In contrast to the cubic model and Klotz predicted EDPVR, only one parameter (β) was determined for the proposed model, which can be directly associated with the passive chamber stiffness. We also observed a statistically significant difference in β ($p = 0.001$, $p < 0.01$) between the two subject groups (control and MI). The mean values of the coefficient α (which is the EDP for each subject) for control and subjects with MI were 7.36 ± 1.42 mmHg and 15.75 ± 9.82 mmHg, respectively. Fig. 3.6c represents all β coefficients for the control and MI groups together. The mean β for the control and MI groups were 1.48 ± 0.26 and 3.49 ± 1.34, respectively ($p = 0.001$ between the two groups).

We also calculated the diastolic chamber stiffness dP/dV. The mean dP/dV calculated from the fitted EDPVR using the proposed model at ED were 0.29 ± 0.06 mmHg/ml vs 1.23 ± 1.01 mmHg/ml (control vs MI), which also showed a statistically significant difference (p = 0.02) between the two subject groups.

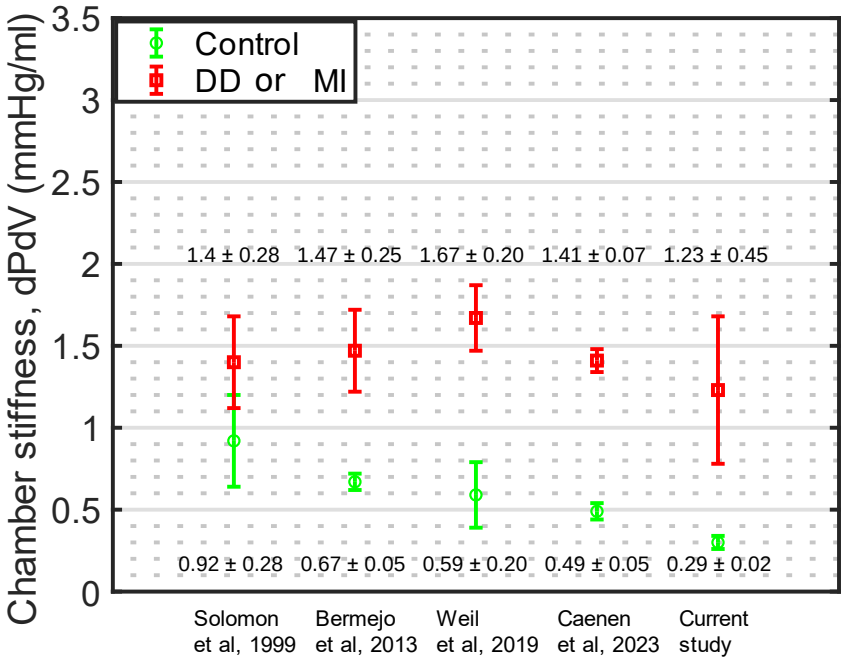

Figure 3.7: LV chamber stiffness dPdV from similar studies and calculated from the proposed model.

Fig. 3.7 illustrates dPdV values across different studies using swine subjects [11, 20, 129, 149] (dPdV values are reported as mean $\pm$ SEM, where SEM= Standard error of the mean). All of these studies investigated swine models with either MI [13, 129, 149] or DD [11] and reported elevated dPdV among the diseased groups using an exponential model fit [11, 13, 149].

Relationship between β and different LV diastolic indices

A larger β value corresponds to an increased infarct size, absolute value of dPdt$_{min}$, τ, isovolumic relaxation time (IVRT), diastolic volume recovery time (DVRT), $dVdt_{\text{max}}$, and ventricular-arterial coupling (VAC). On the contrary, as β increased, EF decreased. We also reported a strong negative correlation between VAC and EF. We reported the Pearson correlation coefficients and significant

p-values (p-value <0.05) in support of our argument for each of these correlations in Table 3.1 and Figs. 3.8, 3.9, and 3.10.

Table 3.1: Relationship between β and different LV indices. *p <0.05, †p <0.01, ‡p <0.001.

Parameters (N=13)	**r**
Infarct size(%)*	0.90
EF†	-0.67
$dPdt^*_{min}$	0.61
τ^*	0.65
IVRT†	0.71
DVRT†	0.70
$dVdt^\dagger_{max}$	0.72
VAC†	0.71
(VAC vs EF‡	-0.99)

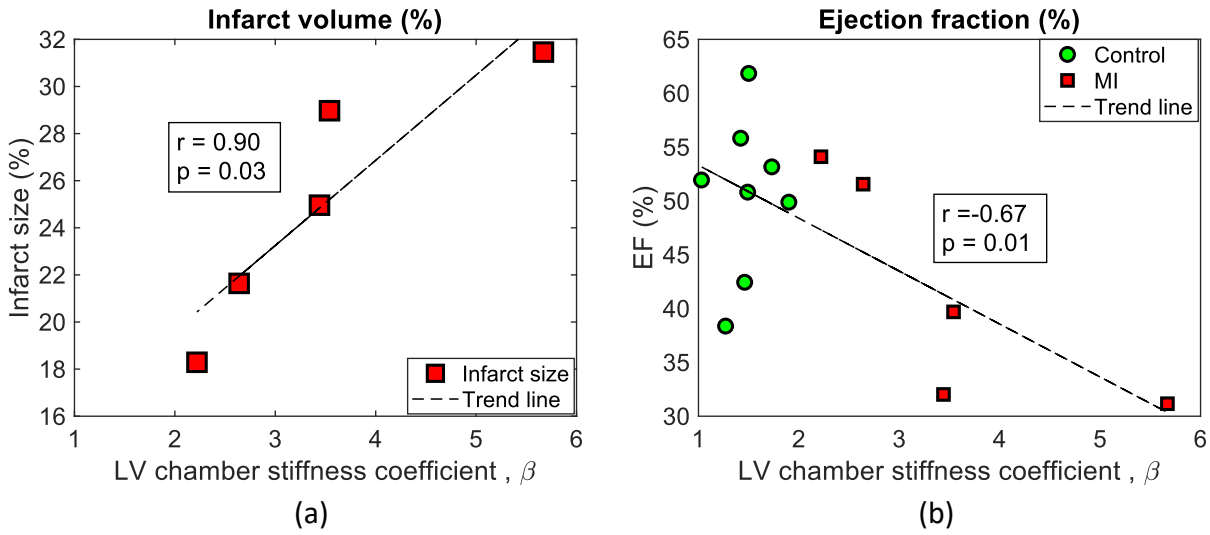

Figure 3.8: Relationship between (a) β and infarct volume (in %); (b) β and EF(%)

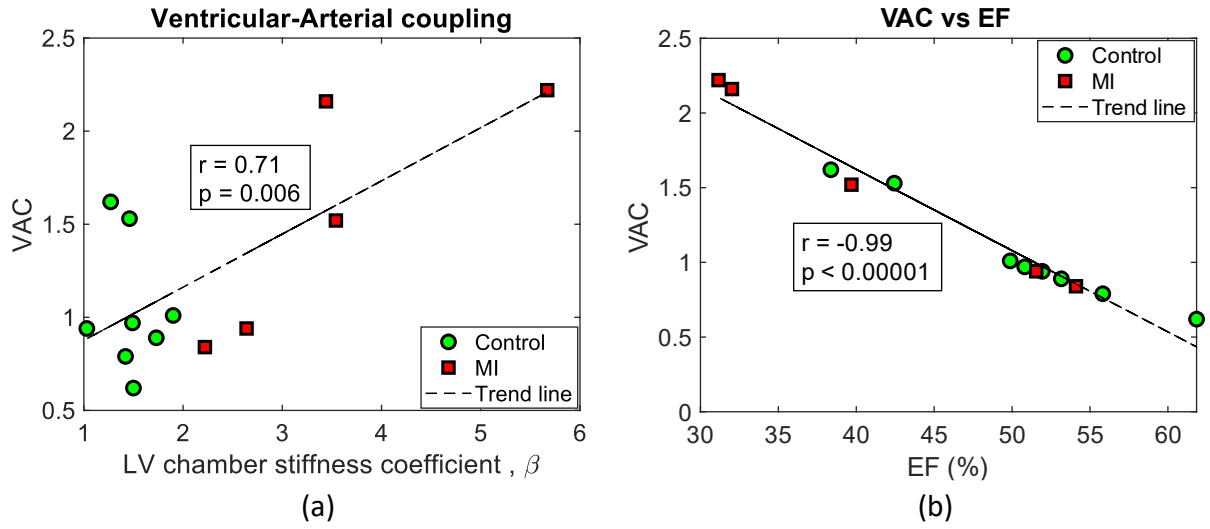

Figure 3.9: Relationship between (a) β and VAC; (b) EF and VAC

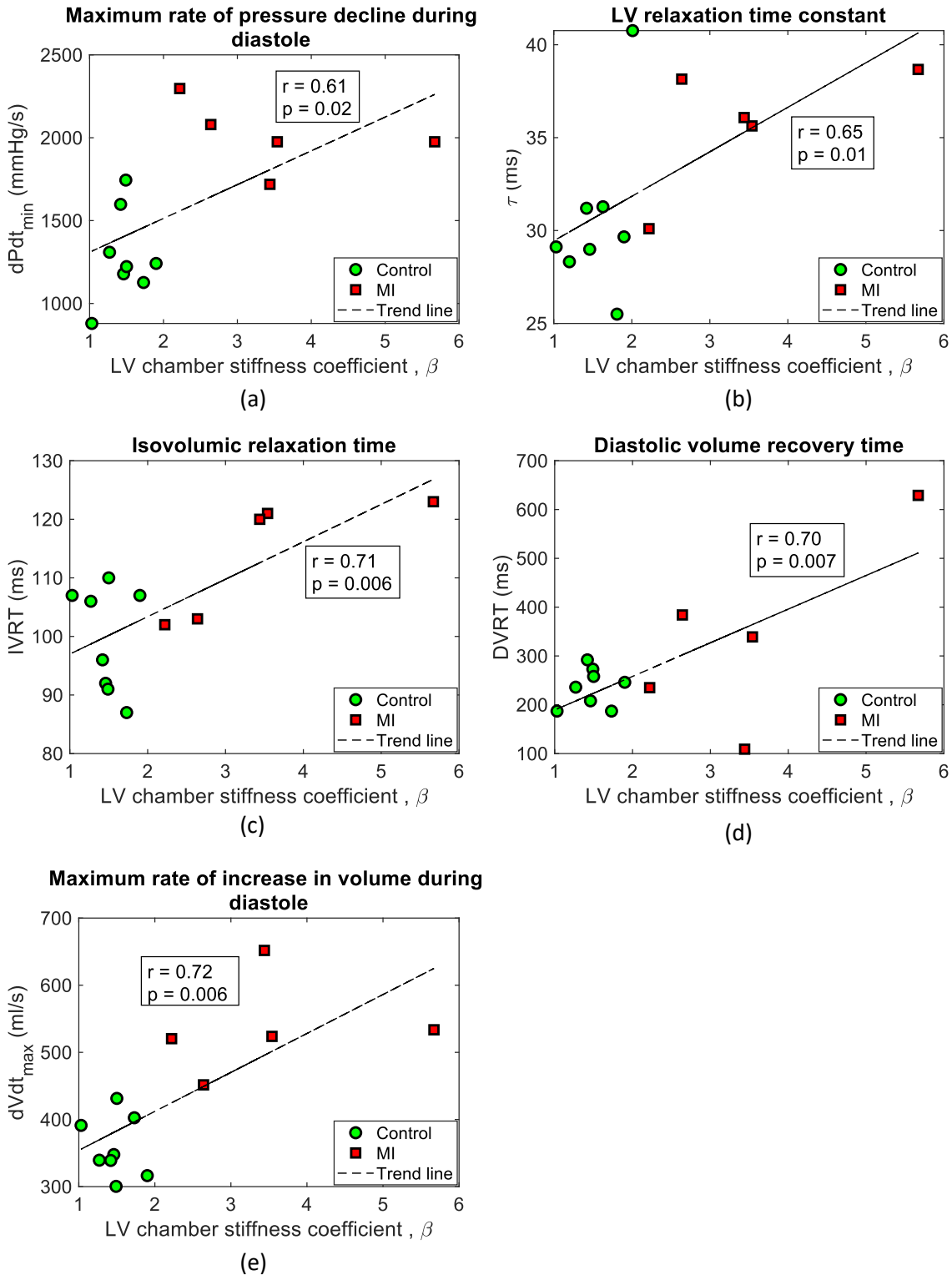

Figure 3.10: Relationship between β and different LV diastolic indices

Comparison of β with dPdV

The diastolic chamber stiffness – dPdV at ED – was calculated from the proposed model for each subject in the control and MI groups. We compared the computed dPdV from the proposed model with previous studies available in the literature and using swine subjects (see Fig. 3.7). The dPdV reported at ED presented in this study aligns well with previously reported ranges documented in the literature for both the control and MI groups.

Further, we compare dPdV at ED with the coefficient β. Fig. 3.11a shows the variation in dPdV as a function of β computed from the proposed model. We observed a strong positive correlation between β and dPdV (r = 0.87, p <0.0001). Next, to understand if other possible measures of cardiac function correlate to β, we analyzed EDP/SV as a function of β (Fig. 3.11b) and EDP/SV as a function of dPdV at ED (Fig. 3.11c). We observed a moderate positive correlation between EDP/SV and β and a strong positive correlation between EDP/SV and dPdV at ED. These positive correlations suggest that as LV chamber stiffness increases (indicating impaired filling), there is a corresponding increase in LV end-diastolic pressure relative to stroke volume. In other words, the heart is working against higher resistance during diastole, leading to elevated LV pressure levels for a given LV volume.

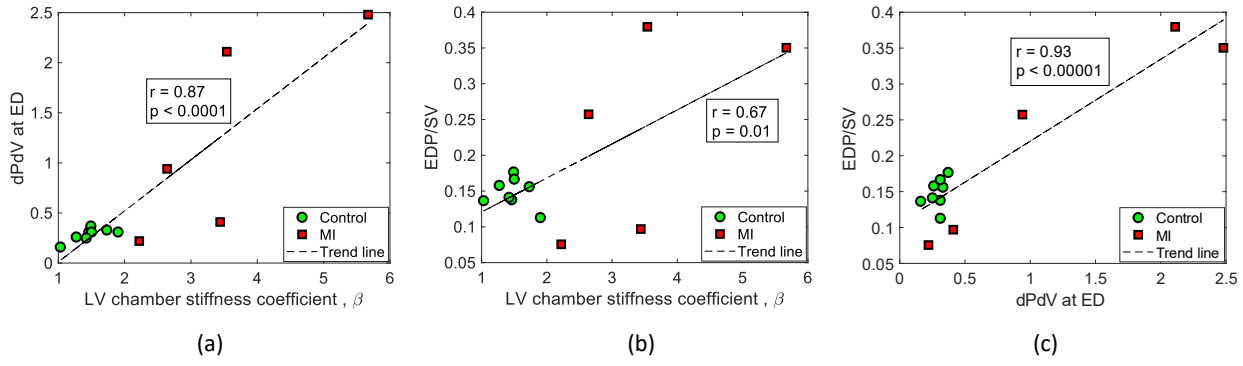

Figure 3.11: Relationship between β and dPdV with EDP/SV.

Discussion

This study describes a new curve-fitting modeling framework for the EDPVR where only one parameter, β, needs to be determined. The model represents the portion of the PV loop extending from the minimum pressure during diastole to ED. The constructed model can be referred to as an "averaged diastolic PV curve" or "predicted diastolic PV relationship". The coefficient β in the proposed EDPVR model characterizes the LV pressure-volume non-linearity during rapid filling, diastasis, and atrial systole. Unlike dPdV, it doesn't solely represent the LV chamber stiffness at ED, but represents the ventricular response across the whole filling phase, offering a comprehensive insight beyond a single cardiac phase.

A fiber optic pressure transducer was used for real-time 3T MRI-guided cardiac catheterization. Thus, intraventricular pressure was recorded at the same time as the imaging data was acquired [87]. This provides the opportunity to register the pressure and volume acquired at the same time for each of the subjects, unlikely many other studies in which pressure and image acquisition are sequential [147]. The CINE MR images acquired during the procedure (see section 'Experimental data', chapter 3) were high resolution and therefore ideal for LV and volume data segmentation using CIM. Given the high-quality data and processing pipeline, the PV loops built in this study exhibited all the well-known features of classic PV loops like an evident isovolumic contraction, ejection, isovolumic relaxation, and ventricular filling phases. Along with these features, our PV loops showed the presence of the "atrial kick". This was previously shown in Fig. 3.4b, d and further illustrated in Fig. 3.12.

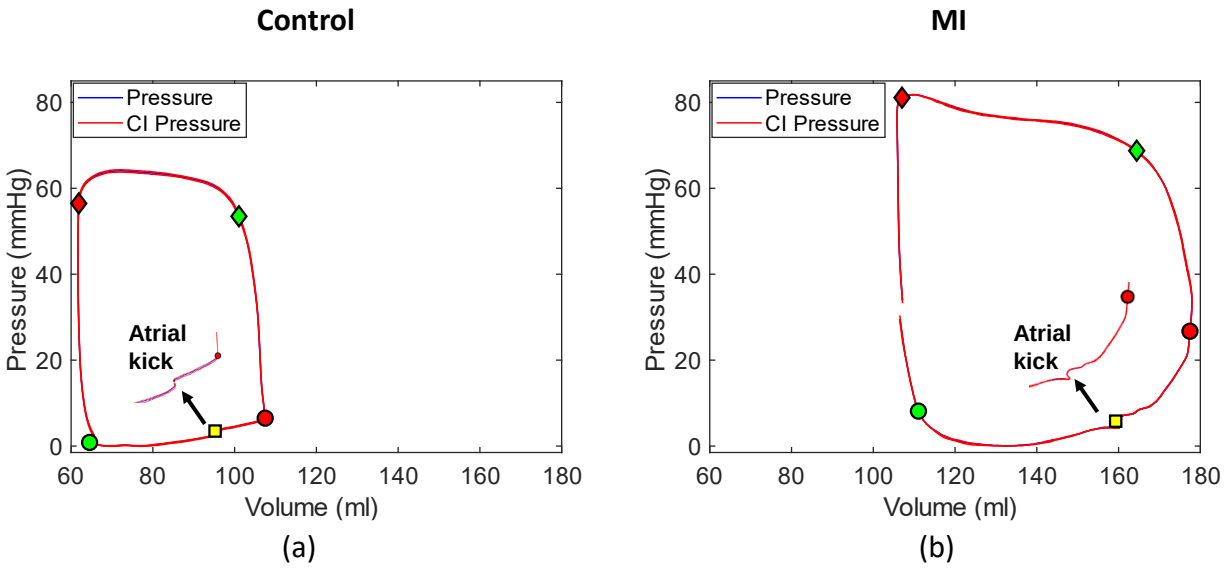

Figure 3.12: PV loop showing classical features and an evident atrial kick for a control subject (a) and a subject with MI (b).

The diastolic (passive) chamber stiffness of the myocardium is one of the main indicators of diastolic abnormalities. Although the clinical application of the EDPVR is not considered feasible yet (see previous detailed discussion in section 'Pressure Volume loop', chapter 2), diastolic (passive) chamber stiffness of the LV is being quantified *in vivo* from the EDPVR [19].

Several mathematical models, including mono-exponential, power, and linear models, are utilized to fit the LV diastolic phase and predict the PV relationship in various studies [73, 134]. These models often involve fitting multiple parameters to the available PV data during diastole, may depend on the patient ventricle size, and may suffer from the loss of exponential PV relation at low pressure. In our study, we focus on identifying the diastolic (passive) chamber stiffness coefficient, which serves as the only fitted parameter. After discussing the exponential model (see section '*In vivo* end-diastolic pressure-volume relations (EDPVR)', chapter 3), we first evaluated EDPVR following the Klotz model and Cubic polynomial model. In the first case, the Klotz model was

unable to represent the experimental data accurately. Although the cubic polynomial model was able to represent the experimental data more closely, we aimed to develop a model requiring fewer parameters for fitting. Parameters evaluated from the proposed model can be directly linked to diastolic (passive) chamber stiffness.

As previously reported in many studies, LV distensibility is greatly impacted by LV chamber geometry [112]. If LV walls are thicker compared to the control group, it becomes harder to push out blood during systole. This may give rise to the leftward and upward shift of the EDPVR as depicted for 3 of the subjects in the MI group (Fig. 3.6a). On the contrary, EDPVR for 2 of the subjects from the MI group shifted rightward and downward. The variations in EDPVR observed among subjects in the MI group can be attributed to the diverse responses of the myocardium to MI. Overall, the combination of increased passive chamber stiffness and both the leftward and upward, rightward and downward shift in the EDPVR curve in the MI group reflects the possible complex interplay between myocardial remodeling, fibrosis, hypertrophy, and altered diastolic properties following MI.

In Figure 3.6b by normalizing both pressure and volume and plotting the EDPVR curves together, we directly showed a comparison of the diastolic properties of the myocardium between the control and MI groups, independent of absolute pressure and volume values. This approach allowed for a more direct assessment of differences in myocardial diastolic chamber stiffness or compliance between the groups, which may not be evident when plotting the curves without normalization. Additionally, observing a steeper slope in the MI group's EDPVR curve compared to the one of the control group supports the notion of altered diastolic function associated with MI.

The computed diastolic (or passive) chamber stiffness coefficient β ranged between 1.03-1.90 for the control group and 2.22-5.67 for the subject group MI (see Fig. 3.6c). Thus, this study focused on investigating further the correlation between the increase in β (N=13) and different LV diastolic

and systolic indices across the two subject groups. Significant results were observed and reported. First, an increase in β suggests a decrease in compliance which is consistent with the upward, leftward of the EDPVR [9, 93, 118, 50](Fig. 3.6a,b). Next, the infarct volume (%) quantified from 3D slicer showed a strong correlation with β (r=0.90, p=0.03) (Fig. 3.8a). This suggests that an increase in β is consistent with an increase in infarct volume (%) in the subject group with MI. We observed a decline in LV ejection fraction from 50.53±7.35% in the subject group control to 41.70±10.72% in the subject group MI ($p < 0.05$). We found a moderate negative correlation between β and ejection fraction (r=-0.67, p=0.01) (Fig. 3.8b). This finding is consistent with other observations that a decline in LV compliance leads to a decline in ejection fraction in patients with MI [3, 30].

Further, we evaluated the peak instantaneous rate of LV pressure decline, $dPdt_{min}$ (peak negative dPdt), and isovolumic relaxation time constant, τ between the two groups. Our study suggests that an increase in β causes significantly higher peak rate of pressure decline $dPdt_{min}$ (r= 0.61, p=0.02) [118](Fig. 3.10a). We also reported a positive correlation between β and τ (r=0.65, p=0.01) (Fig. 3.10b) suggesting that an increase in β is coincident with prolonged τ. This is consistent with DD and HFpEF studies [118]. Patients with DD and HFpEF show abnormal or impaired relaxation which has been previously quantified by an increase in isovolumic relaxation time [123]. Our study shows a significant correlation between β and IVRT (r=0.71, p=0.006) (Fig. 3.10c) inferring impaired relaxation which may cause DD. The studies done to investigate DD likewise showed increased diastolic volume recovery time (DVRT) [74]. This is consistent with our finding as we report the positive correlation between β and DVRT (r= 0.70, p=0.007) (Fig. 3.10d). We evaluated the peak instantaneous rate of increase in LV volume during diastole, $dVdt_{\text{max}}$ and the finding of our study suggests a significant correlation between β and $dVdt_{\text{max}}$ (r=0.72, p=0.006) (Fig. 3.10e). Studies reported previously increased $dVdt_{\text{max}}$ among patients with DD [53]. We also reported a significant correlation between β and VAC (r=0.71, p=0.006)

(Fig. 3.9a). VAC is a representation of cardiac performance as it is defined by both ventricular and arterial elastances. Thus, such a significant correlation suggests that an increase in VAC can be an indication of diastolic abnormalities and impaired LV performances. This finding is consistent with many of the studies reporting increased VAC among patients with MI, DD, and HFpEF [4, 95]. Also with the decline in EF, there is a progressive increase in VAC [5]. We found a strong negative correlation between VAC and EF (r=-0.99, p $<$0.0001) (Fig. 3.9b).

In conclusion, our findings suggest that β estimated from the proposed EDPVR model has the potential to indicate diastolic abnormalities.

Study Limitations and future work

For the subject group MI, a different anesthetic regime was used. This was necessary to achieve the desired heart rate and keep the subjects stable. Although the different anesthetic regimes have been previously validated in several studies and protocols in both control and diseased swine subjects [1, 83, 124], they may still be a confounding factor.

The cohort size in our study (N=13) is small. We conducted a power analysis and computed the achieved power of the study as 0.96 using G*Power software [72] (see details in section 'Statistical analysis', chapter 3). As the p-value depends on the sample size, this power analysis suggests that we had an adequate sample size to draw a reliable conclusion and thus report statistically significant results. However, a larger cohort size is necessary to improve the statistical power of the reported results and strengthen the outcomes of this study.

Infarct size and location varied in the subject group MI. One of the reasons for this variability is the location of the infarct induction. During the experimental procedure, a branch of either the left anterior descending (LAD)(for 3 subjects) or left circumflex (LCx)(for 2 subjects) artery was

selected for infarct induction. This variability could have contributed to the reported differences in β values and the leftward or rightward shift of the fitted EDPVR curves.

CHAPTER 4: LV STRAINS DURING ATRIAL SYSTOLE

In this chapter, we focus on computing cardiac deformation (strain) during atrial systole, which constitutes the second main objective of this thesis.

Experimental data

For this study's second objective, two subject groups were again utilized: a control group and a group with myocardial infarction (MI).

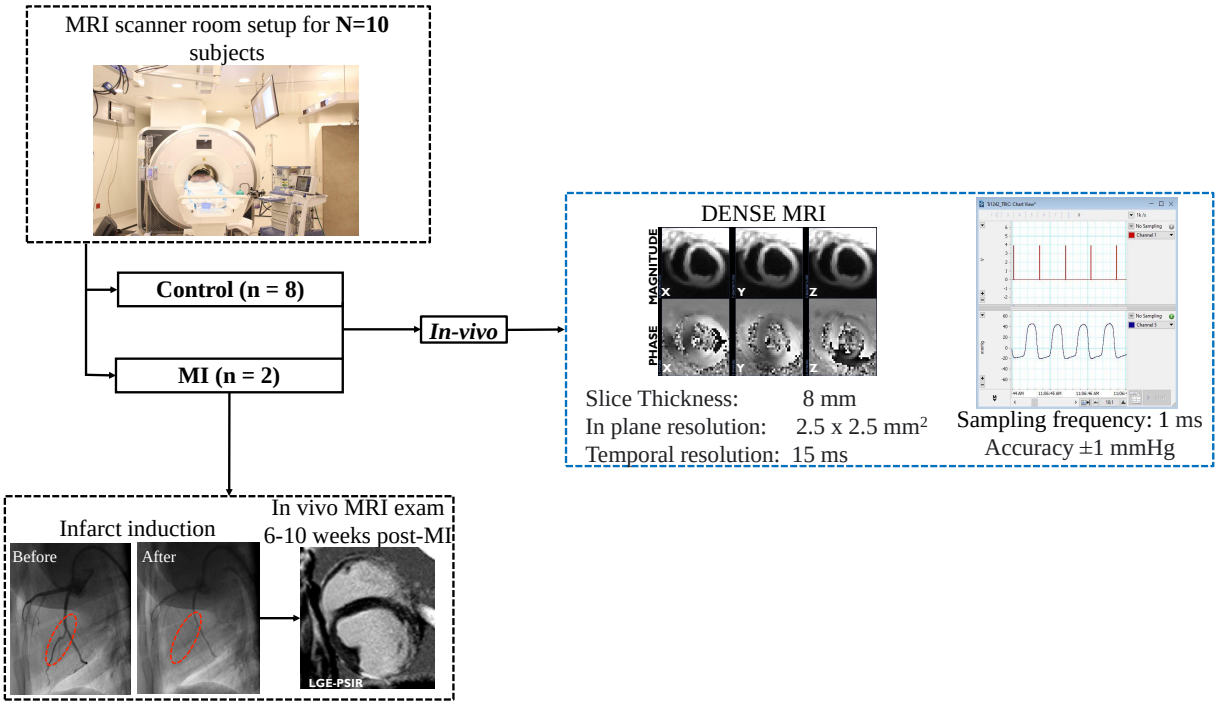

Figure 4.1: Flow chart representing the acquisition of the data used for computing cardiac deformation during atrial systole

Figure 4.1 provides a visual representation of the data acquisition procedure of this study. In total, ten (N=10) subjects were included, with eight (n=8) as the control group, and two (n=2) representing the MI group. The research conducted in this chapter primarily employed cardiac DENSE MRI alongside pressure data acquired through *in vivo* cardiac catheterization. Throughout the MRI data acquisition, intraventricular pressure was continuously recorded [87].

Methodology and Data Analysis

The calculation of cardiac strain during atrial systole relies on the analysis of cardiac DENSE MRI data obtained from in-vivo MRI scans. The subsequent sections detail the methodology employed to calculate cardiac strain by discussing:

1. Segmentation and image analysis of cardiac DENSE MRI data for the assessment of cardiac strain and deformations during atrial systole;
2. Registration of LV pressure measured during DENSE MR acquisition and cardiac strain during atrial systole;
3. Statistical analysis.

Segmentation and image analysis of cardiac DENSE MRI data for the assessment of cardiac strain and deformations during atrial systole

A total of ten (N=10) female Yorkshire swine subjects were included in this study. Among them, eight (n=8) were healthy (control group), while two (n=2) had myocardial infarction (MI group). Full-field, voxelwise displacement data were obtained via cine DENSE MRI during the preclinical experiments as outlined in the section 'Experimental data' (chapter 4). Long-axis (LA) images

were acquired at intervals of 30° in the circumferential direction, while short-axis (SA) images were obtained with an 8mm separation and are normal to the long axis. The cine DENSE MRI data were segmented using DENSEanalysis [58, 130], an open-source MATLAB-based [91] application widely utilized in the DENSE MRI community.

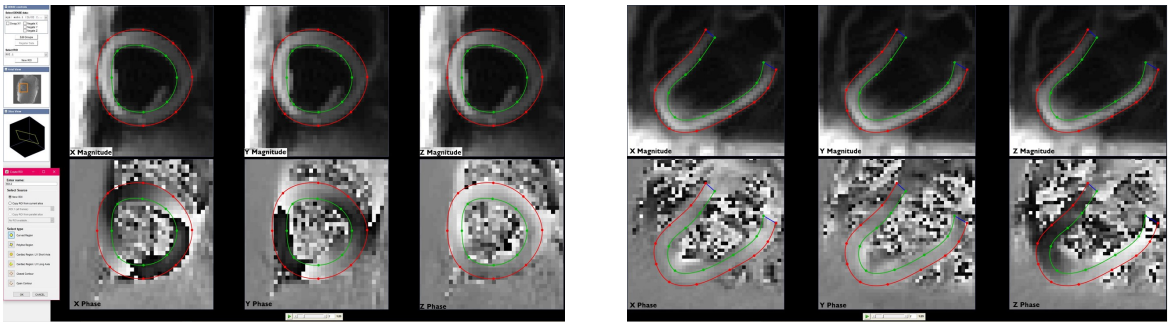

(a) LV short axis (SA)

(b) LV long axis (LA)

Figure 4.2: LV short (a) and long axis (b) views inside the DENSE segmentation tool. Region of interest (ROI) segmentations are overlaid to magnitude (top) and phase (bottom) images encoding voxelwise displacements in the in-plane (xy) and out-of-plane (z) directions.

LV regions of interest (ROIs) were segmented utilizing both the LA and SA slices. For segmentation, dedicated LA or SA cardiac region segmentation tools were employed. The endocardial and epicardial contours were outlined manually by selecting points defining the splines on the endocardial and epicardial walls. The adjustable spline nodal points within the DENSEanalysis tool facilitated close tracking of the LV epicardial and endocardial contours. Subsequently, a motion-guided segmentation was carried out to segment the images across the cardiac cycle. Starting from a selected frame, this process generated an outline for each time frame using the DENSE displacement vectors. During motion-guided segmentation, a linear smoothness value of 0.9 and an order polynomial equal to 8 were utilized. Following automated

segmentation, the newly generated contours across all cardiac phases were carefully inspected. Any contours deviating from the endocardial and epicardial boundaries were manually adjusted. This manual adjustment was iteratively repeated for each ROI point until a satisfactory segmentation was achieved. Figures 4.2a and 4.2b depict the DENSEanalysis tool featuring magnitude and phase images on LV short-axis and long-axis images, respectively. Following iterative manual adjustment of the motion-guided segmentation, the displacements of individual myocardial voxels in 3D are computed across time within the DENSE analysis toolbox. This involved running an analysis to reconstruct 3D Lagrangian displacements throughout the cardiac cycle with a linear smoothness value set to 0.9 and a polynomial order of 10. Initial LV strain values during atrial systole were computed using the DENSEanalysis toolbox, employing a cylindrical reference system based on LV geometry. By differentiating the Lagrangian displacement field, longitudinal (E_{LL}), circumferential (E_{CC}), and radial (E_{RR}) strains are computed. The DENSE toolbox automatically subdivides these strain values transmurally and across the American Heart Association (AHA) regions [110]. Following manual segmentations, the delineated regions were saved as .mat files. Subsequently, these files were processed for registration with intraventricular pressure data acquired during the DENSE MR acquisition. Finally, the strain values derived from the registered data were also compared to existing literature values.

Registration of intraventricular pressure acquired during DENSE MR acquisition and cardiac strains during atrial systole

The calculation of the pressure data utilized in this chapter followed the identical procedure outlined in the section 'Generation of pressure curve' (chapter 3). However, in this case, the pressure traces were obtained during cardiac cine DENSE MRI acquisition (instead of cine MR acquisition) and were extracted based on the beginning and end of the DENSE MR acquisition

time for each subject. For the registration of the generated pressure traces following the procedure detailed in the section 'Generation of pressure curve' (chapter 3) and the strain data detailed in the section 'Segmentation and image analysis of cardiac DENSE MRI data for the assessment of cardiac strain and deformations during atrial systole' (chapter 4), a MATLAB code [91] was built. The trigger delay, which represents a predefined interval between the occurrence of a specific physiological event and the initiation of the MRI data acquisition process, was utilized to synchronize the registration of DENSE MRI data with pressure data acquired during atrial systole. For every subject within the two subject groups (control and MI), a trigger delay was set during the data acquisition to ensure that images were captured during atrial systole.

Statistical analysis

Data from the DENSE MRI segmentations in both the short and long axis are divided and presented by strain type E_{LL}, E_{CC}, and E_{RR}. Strain values at peak atrial systole represent the cardiac phase with maximal ventricular filling. The Kruskal-Wallis test is employed to determine the statistical significance of differences in LV strains and strain rates during peak atrial systole between the two groups. Functioning like a T-test and Analysis of Variance (ANOVA), this test evaluates whether there are notable differences among the medians of two or more datasets. In addition, the Kruskal-Wallis test is non-parametric, meaning it does not rely on assumptions regarding the normal distribution of the data. We reported mean peak atrial systolic circumferential and radial strains (E_{CC}, E_{RR}) and strain rates ($\dot{E}_{\mathrm{CC}}$, $\dot{E}_{\mathrm{RR}}$)(s^{-1}) quantified from mid-ventricular SA slices, and the mean peak atrial systolic longitudinal and radial strains (E_{LL}, E_{RR}) and strain rates ($\dot{E}_{\mathrm{LL}}$, $\dot{E}_{\mathrm{RR}}$)(s^{-1}) quantified from LA slices for the subjects in the control group. The average was computed across 6 AHA regions in mid-ventricular SA slices and 7 AHA regions in LA slices for each subject. Next, for the subjects in the MI group, we analyzed variations in LV strains across different myocardial regions (6 AHA segments in mid-ventricular

SA slices where segment 1 is anteroseptal and segment 6 is anterior; and 7 AHA segments in LA slices where segment 1 is the basal septal segment). We reported the mean peak atrial systolic strain values, i.e., peak E_{CC}, E_{RR} and strain rates, i.e., $\dot{E}_{\mathrm{CC}}$, $\dot{E}_{\mathrm{RR}}$ (s^{-1}) quantified from identified infarcted regions in mid-ventricular SA slices as well as mean peak atrial systolic E_{LL} and $\dot{E}_{\mathrm{LL}}$ (s^{-1}) quantified from identified infarcted regions in LA slices. The tests were performed in MATLAB. All values are reported as mean $\pm$ SD. We also calculated the median, along with the first (Q1) and third (Q3) quartiles, to summarize the central tendency and variability of the data across the subject groups (reported as Median [Q1, Q3]). A p-value of less than 0.05 was considered statistically significant and reported.

Results

Segmentation and data analysis were conducted on a cohort comprising N=10 subjects in 2 groups (n=8 control, and n=2 MI). Strain values were characterized as longitudinal (E_{LL}), circumferential (E_{CC}), and radial (E_{RR}) strains for the control and the MI group. The following sections include the results in detail.

LV strain during atrial systole

Following the procedures outlined in section 'Segmentation and image analysis of cardiac DENSE MRI data for the assessment of cardiac strain and deformations during atrial systole' (chapter 4), three mid-ventricular slices were segmented using the DENSE analysis toolbox for each subject to calculate circumferential (E_{CC}) and radial (E_{RR}) strains. Additionally, to compute longitudinal strain (E_{LL}), LA slices from subjects in both groups underwent processing. Subsequently, as detailed in the section 'Registration of intraventricular pressure acquired during

DENSE MR acquisition and cardiac strains during atrial systole' (chapter 4), strain and intraventricular pressure traces during atrial systole were registered in time by utilizing the trigger delay for each subject during the data acquisition phase. This process allows us to connect changes in ventricular strains to changes in intraventricular pressure and confirm the robustness of the data and processing pipeline. In Figs. 4.3-4.4 and Fig. 4.5, LV pressure traces synchronized with E_{RR} and E_{CC} computed during atrial systole are reported for 8 subjects in the control group and 1 subject in the MI group. In all cases, we note that E_{CC} is positive whereas E_{RR} is negative during atrial systole. These observations are in agreement with the expansion of the LV cavity ($E_{\text{CC}} > 0$) and "thinning" of the LV wall ($E_{\text{RR}} < 0$) during atrial systole. The opposite happens during ventricular systole, which is indeed characterized by positive radial strains (corresponding to wall thickening) and negative circumferential strains (corresponding to a decreasing LV cavity).

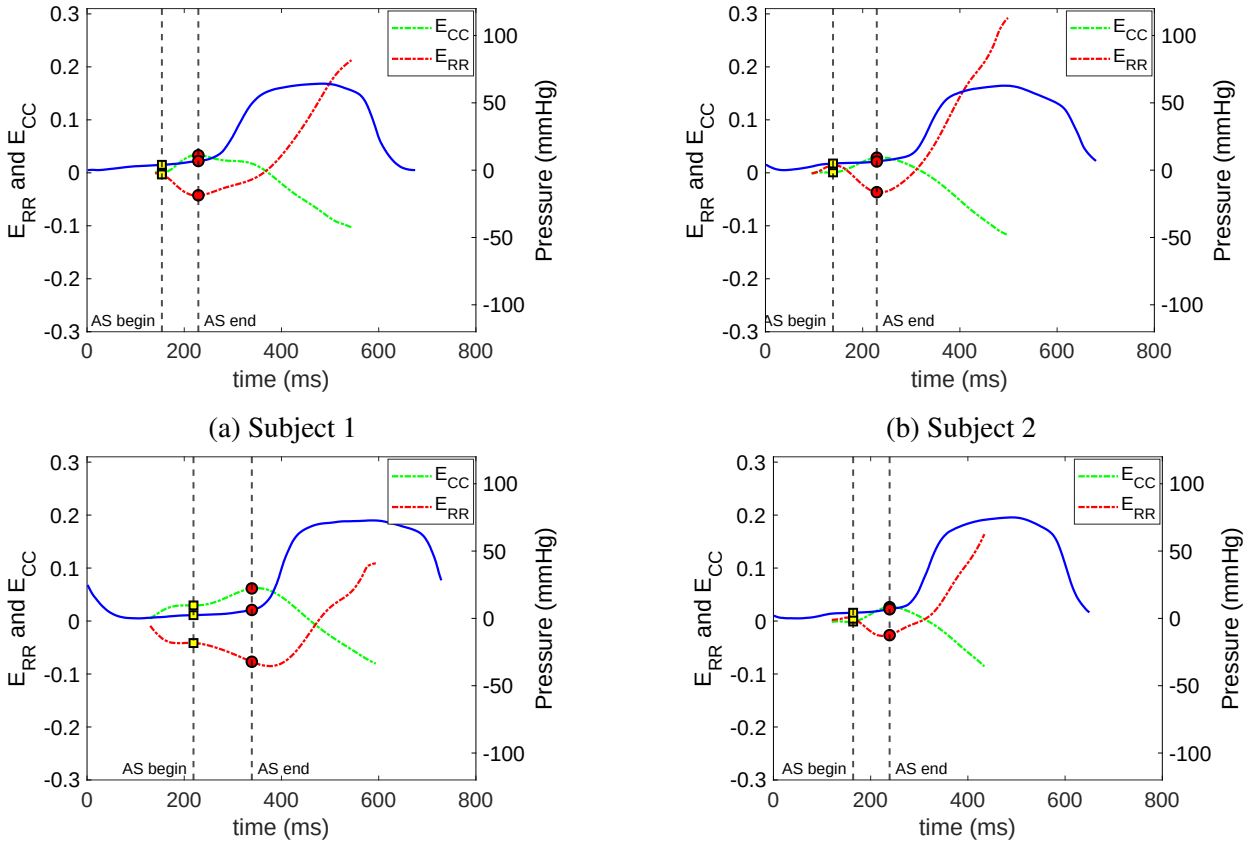

(a) Subject 1

(b) Subject 2

(c) Subject 3

(d) Subject 4

Figure 4.3: Intraventricular pressure overlaid to E_{RR} and E_{CC} quantified from 3 mid-ventricular short-axis slices for subjects 1 to 4 in the control group.

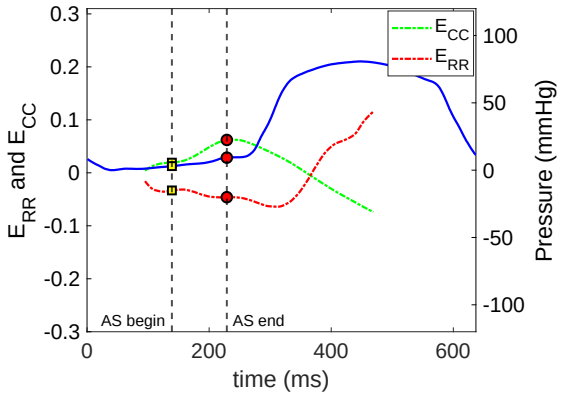

(a) Subject 5

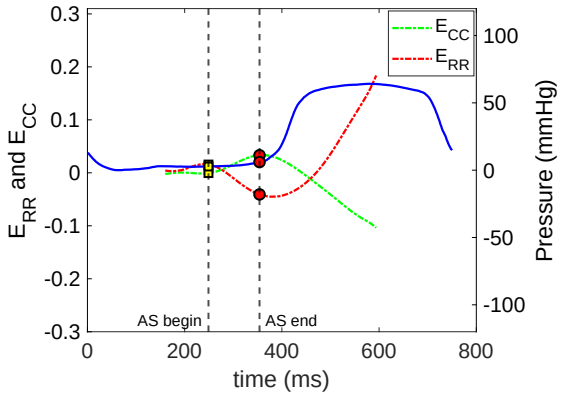

(b) Subject 6

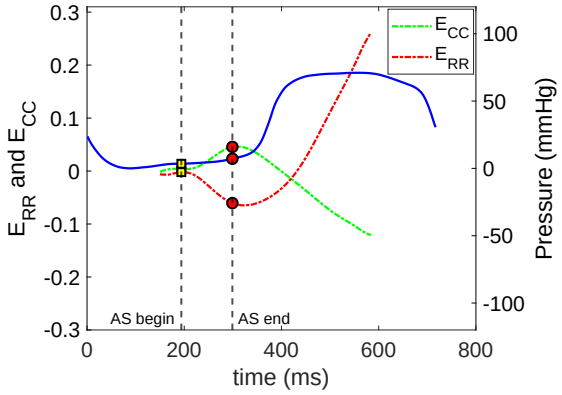

(c) Subject 7

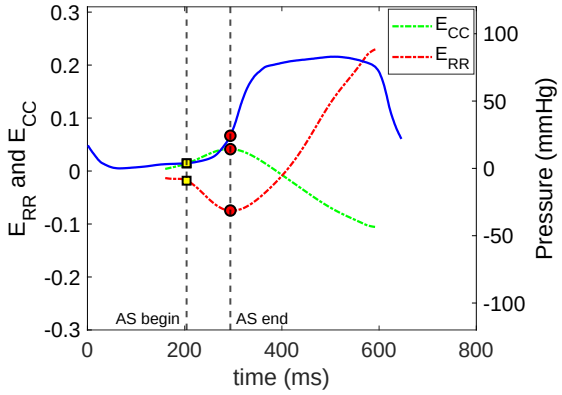

(d) Subject 8

Figure 4.4: Intraventricular pressure overlaid to E_{RR} and E_{CC} quantified from 3 mid-ventricular short-axis slices for subjects 5 to 8 in the control group.

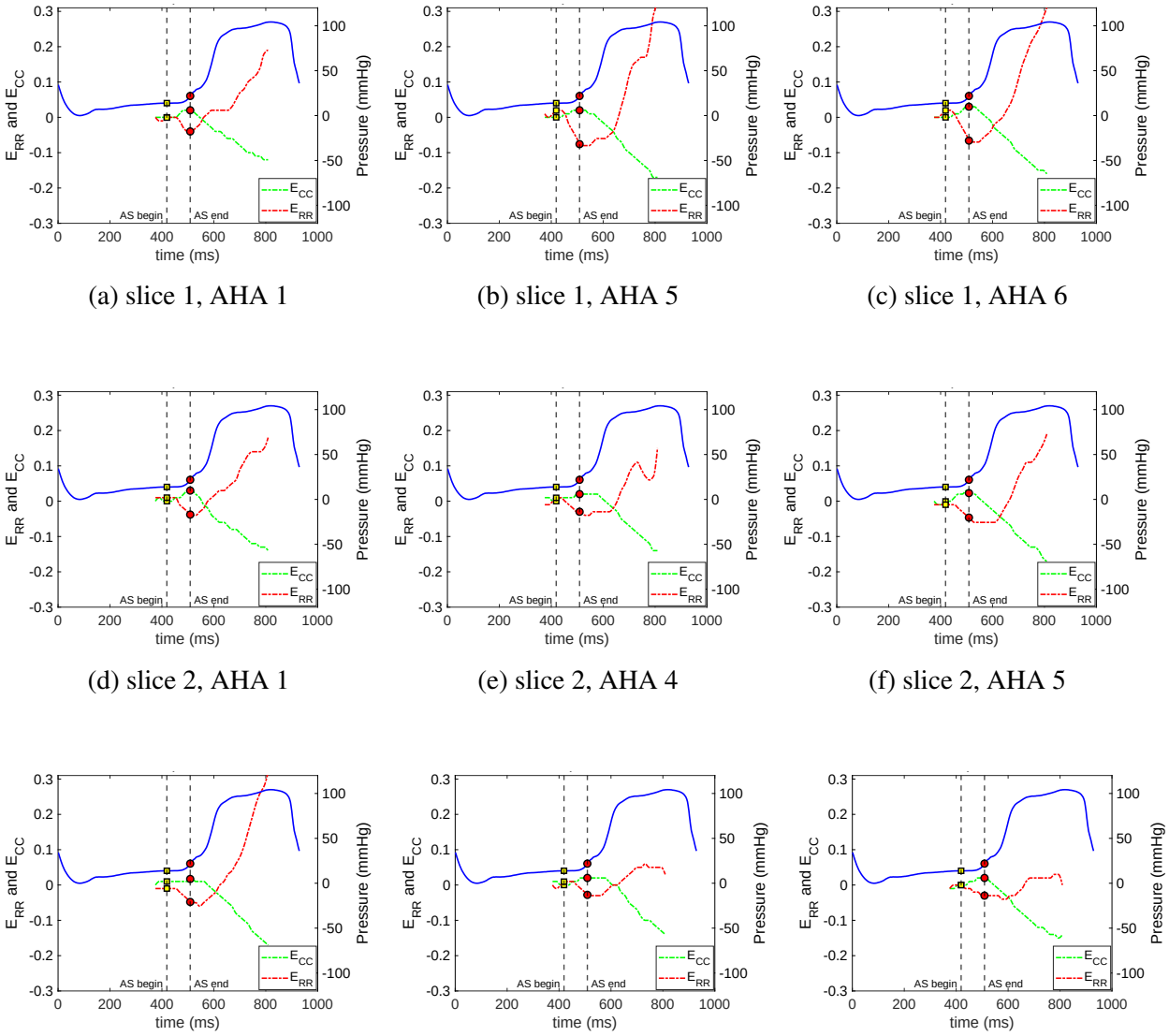

(a) slice 1, AHA 1 (b) slice 1, AHA 5 (c) slice 1, AHA 6

(d) slice 2, AHA 1 (e) slice 2, AHA 4 (f) slice 2, AHA 5

(g) slice 2, AHA 6 (h) slice 3, AHA 4 (i) slice 3, AHA 5

Figure 4.5: Intraventricular pressure overlaid with E_{RR} and E_{CC} quantified from mid-ventricular short axis slice 1 (AHA region 1 (a), AHA region 5 (b), and AHA region 6 (c)); slice 2 (AHA region 1 (d), AHA region 4 (e), AHA region 5 (f), and AHA region 6 (g)); slice 3 (AHA region 4 (h) and AHA region 5 (i)), for subject 1 in the MI group. The reported AHA regions correspond to regions where an infarcted area is present.

The physiological deformation occurring during atrial systole can also be observed from strain values computed in LA slices. In Figs. 4.6-4.7, we reported intraventricular pressure traces

registered in time with E_{RR} and E_{LL} quantified from LA slices acquired in 8 subjects in the control group. A positive E_{LL} corresponds to the lengthening or elongation of the left ventricle during atrial systole due to late filling. In Figs. 4.8 and 4.9, we reported intraventricular pressure traces synchronized with E_{LL} quantified from LA slices acquired in 2 subjects in the MI group. The reported AHA regions correspond to regions where an infarcted area is present.

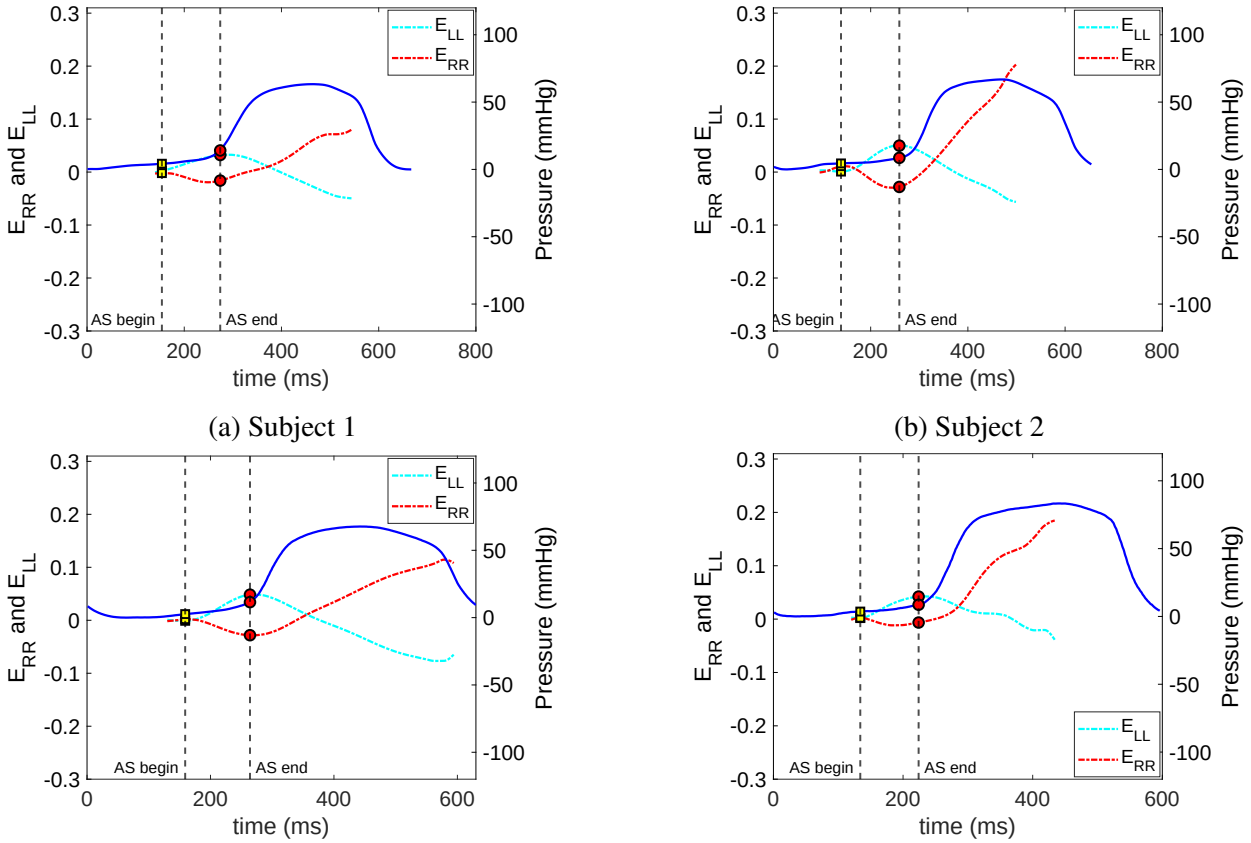

(a) Subject 1

(b) Subject 2

(c) Subject 3

(d) Subject 4

Figure 4.6: Intraventricular pressure overlaid to E_{LL} and E_{RR} quantified from long axis slices for subjects 1 to 4 in the control group.

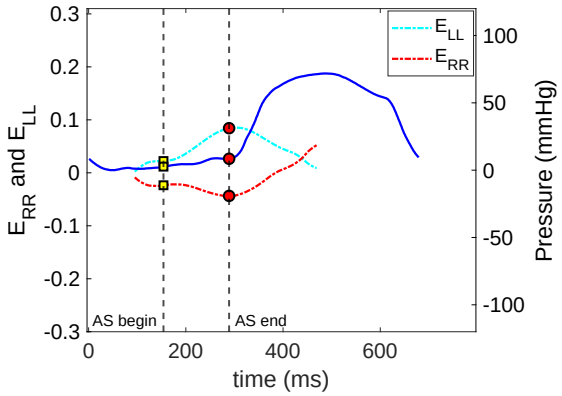

(a) Subject 5

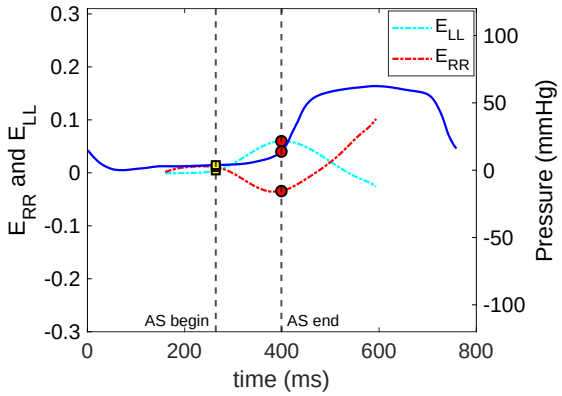

(b) Subject 6

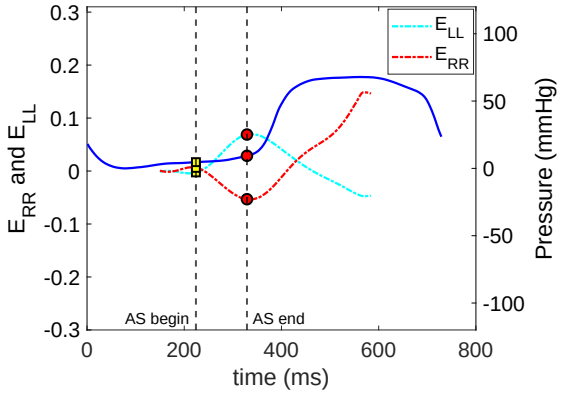

(c) Subject 7

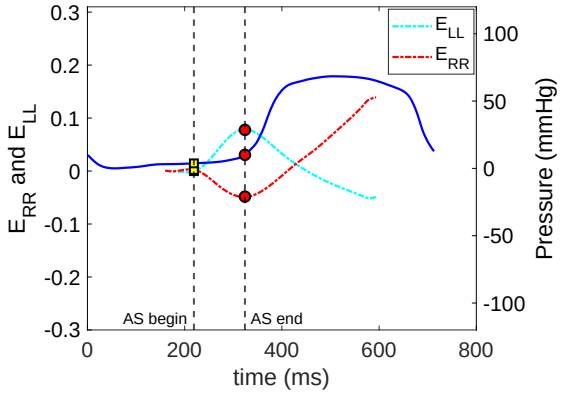

(d) Subject 8

Figure 4.7: Intraventricular pressure overlaid to E_{LL} and E_{RR} quantified from long axis slices for subjects 5 to 8 in the control group.

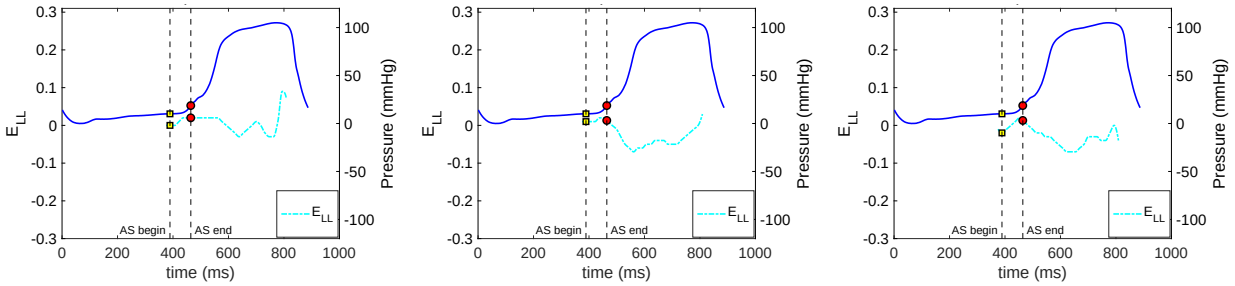

(a) slice 1, AHA region 3 (b) slice 2, AHA region 1 (c) slice 3, AHA region 5

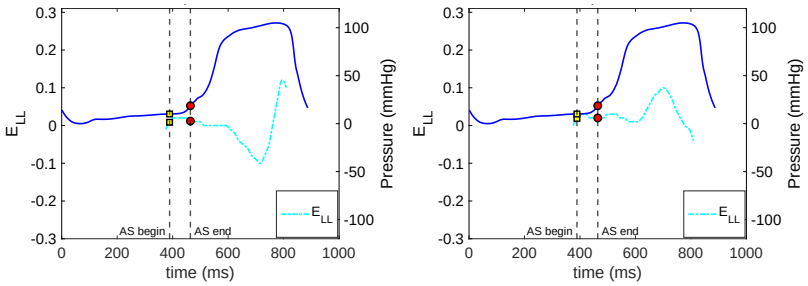

(d) slice 4, AHA region 5 (e) slice 5, AHA region 3

Figure 4.8: Intraventricular pressure overlaid to E_{LL} quantified from long axis slice 1 in AHA region 3 (a); slice 2 in AHA region 1 (b); slice 3 in AHA region 5 (c); slice 4 in AHA region 5 (d); and slice 5 in AHA region 3 (e), for subject 1 in the MI group. The reported AHA regions correspond to regions where an infarcted area is present.

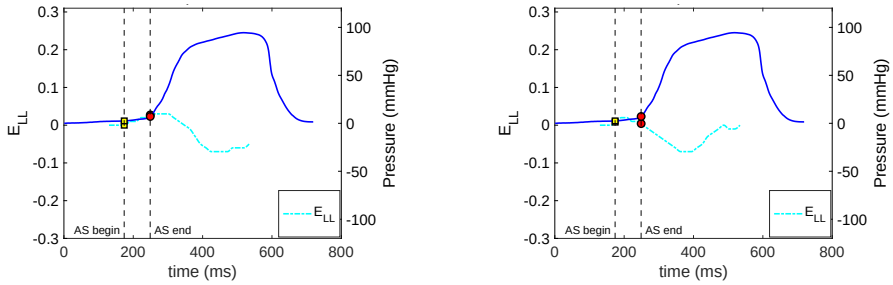

(a) slice 1, AHA 3 (b) slice 2, AHA 3

Figure 4.9: Intraventricular pressure overlaid to E_{LL} quantified from long axis slice 1 in AHA region 3 (a) and slice 2 AHA region 3 (b) for subject 2 in the MI group. The reported AHA regions correspond to regions where an infarcted area is present.

Peak LV strain and strain rate during atrial systole

We reported peak atrial systolic E_{CC} and E_{RR} quantified from 3 mid-ventricular SA slices and peak atrial systolic E_{LL} and E_{RR} quantified from LA slices for each subject in the control group (Table 4.1). The mean peak atrial systolic E_{CC} and E_{RR} (from 3 mid-ventricular SA) reported in the control group is 0.04 $\pm$ 0.01 and -0.05 $\pm$ 0.02, respectively. The mean peak atrial systolic E_{LL} and E_{RR} (from LA) reported in the control group is 0.06 $\pm$ 0.02 and -0.03 $\pm$ 0.01 respectively.

Table 4.1: Peak atrial systolic E_{CC} and E_{RR} quantified from 3 mid-ventricular SA slices and peak atrial systolic E_{LL} and E_{RR} quantified from LA slices for the control group

Subjects	**SA**		**LA**	
	peak $E_{\mathbf{CC}}$	peak $E_{\mathbf{RR}}$	peak $E_{\mathbf{LL}}$	peak $E_{\mathbf{RR}}$
S1	0.03	-0.04	0.03	-0.02
S2	0.03	-0.04	0.05	-0.03
S3	0.06	-0.08	0.05	-0.03
S4	0.03	-0.03	0.04	-0.01
S5	0.06	-0.05	0.09	-0.04
S6	0.03	-0.04	0.06	-0.04
S7	0.05	-0.06	0.07	-0.05
S8	0.04	-0.07	0.08	-0.05
Mean $\pm$ SD	0.04 $\pm$ 0.01	-0.05 $\pm$ 0.02	0.06 $\pm$ 0.02	-0.03 $\pm$ 0.01
Median [Q1,Q3]	0.04 [0.03,0.05]	-0.04 [-0.07,-0.04]	0.05 [0.05,0.07]	-0.03 [-0.04,-0.03]

Next, for the subject group MI, we reported peak E_{CC} and E_{RR} quantified from mid-ventricular SA slices (for 1 subject) and peak E_{LL} quantified from LA slices (for 2 subjects) during atrial systole (Table 4.2). The values are reported for AHA regions with an infarcted area. The mean peak atrial systolic E_{CC} and mean peak atrial systolic E_{RR} (from mid-ventricular SA) reported for 1 subject in the MI group is 0.02 $\pm$ 0.004 and -0.05 $\pm$ 0.01 respectively. The mean peak atrial systolic E_{LL} (from LA) reported for 2 subjects in the subject group MI is 0.02 $\pm$ 0.004.

Lastly, in Tables 4.3 and 4.4 we reported the peak atrial systolic strain rates as $\dot{E}_{CC}$, $\dot{E}_{RR}$, $\dot{E}_{LL}$ for subject groups control and MI. The mean peak atrial systolic $\dot{E}_{CC}$ and $\dot{E}_{RR}$ reported from SA slices are 0.36 $\pm$ 0.08 1/s and -0.46 $\pm$ 0.16 1/s, respectively in the control group. The mean peak

Table 4.2: Peak atrial systolic E_{CC} and E_{RR} quantified from mid-ventricular SA slices and peak atrial systolic E_{LL} quantified from LA slices for the MI group

Subjects	**SA**				**LA**		
	SA	**AHA segment**	peak E_{CC}	peak E_{RR}	**LA**	**AHA segment**	peak E_{LL}
S1	**SA1**	1	0.02	-0.04	**LA1**	3	0.02
		5	0.02	-0.08	**LA2**	1	0.02
		6	0.03	-0.07	**LA3**	5	0.02
	SA2	1	0.03	-0.04	**LA4**	5	0.02
		4	0.02	-0.03	**LA5**	3	0.03
		5	0.03	-0.05			
		6	0.02	-0.05			
	SA3	4	0.02	-0.03			
		5	0.02	-0.03			
S2					**LA1**	3	0.03
					LA2	3	0.02
Mean $\pm$ SD			0.02 ± 0.004	-0.05 ± 0.01			0.02 ± 0.005
Median [Q1,Q3]			0.02 [0.02,0.03]	-0.04 [-0.05,-0.03]			0.02 [0.02,0.03]

atrial systolic $\dot{E}_{LL}$ and $\dot{E}_{RR}$ reported from LA slices are 0.48 $\pm$ 0.16 1/s and -0.29 $\pm$ 0.17 1/s , respectively, in the control group. The mean peak atrial systolic $\dot{E}_{CC}$ and $\dot{E}_{RR}$ reported from SA slices are 0.26 $\pm$ 0.05 1/s and -0.51 $\pm$ 0.19 1/s, respectively, in the MI group (for 1 subject). The mean peak atrial systolic $\dot{E}_{LL}$ reported from LA slices is 0.30 $\pm$ 0.06 1/s in the MI group (for 2 subjects). The peak atrial systolic strain rates reported from different SA and LA slices correspond to the same slices and regions from which the mean peak atrial systolic E_{CC}, E_{RR}, and E_{LL} are reported previously (Table 4.2).

Discussion

The concurrent display of intraventricular pressure alongside synchronized longitudinal, circumferential, and radial strains (E_{LL}, E_{CC}, E_{RR} respectively) during atrial systole provides insights into the relation between intraventricular pressure changes and the corresponding LV kinematics. During atrial systole, longitudinal and circumferential strain are positive, indicating

Table 4.3: Peak E_{CC} and E_{RR} rates from mid-ventricular SA slices and peak E_{LL} and E_{RR} rates from LA slices for the control group.

Subjects	**SA**		**LA**	
	$\dot{E}_{CC}$ (s^{-1})	$\dot{E}_{RR}$ (s^{-1})	$\dot{E}_{LL}$ (s^{-1})	$\dot{E}_{RR}$ (s^{-1})
S1	0.45	-0.52	0.25	-0.12
S2	0.31	-0.57	0.41	-0.33
S3	0.27	-0.29	0.47	-0.29
S4	0.36	-0.41	0.45	-0.10
S5	0.48	-0.14	0.46	-0.15
S6	0.32	-0.54	0.41	-0.33
S7	0.40	-0.56	0.68	-0.56
S8	0.30	-0.63	0.74	-0.48
Mean $\pm$ SD	0.36 $\pm$ 0.08	-0.46 $\pm$ 0.16	0.48 $\pm$ 0.16	-0.29 $\pm$ 0.17
Median [Q1,Q3]	0.34 [0.31,0.41]	-0.53 [-0.56,-0.38]	0.45 [0.41,0.52]	-0.31 [-0.37,-0.14]

Table 4.4: Peak E_{CC} and E_{RR} rates from mid-ventricular SA slices and peak E_{LL} rate from LA slices for the MI group.

Subjects	**SA**				**LA**		
	SA	**AHA segment**	$\dot{E}_{CC}$ (s^{-1})	$\dot{E}_{RR}$ (s^{-1})	**LA**	**AHA segment**	$\dot{E}_{LL}$ (s^{-1})
S1	**SA1**	1	0.22	-0.4	**LA1**	3	0.27
		5	0.22	-0.89	**LA2**	1	0.27
		6	0.33	-0.77	**LA3**	5	0.27
	SA2	1	0.33	-0.40	**LA4**	5	0.27
		4	0.22	-0.33	**LA5**	3	0.40
		5	0.33	-0.56			
		6	0.22	-0.56			
	SA3	4	0.22	-0.33			
		5	0.22	-0.33			
S2					**LA1**	3	0.40
					LA2	3	0.27
Mean $\pm$ SD			0.26 $\pm$ 0.05	-0.51 $\pm$ 0.19			0.30 $\pm$ 0.06
Median [Q1,Q3]			0.22 [0.22,0.33]	-0.40 [-0.56,-0.33]			0.27 [0.27,0.33]

left ventricular 'elongation' along the long axis and 'expansion' in the circumferential direction. Concurrently, radial strains during atrial systole are negative, indicating wall thinning. These strain values correspond to the late ventricular filling phase during atrial systole.

During atrial systole, rapid changes in ventricular geometry occur within a short duration, necessitating imaging techniques that may accurately capture LV kinematics during this short phase of the cardiac cycle. In addition, ventricular strains during atrial systole are notably smaller

compared to ventricular strains during ventricular systole, amplifying the impact of experimental noise and post-processing techniques on strain values. Furthermore, during atrial systole, the LV undergoes passive deformation due to the pressure wave generated by atrial contraction. The resulting LV deformation is non-uniform adding to the complexity of strain assessment. In this work, we have used the established DENSE analysis toolbox [130] (available at https://github.com/denseanalysis/denseanalysis) GitHub Repository to overcome some of these challenges, but further work is necessary.

Although, due in part to the challenges listed above, direct investigations of LV strains and kinematics during atrial systole are limited, some data from 2D echocardiography provide comparative insights into strain rates across both healthy and diseased cohorts. One of these studies concluded that peak atrial systolic LV circumferential strain rate may be an early predictor of diastolic dysfunction in patients with hypertension (HT) [98]. Another study reported preserved systolic function in left ventricular hypertrophy (LVH) patients with a compromised regional diastolic function (reduced early diastolic strain rate in LV) [37]. These studies emphasize the significance of assessing LV strain during diastole or atrial systole. Our study represents one of the few analyses of ventricular strains specifically during atrial systole. The capacity to accurately quantify and characterize strains during the myocardium's passive response may hold significant value in assessing impaired passive myocardial response in various cardiac pathologies, such as HFpEF and DD. Therefore, the novelty of this study lies in its exploration of ventricular strains during atrial systole, shedding light on an aspect of cardiac kinematics that remains relatively unexplored but may have significant clinical relevance.

By performing the Kruskal-Wallis test on peak atrial systolic E_{CC}, we found significant differences between the control and MI groups (p=0.002). We performed the same test on peak atrial systolic $\dot{E}_{\mathrm{CC}}$ and again found a significant difference between the control and MI groups (p= 0.02). Next, we performed the Kruskal-Wallis test on peak atrial systolic E_{LL} and peak atrial systolic $\dot{E}_{\mathrm{LL}}$

quantified from the LA slices. We found significant differences in both cases between the control and MI groups (p = 0.001 and p = 0.01 respectively). However, when we performed the same test on peak atrial systolic E_{RR} and peak atrial systolic $\dot{E}_{\mathrm{RR}}$ between the two groups, there was no statistically significant difference (p = 0.52 and p=0.92 respectively, control vs MI). This may be due to the known larger uncertainty in computing radial strains that may obscure differences between control and MI subjects. These values are being reported in Table 4.5. Our result agrees with other studies that reported reduced ventricular strain during atrial systole between healthy individuals and MI patients [137]. Several other studies also reported no significant differences in ventricular strain and strain rates during atrial systole [111, 155]. These findings suggest that while MI can lead to substantial alterations in ventricular function, these changes may not always be detectable or distinguishable from normal variations in healthy individuals. The aforementioned challenges in computing LV strains during atrial systole combined with factors such as the extent and location of myocardial damage [56], the presence of collateral circulation, and individual patient characteristics may contribute to the variability in strain measurements observed across studies. Several studies [39, 111, 155] also reported significant alterations in early diastolic strain and strain rates in MI patients.

Table 4.5: p- value between two groups

Control vs MI	p-value
peak E_{CC} (SA)	0.002
peak E_{RR} (SA)	0.52
peak E_{LL} (LA)	0.001
peak $\dot{E}_{\mathrm{CC}}$(SA)	0.02
peak $\dot{E}_{\mathrm{RR}}$ (SA)	0.92
peak $\dot{E}_{\mathrm{LL}}$ (LA)	0.01

Variability in infarct size and location within the MI group is mainly due to the chosen artery branch for infarct induction (either the left anterior descending – LAD – or left circumflex – LCx

– artery). This selection of the artery for infarct induction may lead to variability in the affected regions as well. Healthy myocardium demonstrates characteristic strain patterns associated with optimal function. In contrast, strain values in infarcted tissue tend to be notably lower than those in healthy tissue during atrial systole, indicating abnormal myocardial function attributable to scar formation following MI. While quantifying strain and strain rates, thus considering the location of infarcted regions separating healthy and infarcted myocardium is very important to capture the strain accurately. In this study, we focused on the American Heart Association (AHA) segment-wise quantification of ventricular strain during atrial systole with specific emphasis on the infarct region in the MI group.

Study limitations and future work

Here we subdivided the myocardium using the AHA regions and, in the MI group, we reported LV strains during atrial systole only using the AHA regions that contain infarcted myocardium. A more precise strategy would involve delineating exactly the infarcted myocardium without relying on the AHA subdivision as, for example, an infarcted segment may not occupy the full AHA region in which it is contained. If this is the case, the reported strain per AHA region includes both strains in infarcted and remote/border zone myocardium, partially confounding the results.

Given the complications related to identifying the infarcted myocardium, there is a risk of combining healthy and infarcted myocardium during this procedure. Thus we proceeded with caution to quantify strain only from 2 of the subjects in the MI group. In this process, we chose to use the subjects with two of the largest myocardial infarct volumes (in %) (see detailed infarct volume identification procedure in section 'Quantification of *in vivo* LV cardiac indices', chapter 3). The infarct volume (in %) quantification was done using T1 weighted images in open-source software '3D Slicer' (http://www.slicer.org) [43].

Additionally, in this study, we have used a small cohort size of N=10 combining both groups. A larger cohort size will improve and strengthen the reported results and the outcome of this study.

CHAPTER 5: PASSIVE MYOCARDIUM MATERIAL LAWS AND MATERIAL PROPERTIES

In this chapter, we work towards our third and final objective which is the study of a material law and material properties to describe the response of the passive myocardium. This task is achieved by optimizing the equilibrium between external (i.e., LV intraventricular pressure, presented previously in Chapter 3) and internal forces (due to the myocardium deformation, presented previously in Chapter 4).

Experimental data

For this study's final objective, only the control group was utilized. Figure 5.1 provides a visual representation of the process by which the dataset used in this study was acquired. In total, nine (N=8) subjects were included in the control group. The research conducted in this chapter primarily employed cardiac DENSE MRI alongside pressure data acquired simultaneously through *in vivo* cardiac catheterization.

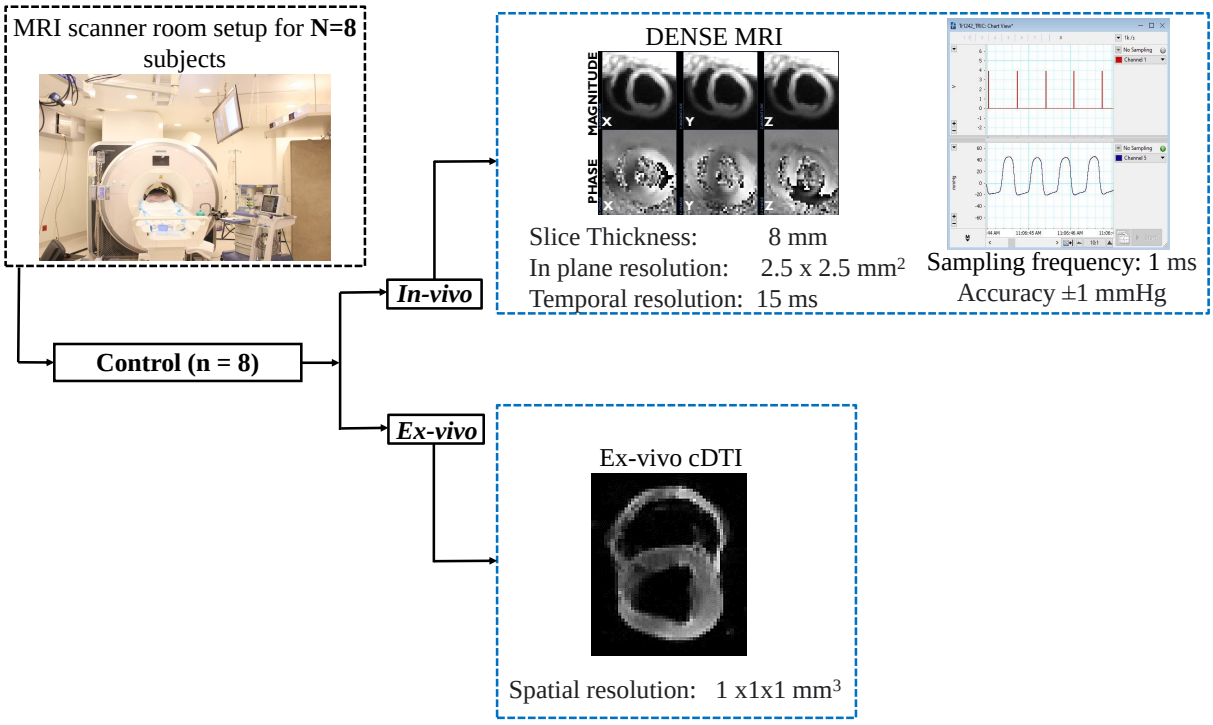

Figure 5.1: Flow chart representing the acquisition of the data used for computing material laws and properties describing the passive myocardium

Methodology and Data Analysis

The subsequent sections detail the methodology employed for computing the material laws and parameters describing the passive myocardium response. This includes:

1. The minimization of the difference between external or applied forces (intraventricular pressure) and internal forces (due to cardiac deformation);
2. The description of the material law considered to describe the passive myocardium response;
3. The definition of LV 3D microstructure-based mid-ventricular models.

External and internal forces

Pressure measurements obtained, for example, via catheterization can be used to define the external forces acting on the LV endocardial surface. In chapter 3, a detailed process of how the intraventricular pressure is extracted and processed is elaborated. The developed custom MATLAB code [91] extracted pressure data from LabChart files, synchronizing it with the cardiac cine DENSE MRI data acquired for each subject. This ensured alignment between pressure measurements, cardiac deformation mapping, and the constructed LV 3D models (please see details in chapter 3). After the registration, the intraventricular pressure values as well as cardiac deformation data were extracted from the beginning of the atrial systole phase to the end of the atrial systole phase for each subject.

To minimize the difference between external and internal forces, we follow the work of [115] which allows us to compute material parameters and characterize the passive myocardium's response. Several other works in the literature have previously proposed and used the equilibrium gap method that is based on minimizing the norm of the residual vector (see, e.g., [28]). In biomechanics, various approaches aim to identify material properties by minimizing the difference between experimental $\mathbf{u}_{\text{exp}}$ and computed $\mathbf{u}_{\text{num}}$ displacement fields under applied forces and boundary conditions [146, 80, 77]. Computed displacements $\mathbf{u}_{\text{num}}$ are usually obtained by solving the equilibrium equations, often using the Finite Element Method. Material properties are iteratively adjusted to minimize the discrepancy between experimental and computed displacements. However, these standard methods may not yield unique material properties and may not offer insight into the formulation of the material law to be considered. To address this, Perotti et al. proposed a reversed approach using experimental displacements to compute internal forces and uniquely identify the material properties [115] by enforcing, as closely as possible, equilibrium between internal $\mathbf{f}_{\text{int}}$ and external forces $\mathbf{f}_{\text{ext}}$. Imperfect equilibrium arises from errors

in displacement measurements, pressure, and material model. Thus, material properties $\boldsymbol{\alpha}$ are identified by minimizing the error between f_{int} and f_{ext} as:

$$(\boldsymbol{\alpha}) = \text{argmin}_{\boldsymbol{\alpha}} g(\boldsymbol{\alpha}) \,, \tag{5.1}$$

where

$$g(\boldsymbol{\alpha}) = \mathbf{R}(\boldsymbol{\alpha})^T \mathbf{R}(\boldsymbol{\alpha}) \,, \tag{5.2}$$

and $\mathbf{R}(\boldsymbol{\alpha})$ is the residual vector:

$$\mathbf{R}(\boldsymbol{\alpha}) = \mathrm{f}_{\text{int}} - \mathrm{f}_{\text{ext}} \,. \tag{5.3}$$

If the material energy density W is chosen so that is linear in the material properties $\boldsymbol{\alpha}$, then $g(\boldsymbol{\alpha})$ is quadratic in $\boldsymbol{\alpha}$ and admits a unique solution for $\boldsymbol{\alpha}$ as far as the Hessian $\mathbf{H}_g$ is positive definite.

If $\mathbf{H}_g$ is semi-positive definite, the available experimental data is insufficient to characterize the material properties in W. Tailoring W to problem complexity and data quantity ensures a strictly positive definite $\mathbf{H}_g$, ensuring uniqueness of $\boldsymbol{\alpha}$.

Numerically g is minimized using the Newton-Raphson method.

The material law for the passive myocardium

$W(\boldsymbol{\alpha}, \mathbf{C}(\mathbf{u}))$ can be expressed as a linear combination of terms $\Phi_i(\mathbf{C}(\mathbf{u}))$, each representing a different component of the isotropic and anisotropic material response. The coefficients of this linear interpolation are the material properties $\boldsymbol{\alpha}$ so that:

$$W(\boldsymbol{\alpha}, \mathbf{C}(\mathbf{u})) = \sum_{i=1}^{N} \alpha_i \Phi_i(\mathbf{C}(\mathbf{u})) \tag{5.4}$$

where $\Phi_i(\mathbf{C}(\mathbf{u}))$ are polyconvex functions of the deformation invariants, N is the number of terms used to capture the material behavior, $\mathbf{C}$ is the right Cauchy-Green deformation tensor, and $\mathbf{u}$ is the displacement field. All material properties α_i need to be greater than zero.

Principles for constructing polyconvex energy functions that meet the stress-free reference configuration condition have been outlined in [8] and a subset of these functions is selected by Perotti et al. [115], aiming to capture the experimental response of the passive myocardium effectively. Based on their previous work, we use the following expression for Φ_1 and Φ_2:

$$\Phi_1 = \left(\frac{I_1}{I_3^{\frac{1}{3}}} - 3 \right)^{a_1} \tag{5.5}$$

$$\Phi_2 = \langle I_4 - 1 \rangle^{a_2} \tag{5.6}$$

where $a_1 = 2.60$, $a_2 = 2.82$, $I_1 = \text{tr}(\mathbf{C})$, $I_3 = \det(\mathbf{C})$, and $I_4 = \text{tr}\left(\mathbf{C}(\mathbf{A} \otimes \mathbf{A})\right)$, with $\mathbf{A}$ representing the material direction of anisotropy, i.e., the local myofiber direction.

Based on the previous discussion, the strain energy function W is

$$W = \alpha_1 \left(\frac{I_1}{I_3^{\frac{1}{3}}} - 3 \right)^{2.60} + \alpha_2 \langle I_4 - 1 \rangle^{2.82} \tag{5.7}$$

where α_1 and α_2 represent the isotropic and anisotropic material properties, respectively.

LV mid-ventricular models construction

From the acquired *in vivo* cine DENSE MRI and *ex vivo* cDTI data, a microstructurally and anatomically accurate finite element model was built for this study. For each subject, 3 mid-ventricular short-axis slices were chosen to build the LV 3D models. As described previously in the section 'Segmentation and image analysis of cardiac DENSE MRI data for the assessment of cardiac strain and deformations during atrial systole' (chapter 4), cardiac cine DENSE MRI data was segmented at the beginning of atrial systole, which is considered as the reference configuration. A dedicated MATLAB code [91] was built and used to further process the data. LV epicardial and endocardial surfaces were extracted from the cardiac cine DENSE MRI segmentations. Subsequently, these contours were meshed utilizing 1848 nodes and 1188 linear hexahedral elements. For each mesh per subject, three elements were used across the myocardium wall, with an additional three elements longitudinally in between the DENSE slices, resulting in a total of six elements in the longitudinal direction. Next, the microstructural data was extracted from the *ex vivo* cDTI data for each subject to incorporate in the LV 3D mid-ventricular models. During the data acquisition process, *ex vivo* cDTI data was acquired by fixing the LV geometry close to the beginning of atrial systole using a 3D printed mold [29]. *Ex vivo* cDTI slices, each 1 mm apart, were manually identified by aligning the longitudinal position of the DENSE MRI data with the LV acquired using cDTI. The number of the *ex vivo* slices varied between 16 and 18. Subsequently, the *ex vivo* cDTI slices were registered with the DENSE-based mesh. During the registration process, all the cDTI images were rigidly translated and rotated to match the

DENSE-based LV mesh using the right ventricular insertion points in both the DENSE and cDTI images. Next, using this rigid transformation, the diffusion tensors were rotated. While the rigid registration accurately positioned and oriented the cDTI images, the LV shape in the *ex vivo* cDTI data had minor discrepancies compared to the mesh built with the LV model. Thus, a non-rigid (NR) registration was needed to ensure the overlap between the DENSE-based models and the cDTI data. LV short-axis contours were first segmented from the *ex vivo* cDTI data, followed by the creation of a mask from the segmented contours. Similarly, binary masks were generated from the DENSE contours at the beginning of atrial systole. A non-rigid registration (NR) was then performed between the DENSE LV mask and the cDTI LV mask employing a b-spline registration algorithm [120]. The NR registration was employed to deform the finite element quadrature points (QPs) to the spatial domain of the *ex vivo* cDTI data. The diffusion tensors were reconstructed utilizing a custom MATLAB framework (available at https://github.com/KMoulin/DiffusionRecon) and were then interpolated to each mapped QP within the FE mesh using linear invariant interpolation [54]. Myofiber orientations were determined at each QP by identifying the primary eigenvectors of the interpolated diffusion tensor corresponding to that point.

Results

In this section, we discuss the constructed LV mid-ventricular models, the validation of the proposed pipeline to compute the material properties, and the calibration of the material law to model the passive myocardium response.

LV mid-ventricular models and intraventricular pressure load during atrial systole

Intraventricular pressure was continuously recorded during the MRI acquisition procedure and, as described in section 'External and internal forces' (chapter 5) and chapter 4, it was synchronized with the cardiac cine DENSE MRI data. After synchronization, each subject's total deformation (from the beginning to the end of atrial systole) was extracted from 3 mid-ventricular short-axis slices along with the external change in pressure ΔP (from the beginning to the end of atrial systole) that caused that deformation. The displacements were then interpolated to get displacements at the finite element mesh nodal points. Fig. 5.2 represents synchronized intraventricular pressure with cardiac deformation mapping for 2 subjects. For this study, the

reference configuration is the beginning of atrial systole.

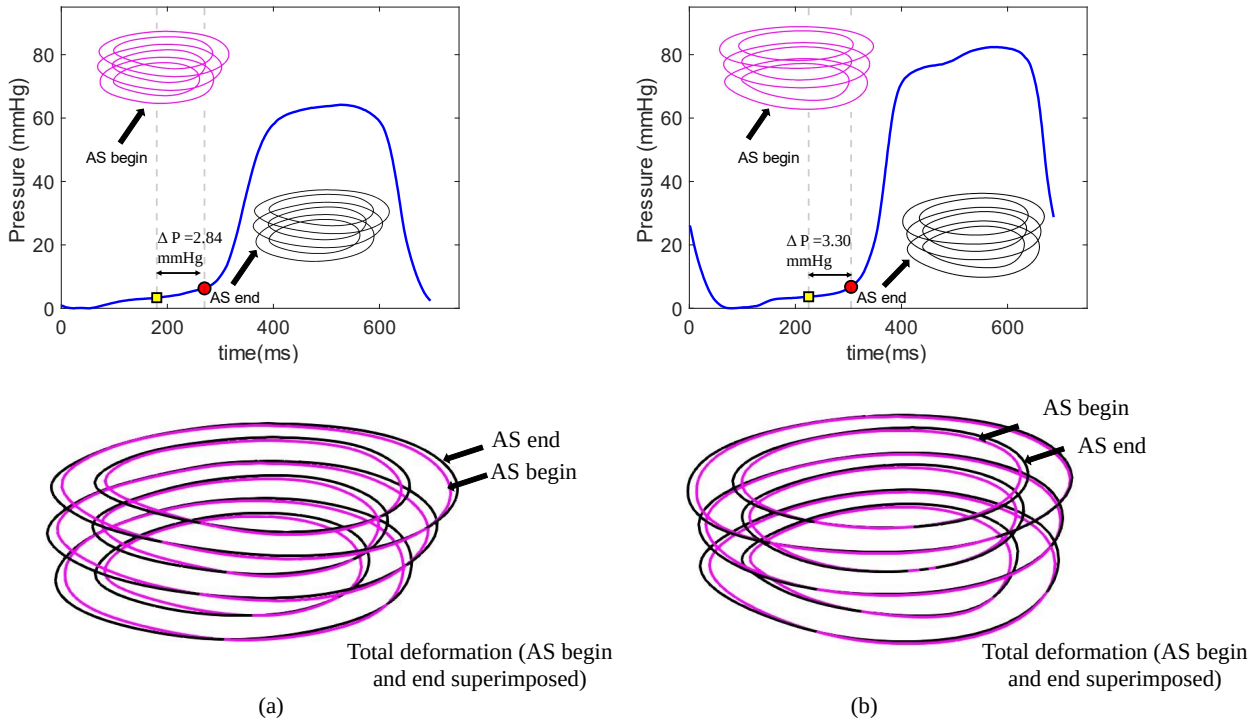

Figure 5.2: Synchronized intraventricular pressure with cardiac deformation mapping for subject 1 (a) and subject 6 (b). The epicardial and endocardial contours were extracted separately and then superimposed at the beginning and end of atrial systole to display the total deformation during atrial systole due to the applied pressure ΔP.

In Table 5.1, ΔP (pressure difference between the beginning and end of atrial systole) is reported for all the subjects in kPa.

The volumes enclosed by the epicardial and endocardial surfaces extracted from the DENSE data for each subject were meshed with 1848 nodes and 1188 linear hexahedral elements, with 3 elements across the myocardium wall and 3 elements longitudinally between DENSE slices (details in the section 'LV mid-ventricular models construction', chapter. 5). Subsequently, 8

Table 5.1: ΔP for 8 subjects in the Control group

Subjects	ΔP (kPa)
S1	0.38
S2	0.20
S3	0.52
S4	0.35
S5	0.84
S6	0.44
S7	0.49
S8	2.72

models were built as shown in Fig. 5.3 (S1 through S8) at the beginning of atrial systole (reference configuration).

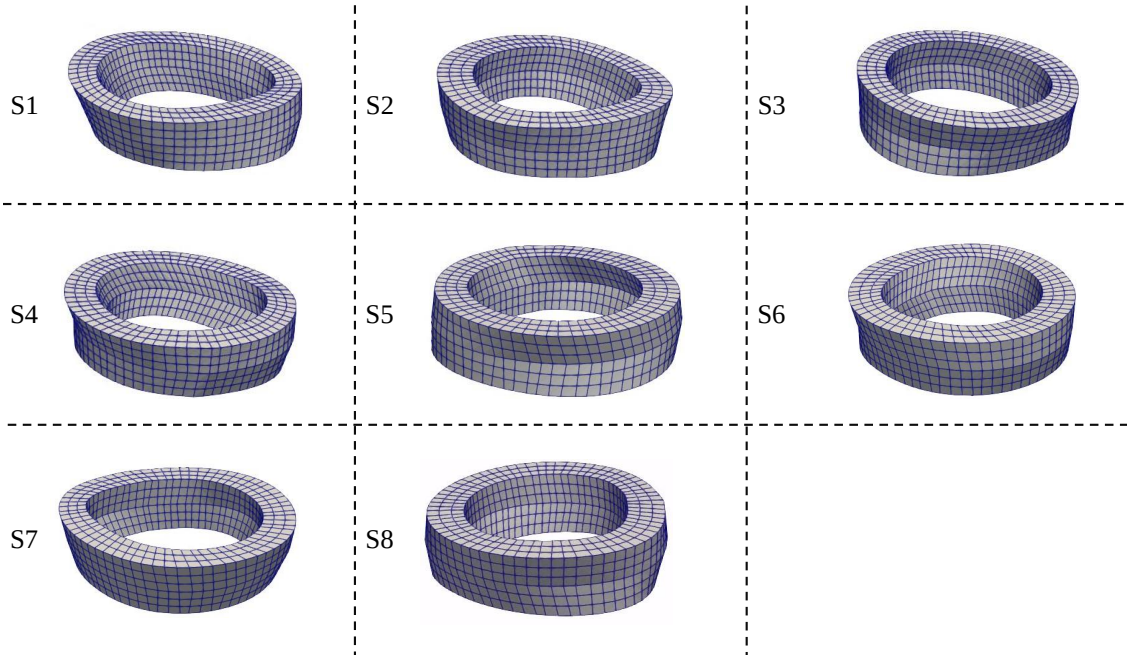

Figure 5.3: Subject-specific mesh built for N= 8 subjects from S1 through S8 at the beginning of atrial systole, which is the chosen reference configuration.

Next, microstructural data from ex-vivo cDTI scans were incorporated into the DENSE-based models following the method described in the section 'LV mid-ventricular models construction' (chapter. 5). The process is shown for 2 subjects in Fig. 5.4. The figure shows primary eigenvectors of the reconstructed diffusion tensor plotted for one short-axis slice. The fiber angle ranges from positive at the endocardium, passing through 0° close to the mid-wall, to negative at the epicardium. Finite element models built (reference configuration) from 3 midventricular short-axis slices (DENSE) and preferential aggregate cardiomyocyte orientation at each quadrature point in the finite element model (superimposed FEM model and microstructure data) is shown as well. In Fig. 5.5, FE models built (reference configuration) for all N=8 subjects are shown with the preferential aggregate cardiomyocyte orientation (superimposed FEM model and microstructure data).

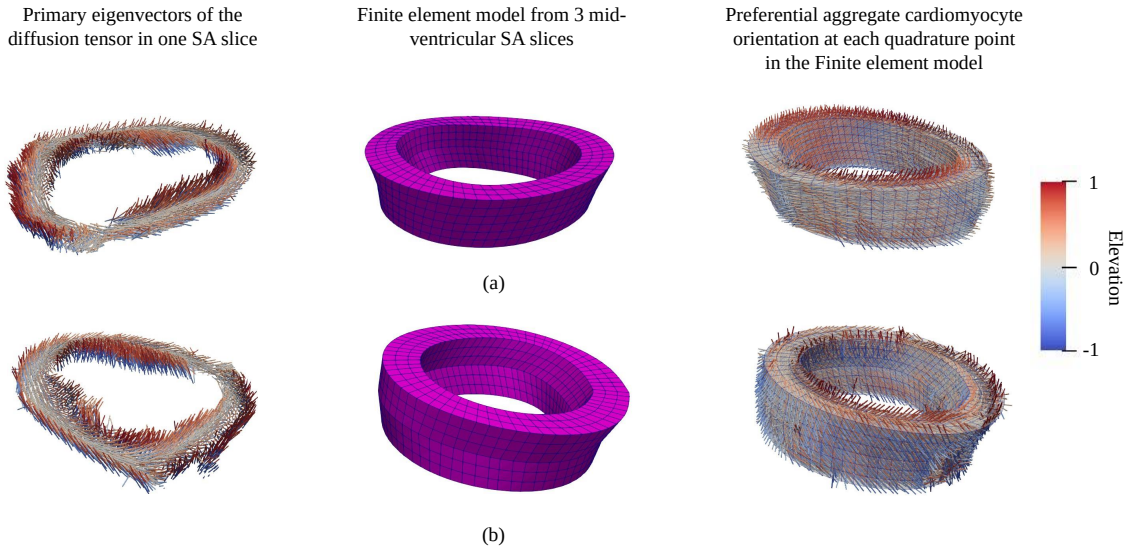

Figure 5.4: Subject-specific FE model for subject 1 (a) and subject 6 (b) showing primary eigenvectors of the diffusion tensor in 1 short-axis slice, FE model (reference configuration) based on 3 midventricular short-axis DENSE slices, and preferential aggregate cardiomyocyte orientation at each quadrature point in the FE model (superimposed FE model and microstructure data).

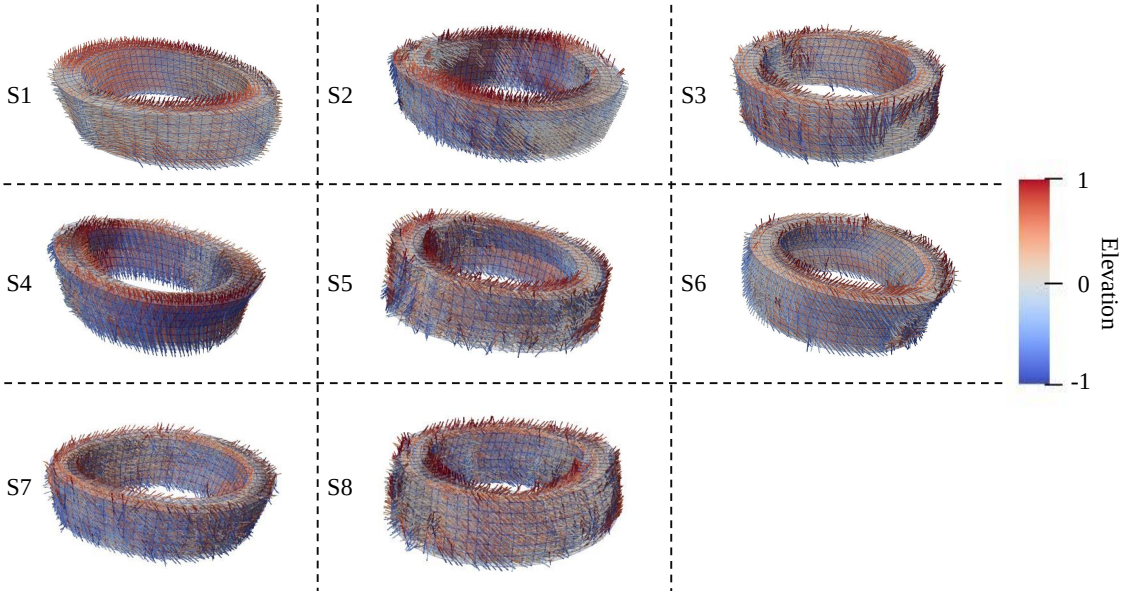

Figure 5.5: Subject-specific FE models and preferential aggregate cardiomyocyte orientation at each quadrature point in the FEM models for all subjects.

Validation of the proposed pipeline

A MATLAB algorithm was built to compute the material parameters by minimizing the difference between external and internal forces using the mid-ventricular finite element models constructed and discussed in the previous section.

Before applying this methodology to the swine data set, the proposed pipeline was validated by applying it to compute the material properties in a known boundary value problem. First, one of the swine mid-ventricular models was imported in ABAQUS [32]. A simple ABAQUS Neo-Hookean material model was chosen to set up the boundary value problem. The Neo-Hookean material model is a hyperelastic material model commonly used in finite element analysis to describe the mechanical behavior of elastic materials undergoing large deformations. The Neo-Hookean material model is suitable for isotropic, nearly incompressible materials such

as rubber and soft tissues. It provides a relatively simple representation of the material behavior according to the following material energy density:

$$W = C_{10}\left(\bar{I}_1 - 3\right) + \frac{1}{D_1}\left(J-1\right)^2 \tag{5.8}$$

where, $C_{10} = \frac{\mu}{2}$, μ being the shear modulus; $D_1 = \frac{2}{\kappa}$, κ being the bulk modulus; $\bar{I}_1 = J^{(-2/3)}tr(\mathbf{C})$, $\mathbf{C}$ being the right Cauchy-Green deformation tensor; and $J = \det(\mathbf{F})$, $\mathbf{F}$ being the deformation gradient tensor.

$C_{10} = 1000$ Pa and $D_1 = 0.0006$ 1/Pa were used in equation 5.8 during this test. For the boundary conditions of the FEM problem, all the nodes on the bottom surface were fixed in the Z direction. Along with that, a line of nodes parallel to the X axis was fixed in the Y direction, and a line of nodes parallel to the Y axis was fixed in the X direction. The boundary conditions were chosen to prevent any rigid body motion, without imposing further constraints on the motion of the LV due to intraventricular pressure. Additionally, a pressure of 100 Pa was applied to the endocardial surface. All the elements were 8-node linear hexahedral elements.

Figure 5.6 shows the boundary conditions that were used to set up the finite element boundary value problem in ABAQUS. Figure 5.6(a) shows the pressure applied perpendicularly to the endocardial surface (100 Pa). Figure 5.6(b-d) shows the other 3 boundary conditions as previously mentioned. Fig 5.7 shows the deformation due to the externally applied force (applied pressure perpendicular

to the endocardial surface) and applied boundary conditions.

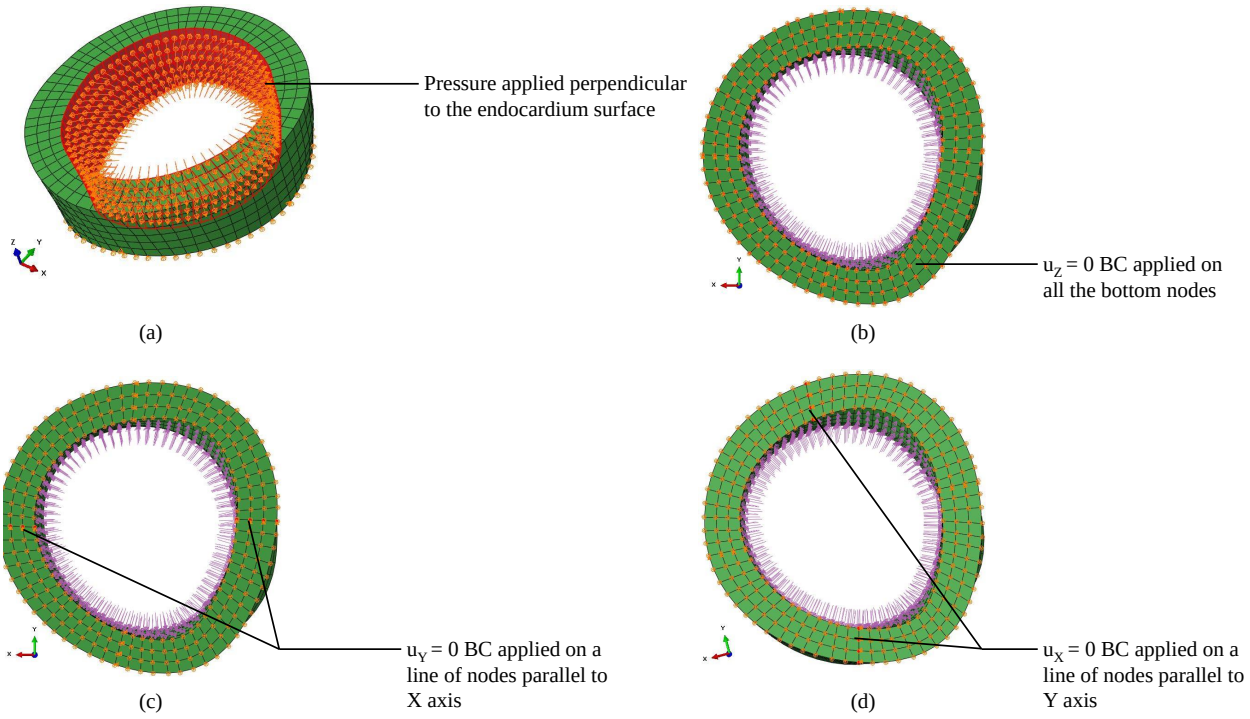

Figure 5.6: FE boundary value problem setup in ABAQUS showing: Pressure applied perpendicular to the endocardial surface (a); $u_Z = 0$ boundary condition applied on all the bottom nodes (b); $u_Y = 0$ boundary condition applied on a line of nodes (close to) parallel to the X-axis (c); $u_X = 0$ boundary condition applied on a line of nodes (close to) parallel to the Y-axis (d).

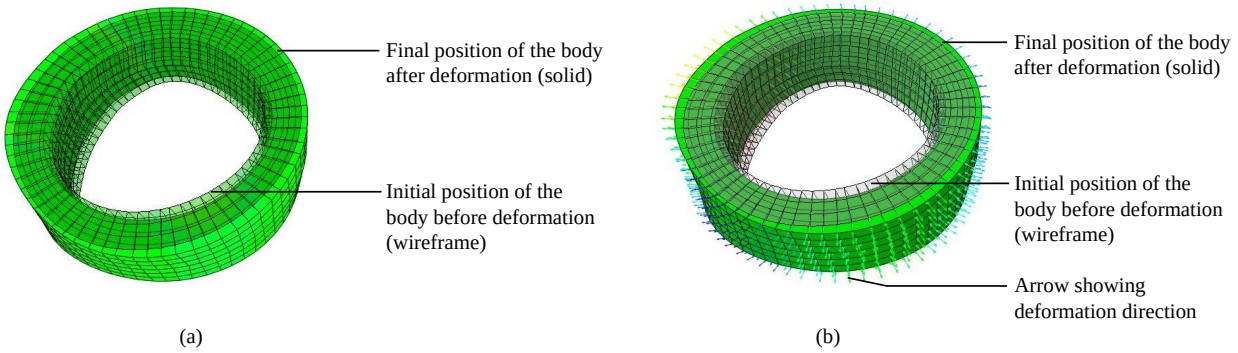

Figure 5.7: Total deformation due to the applied external force (pressure perpendicular to the endocardial surface) with initial (wireframe) and final (solid) configurations (a). Total deformation with arrows pointing in the deformation direction (b).

After running and completing the simulation in ABAQUS, the nodal displacements were extracted from the ABAQUS results. These nodal displacements together with the applied endocardial pressure were provided as input to the algorithm implemented in MATLAB for the unique identification of the material parameters. This procedure mimics the pipeline that will be followed using the experimental data and recovering the material properties used in the forward ABAQUS simulation will verify the implementation of the used scheme. As reported in Table 5.2, the implemented methodology in the MATLAB algorithm was successful in recovering both the Neo-Hookean material parameters C_{10} and D_1 that were used as input to calculate the obtained displacement field in ABAQUS.

Table 5.2: Normalized percent differences Δ in material parameters identified using the proposed pipeline versus the exact values used in the ABAQUS simulations. The small differences in identified versus original parameters confirm the verification of the proposed pipeline.

ΔC_{10} [%]	ΔD_1 [%]
0	0.03

The implemented algorithm in MATLAB was also tested using the same setup but with applied pressure subdivided into multiple steps. In this case, multiple pressure values and the corresponding deformation field were provided as input to the algorithm. This setup is meant to simulate the case (closer to the experimental data) where deformation and pressure values are available at multiple time frames, e.g., during atrial systole, and not only at the final cardiac phase. Previously, for the single step, the applied pressure was 100 Pa. For the multi-step process, first, we perform the test by applying pressure as 25 Pa, 50 Pa, 75 Pa, and 100 Pa (uniform pressure increases) and secondly by applying pressure as 25 Pa, 30 Pa, 50 Pa, 60 Pa, 75 Pa, 83 Pa, and 100 Pa (non-uniform pressure increases). With the same boundary conditions and with different values of pressure, all the simulations for the finite element boundary value problem were run one by one in ABAQUS. After the simulations were completed, corresponding displacements were extracted from the ABAQUS results. Next, the MATLAB algorithm was run for multiple steps (4 steps and 7 steps for the first and the second case, respectively) using the pressure increases with their corresponding deformation. Subsequently, the material parameters were computed using the residual vectors from the multiple steps (4 steps for the uniform pressure increases and 7 steps for the non-uniform pressure increases) thus optimizing the difference between the internal forces corresponding to the myocardium deformation and the external forces due to the applied pressure on the endocardial surface.

For the material parameters C_{10} and D_1, the same values were used in all ABAQUS simulations. The normalized percent differences in material parameters between the exact values used in ABAQUS and the ones computed in the MATLAB algorithm are reported in Table 5.3. As can be seen, the implemented MATLAB algorithm was again successful in recovering both material parameters in all the cases.

Table 5.3: Normalized percent differences Δ in material parameters identified using the proposed pipeline versus the exact values used in the ABAQUS simulations using multi-pressure steps. The small differences in identified versus original parameters again confirm the verification of the proposed pipeline.

Step	ΔC_{10} [%]	ΔD_1 [%]
1	0	0.03
4	-0.2	0.16
7	-0.1	0.15

Computation of the material parameters describing the passive myocardium

Following the verification of the implemented pipeline, the MATLAB algorithm was used to compute the material parameters governing passive myocardium response using the preclinical (swine) MRI and pressure experimental data. The algorithm was applied to the finite element models constructed as described in the section 'LV mid-ventricular models and intraventricular pressure load during atrial systole' (chapter 5) and including the microstructure information to model the myocardium anisotropic response. The material model shown in Eq. 5.7 and proposed in [115] was used throughout this process. The MATLAB algorithm was executed to minimize the difference between the external and internal forces for each subject (N=8 subjects, S1 through S8). The material properties α_1 and α_2 determined for each subject are reported in Table 5.4 and are associated with the isotropic and anisotropic response, respectively.

Table 5.4: Material properties α_1 and α_2 describing the passive myocardium material response computed using the material model in Eq. 5.7, the mid-ventricular finite element models based on DENSE and cDTI data, and the intraventricular pressure recorded during the imaging experiments.

Subjects	α_1 (kPa)	α_2 (kPa)
S1	18.95	0.31
S2	4.07	0.25
S3	15.36	0.17
S4	3.79	0.16
S5	9.05	0.10
S6	7.87	0.31
S7	2.89	0.12
S8	2.27	0.03
Mean $\pm$ SD	8.03 ± 6.17	0.18 ± 0.1

Discussion

When modeling left ventricular mechanics through the Finite Element Method, ensuring the accuracy of geometric and microstructural data representation, coupled with selecting appropriate material models or constitutive laws, becomes very important for the reliability of the simulations. In the field of biomechanics, a variety of methodologies are employed to compute material properties by minimizing the difference between the experimental $\mathbf{u}_{\text{exp}}$ and computed $\mathbf{u}_{\text{num}}$ displacement fields under specified applied forces and boundary conditions [146, 80, 77]. Subsequently, material properties are iteratively adjusted to reduce deviations from experimental data. Nevertheless, conventional techniques may face challenges in achieving unique material

properties. To address this challenge, Perotti et al. [115] described an approach that utilizes experimental displacements to compute internal forces. This approach minimizes the difference between the external (or applied) and internal (due to body deformation) forces. This approach is part of the equilibrium gap method that has been previously described and proposed in the literature (see, e.g., [28]). This framework applies to instances with access to full-field measurements and traction boundary conditions.

Characterizing material properties at the tissue level offers advantages over traditional methods for assessing passive myocardium stiffness. Common estimates such as left ventricular pressure-volume (PV) loops provide a global chamber stiffness assessment and are not able to identify local changes in material stiffness or to distinguish between geometrical (e.g., due to hypertrophy) and physiological (e.g., due to scar formation) changes. However, PV-loop estimates are less susceptible to experimental noise, a problem that more severely affects estimates based on the calculation of the internal forces which require that the experimental displacement field is differentiated to compute deformation measures.

The material properties characterizing the isotropic and anisotropic response of the passive myocardium were computed using subject-specific anatomical, motion, and pressure data, the latter acquired concurrently with the imaging data. This unique set of experimental data allows an accurate representation of the passive myocardium response, in contrast to other studies that combine imaging data with pressure measures acquired at a different time and/or rule-based models.

After verifying the proposed pipeline using known ground-truth simulations obtained with ABAQUS, the passive myocardium material properties were identified for N=8 subjects. The mean value reported for the isotropic material property (α_1) of the passive myocardium is 8.03 $\pm$ 6.17 kPa and the mean value reported for the anisotropic (fiber-directed response, α_2) material

property of the passive myocardium is 0.18 ± 0.1 kPa.

These material properties agree reasonably well with other passive myocardium material properties reported in the literature. Several studies [107, 109, 139, 146, 103] use either the Guccione material model [62] or a Fung [51] type exponential material model to compute the passive myocardium material properties. To compare our findings with existing values, we report the coefficient that overall scales the passive myocardial response computed in these studies (see Table 5.5). The coefficient that overall scales the passive myocardial response in these studies ranges from 0.51 to 5.8 kPa.

Table 5.5: Coefficient that overall scales the passive myocardium material response estimated in several studies using different constitutive laws (SD reported where known).

Constitutive law	**Study and species**	Isotropic material parameter (kPa)
Guccione material model [62]	Wang et al. [147], human	1.2 ± 0.4
	Kolawole et al. [77], human	5.8 ± 1.2
	Augenstein et al. [6], dog	3
	Wang et al. [146], dog	0.83
	Usyk et al. [139], dog	0.88
	Omens et al. [109], dog	1.2
	Okamoto et al. [107], dog	0.51
	Omens et al. [109], rat	1.1
Fung type material model [51]	Nemavhola et al. [103], swine	3.47

In Table 5.5 we reported only the coefficient that overall scales the passive myocardial response in each of these studies. The material laws used in these studies define more than one parameter for the anisotropic material response and comparing these parameters directly with α_2 computed in this study is difficult given the different definitions of anisotropic terms and response.

Study Limitations and future work

The proposed method to identify material properties requires differentiating the displacement field and therefore may be more susceptible to propagating experimental noise. In the future, strategies to minimize the effect of displacement noise or the inclusion of other deformation measures, i.e., tag MRI, should be investigated.

In addition, we have not investigated the effect of uncertainty in material parameters associated with the subject-specific geometry and microstructural data. The effect of variability and experimental accuracy on the computed material properties needs to be evaluated.

Due to the complexity of this study, we have limited the model and the material property identification only to a midventricular section of the LV. Future studies can be undertaken to consider the full LV and, in the future, the RV as well. These studies require enhanced experimental data, especially to properly capture the LV basal and apical regions and the RV.

The current methodology also operates under the assumption of homogeneous material properties yielding an overall measure of the passive myocardium response. However, in the future, material properties and material behavior should be investigated regionally. This would allow us to identify regional dysfunction, for example, in the case of myocardial infarction.

Comparison of myocardial tissue anisotropy between different studies was not feasible at this time due to challenges associated with the identifiability of tissue anisotropy parameters in different material laws.

Finally, the cohort size used in this study was small (N=8 control subjects). Conducting investigations on a larger cohort in the future is necessary to improve the robustness of the findings.

CHAPTER 6: CONCLUSION

A Brief Summary with Novelty and Significance of the Work

Heart failure is a health challenge, impacting approximately 6.2 million adults in the USA [10]. This causes substantial healthcare costs, surpassing 11 billion annually, attributed to direct medical outlays and diminished productivity[10]. Such figures underscore the importance of collaborative endeavors aimed at tackling the complex array of issues associated with heart failure. These efforts should encompass proactive measures in prevention and early detection, facilitating improved accessibility to treatment options.

The most commonly used clinical measures, such as left ventricular ejection fraction (LVEF), have limitations in quantifying regional changes and primarily reflect active myocardial response. Myocardial deformation imaging techniques, such as strain echocardiography, offer promise in evaluating cardiac function but are predominantly applied during ventricular systole, neglecting atrial systole when the myocardium response is mainly passive. In this context, a better understanding of the passive myocardium response is important to improve diagnosis and possible treatment for diastolic dysfunction and heart failure with preserved ejection fraction (HFpEF), which mostly affects the passive myocardium response. This study contributes to closing this knowledge gap by: 1) analyzing the LV pressure-volume (PV) loops and the end-diastolic pressure-volume relation (EDPVR); 2) studying cardiac deformation during atrial systole; and 3) Identifying the material properties to characterize the passive myocardium response by optimizing the equilibrium between external (i.e., LV pressure) and internal forces (due to the myocardium deformation). The latter effort combines the knowledge developed in the first two goals of this thesis, i.e., pressure and deformation during atrial systole.

To accomplish the first objective, data from the subject groups control and MI were used. Computing the EDPVR primarily involved the utilization of cardiac CINE MRI in conjunction with pressure data acquired via *in vivo* cardiac catheterization. Intraventricular pressure measurements were continuously recorded throughout the MRI data acquisition process. Additionally, *ex vivo* T1 weighted images were employed to quantify the percentage of infarct in each subject within the myocardial infarction (MI) group, serving as a validation component for the proposed end-diastolic pressure-volume relationship (EDPVR) model. First, *in vivo* pressure-volume loops were built. Leveraging high-resolution data and a robust processing pipeline, the pressure-volume (PV) loops constructed for this study displayed all the classical characteristics of traditional PV loops, including distinguishable phases like an isovolumetric contraction, ejection, isovolumetric relaxation, and ventricular filling. Notably, our PV loops also showed the presence of the ”atrial kick,” further supporting the high quality of the computed PV loops. Next, the proposed models for the end-diastolic pressure-volume relations (EDPVR) showed the capability to identify statistically significant differences in increased LV chamber stiffness between the control and MI groups. In our study, subjects with myocardial infarction (MI) exhibited diverse shifts in their end-diastolic pressure-volume relationship (EDPVR), reflecting heterogeneous myocardial responses to MI. The reported variations underscore the individual influence of factors such as infarct size and location on myocardial remodeling. By normalizing pressure and volume and comparing EDPVR curves between control and MI groups, we revealed differences in diastolic chamber stiffness independent of absolute values where we reported a steeper slope observed in the MI group's EDPVR curve suggesting altered diastolic function post-MI. The findings highlight the complex interplay between myocardial remodeling and altered diastolic properties following MI. We also presented statistically significant correlations between the identified chamber stiffness coefficient (β) from the proposed EDPVR model and important LV systolic and diastolic indices like ventricular-arterial coupling (VAC), maximum rate of pressure decline during diastole ($dPdt_{min}$), LV relaxation time constant (τ),

isovolumic relaxation time (IVRT), diastolic volume recovery time (DVRT), and maximum rate of increase in volume during diastole ($dVdt_{max}$).

The proposed end-diastolic pressure-volume relation directly links a single coefficient (β) and the chamber stiffness (dPdV). Furthermore, by using normalized volume and pressure, differences between control and MI groups are observable more clearly and are independent of, e.g., ventricle size. Thus, the resulting model has the potential to better approximate the experimental data and to provide a direct measure of the chamber stiffness.

For the second objective, data from the subject group control and MI were again used. The methodology primarily involved the use of cardiac CINE DENSE MRI in conjunction with pressure data acquired via *in vivo* cardiac catheterization. As already mentioned, intraventricular pressure measurements were continuously recorded throughout the MRI data acquisition process. Cardiac cine DENSE MRI data was used to quantify cardiac deformations during atrial systole. A custom MATLAB code synchronized pressure and deformation mapping concurrently, marking this study as among the few to integrate concurrent pressure and MRI data. The synchronization ensured the alignment of intraventricular pressure, and displacements or deformations during atrial systole. Simultaneous display of intraventricular pressure with synchronized longitudinal, circumferential, and radial strains (E_{LL}, E_{CC}, E_{RR}) during atrial systole illustrated the changes occurring during atrial systole to the LV wall. In response to the increased pressure during atrial systole and due to the myocardium passive response, the LV elongates – (corresponding to positive longitudinal strains – and the LV wall becomes thinner – corresponding to positive circumferential strains and negative radial strain. Mean peak atrial systolic strains and strain rates were evaluated using the AHA segments, revealing significant differences between control and MI groups in circumferential and longitudinal strains. However, radial strains did not show significant differences. This may be also due to the difficulty in computing radial strains accurately using DENSE MRI data. Our findings align with studies reporting reduced ventricular

strain in MI patients compared to healthy individuals, though some studies report no significant differences as well.

Our study quantifying strains during atrial systole is among the few to do so and sheds light on the kinematics corresponding to the passive myocardium response.

For the final objective, data from the subject group control was used. The methodology primarily involved the use of cardiac CINE DENSE MRI in conjunction with pressure data acquired via *in vivo* cardiac catheterization continuously recorded throughout the MRI data acquisition process. Additionally, *ex vivo* cDTI images were used to extract cardiac microstructural data. The study incorporates both DENSE MRI and cDTI data to construct anatomically and microstructural accurate mid-ventricular finite element models. The constructed pipeline to identify the material properties was validated using known solutions computed in ABAQUS. After validating the method, we utilized a MATLAB algorithm to compute the material properties of the passive myocardium and characterize the passive myocardium response. This approach optimized differences between internal (due to cardiac deformations) and external forces (due to LV intraventricular pressure). The isotropic and anisotropic material properties were determined for each subject and reported. The coefficients that overall scale the passive myocardium stiffness reported across different studies using various material models were also reported and compared with the newly computed properties, showing overall agreement. It is worth noting that the overall passive myocardial stiffness parameters are derived from various constitutive laws and thus we exclude comparison of anisotropic properties due to the different parameter definitions.

This study computed passive myocardium material properties by enforcing equilibrium between internal and applied forces. The passive myocardium material properties were uniquely identified and characterized the passive myocardium behavior using pressure and deformation data acquired concurrently and patient-specific microstructural data. These material properties have the potential

to better describe the passive myocardium response and could improve the passive myocardium modeling. Furthermore, the use of the proposed pipeline with preclinical data paves the way for future extensions of this methodology to measure passive myocardium properties using patient data.

Suggestions for Future Work

In the following, we summarize a few key limitations of the presented work, offering a few suggestions for future studies.

Cohort Size

The overall cohort size used in this study representing both control and MI subjects was small. Future research to include a larger cohort is important to improve statistical significance, aiding in detecting subtle yet significant effects.

Infarct Size and Location

Variations in infarct size and location within the MI subject group may arise from differences in the chosen artery for infarction induction. Specifically, during the procedure, MI was induced in branches of either the left anterior descending (LAD) or left circumflex (LCx) artery. These differences can affect the remodeling process and therefore the passive myocardial stiffness and EDPVR curve shifts. Subsequent investigations are needed to assess the impact of inducing MI in the same artery versus different arteries.

Segment-wise Strain Quantification

This study aimed to quantify strains across various infarcted regions and AHA segments. Healthy myocardium shows distinct strain patterns reflecting optimal function, whereas strain values decreased significantly in infarcted tissue post-MI due to scar formation. However, by reporting

strain values averaged over AHA regions in MI subjects, values in healthy and infarcted myocardium are, in part, likely mixed. A better approach consists of carefully delineating infarcted regions and reporting strain values only for those regions, not the standard AHA regions. This would require further image segmentation and registration, including both rigid and non-rigid components.

Method for Region-based Material Property Identification Using Whole Heart Models

This study assumed homogeneous material laws for the LV mid-ventricular section, providing an average measure of the passive isotropic and anisotropic myocardium material response. Further studies should include regional material properties to identify localized heterogeneities in both health and disease, e.g., due to MI.

LIST OF REFERENCES

[1] Joana Afonso and Flávio Reis. Dexmedetomidine: current role in anesthesia and intensive care. *Revista brasileira de anestesiologia*, 62:125–133, 2012.

[2] Anthony H Aletras, Shujun Ding, Robert S Balaban, and Han Wen. Dense: displacement encoding with stimulated echoes in cardiac functional mri. *Journal of magnetic resonance (San Diego, Calif.: 1997)*, 137(1):247, 1999.

[3] Mads J Andersen, Mads Ersbøll, John Bro-Jeppesen, Finn Gustafsson, Christian Hassager, Lars Køber, Barry A Borlaug, Søren Boesgaard, Jasper Kjærgaard, and Jacob E Møller. Exercise hemodynamics in patients with and without diastolic dysfunction and preserved ejection fraction after myocardial infarction. *Circulation: Heart Failure*, 5(4):444–451, 2012.

[4] Francesco Antonini-Canterin, Roxana Enache, Bogdan Alexandru Popescu, Andreea Catarina Popescu, Carmen Ginghina, Elisa Leiballi, Rita Piazza, Daniela Pavan, Daniela Rubin, Piero Cappelletti, et al. Prognostic value of ventricular-arterial coupling and b-type natriuretic peptide in patients after myocardial infarction: a five-year follow-up study. *Journal of the American Society of Echocardiography*, 22(11):1239–1245, 2009.

[5] Hidetsugu Asanoi, Shigetake Sasayama, and Tomoki Kameyama. Ventriculoarterial coupling in normal and failing heart in humans. *Circulation research*, 65(2):483–493, 1989.

[6] Kevin F Augenstein, Brett R Cowan, Ian J LeGrice, Poul MF Nielsen, and Alistair A Young. Method and apparatus for soft tissue material parameter estimation using tissue tagged magnetic resonance imaging. *J. Biomech. Eng.*, 127(1):148–157, 2005.

[7] Reza Avazmohammadi, João S Soares, David S Li, Samarth S Raut, Robert C Gorman, and Michael S Sacks. A contemporary look at biomechanical models of myocardium. *Annual review of biomedical engineering*, 21:417–442, 2019.

[8] Daniel Balzani, Patrizio Neff, Jörg Schröder, and Gerhard A Holzapfel. A polyconvex framework for soft biological tissues. adjustment to experimental data. *International journal of solids and structures*, 43(20):6052–6070, 2006.

[9] J Bardet, P Rocha, M Rigaud, JP Bourdarias, and A Mathivat. Left ventricular compliance in acute myocardial infarction in man. *Cardiovascular Research*, 11(2):122–131, 1977.

[10] Aakash Bavishi and Ravi B Patel. Addressing comorbidities in heart failure: hypertension, atrial fibrillation, and diabetes. *Heart failure clinics*, 16(4):441–456, 2020.

[11] Javier Bermejo, Raquel Yotti, Candelas Pérez del Villar, Juan C del Álamo, Daniel Rodríguez-Pérez, Pablo Martínez-Legazpi, Yolanda Benito, J Carlos Antoranz, M Mar Desco, Ana González-Mansilla, et al. Diastolic chamber properties of the left ventricle assessed by global fitting of pressure-volume data: improving the gold standard of diastolic function. *Journal of Applied Physiology*, 115(4):556–568, 2013.

[12] Donald M Bers. Cardiac excitation–contraction coupling. *Nature*, 415(6868):198–205, 2002.

[13] S Bezy, A Caenen, J Duchenne, M Orlowska, M Amoni, A Puvrez, J D" hooge, and JU Voigt. Myocardial stiffness assessed by shear wave elastography relates to pressure-volume loop derived measurements of chamber stiffness. *European Heart Journal-Cardiovascular Imaging*, 23(Supplement_1):jeab289–169, 2022.

[14] Tor Biering-Sørensen, Soren Hoffmann, Rasmus Mogelvang, Allan Zeeberg Iversen, Søren Galatius, Thomas Fritz-Hansen, Jan Bech, and Jan Skov Jensen. Myocardial strain analysis

by 2-dimensional speckle tracking echocardiography improves diagnostics of coronary artery stenosis in stable angina pectoris. *Circulation: Cardiovascular Imaging*, 7(1):58–65, 2014.

[15] Attila Borbély, Jolanda Van Der Velden, Zoltán Papp, Jean GF Bronzwaer, Istvan Edes, Ger JM Stienen, and Walter J Paulus. Cardiomyocyte stiffness in diastolic heart failure. *Circulation*, 111(6):774–781, 2005.

[16] Barry A Borlaug, Carolyn SP Lam, Véronique L Roger, Richard J Rodeheffer, and Margaret M Redfield. Contractility and ventricular systolic stiffening in hypertensive heart disease: insights into the pathogenesis of heart failure with preserved ejection fraction. *Journal of the American College of Cardiology*, 54(5):410–418, 2009.

[17] Boston University School of Public Health. PH709 Module 2: Anatomy and Function of the Heart, n.d. Accessed on April 4, 2024. Available at: `https://sphweb.bumc.bu.edu/otlt/mph-modules/ph/ph709_heart/ph709_heart2.html`.

[18] Daniel Burkhoff. Pressure-volume loops in clinical research: a contemporary view, 2013.

[19] Daniel Burkhoff, Israel Mirsky, and Hiroyuki Suga. Assessment of systolic and diastolic ventricular properties via pressure-volume analysis: a guide for clinical, translational, and basic researchers. *American Journal of Physiology-Heart and Circulatory Physiology*, 289(2):H501–H512, 2005.

[20] Annette Caenen, Lana Keijzer, Stéphanie Bézy, Jürgen Duchenne, Marta Orlowska, Antonius FW Van Der Steen, Nico De Jong, Johan G Bosch, Jens-Uwe Voigt, Jan D'hooge, et al. Continuous shear wave measurements for dynamic cardiac stiffness evaluation in pigs. *Scientific Reports*, 13(1):17660, 2023.

[21] Kenneth S Campbell and Vincent L Sorrell. Cell-and molecular-level mechanisms contributing to diastolic dysfunction in hfpef. *Journal of Applied Physiology*, 119(10):1228–1232, 2015.

[22] Chen-Huan Chen, Barry Fetics, Erez Nevo, Carlos E Rochitte, Kuan-Rau Chiou, PhillipYu-An Ding, Miho Kawaguchi, and David A Kass. Noninvasive single-beat determination of left ventricular end-systolic elastance in humans. *Journal of the American College of Cardiology*, 38(7):2028–2034, 2001.

[23] Xiaorong Chen, Hongjie Hu, Yue Qian, and Jiner Shu. Relation of late gadolinium enhancement in cardiac magnetic resonance on the diastolic volume recovery of left ventricle with hypertrophic cardiomyopathy. *Journal of Thoracic Disease*, 6(7):988, 2014.

[24] Shahryar M Chowdhury, Ryan J Butts, Anthony M Hlavacek, Carolyn L Taylor, Karen S Chessa, Varsha M Bandisode, Girish S Shirali, Arni Nutting, and G Hamilton Baker. Echocardiographic detection of increased ventricular diastolic stiffness in pediatric heart transplant recipients: a pilot study. *Journal of the American Society of Echocardiography*, 31(3):342–348, 2018.

[25] Charles S Chung, Julius Bogomolovas, Alexander Gasch, Carlos G Hidalgo, Siegfried Labeit, and Henk L Granzier. Titin-actin interaction: Pevk-actin-based viscosity in a large animal. *Journal of Biomedicine and Biotechnology*, 2011, 2011.

[26] Charles S Chung, Kirk R Hutchinson, Mei Methawasin, Chandra Saripalli, John E Smith III, Carlos G Hidalgo, Xiuju Luo, Siegfried Labeit, Caiying Guo, and Henk L Granzier. Shortening of the elastic tandem immunoglobulin segment of titin leads to diastolic dysfunction. *Circulation*, 128(1):19–28, 2013.

[27] Charles S Chung, Methajit Methawasin, O Lynne Nelson, Michael H Radke, Carlos G Hidalgo, Michael Gotthardt, and Henk L Granzier. Titin based viscosity in ventricular

physiology: an integrative investigation of pevk–actin interactions. *Journal of molecular and cellular cardiology*, 51(3):428–434, 2011.

[28] Damien Claire, François Hild, and Stéphane Roux. A finite element formulation to identify damage fields: the equilibrium gap method. *International journal for numerical methods in engineering*, 61(2):189–208, 2004.

[29] Tyler E Cork, Luigi E Perotti, Ilya A Verzhbinsky, Michael Loecher, and Daniel B Ennis. High-resolution ex vivo microstructural mri after restoring ventricular geometry via 3d printing. In *Functional Imaging and Modeling of the Heart: 10th International Conference, FIMH 2019, Bordeaux, France, June 6–8, 2019, Proceedings 10*, pages 177–186. Springer, 2019.

[30] Philip A Corrado, Jacob A Macdonald, Christopher J François, Niti R Aggarwal, Jonathan W Weinsaft, and Oliver Wieben. Reduced regional flow in the left ventricle after anterior acute myocardial infarction: a case control study using 4d flow mri. *BMC Medical Imaging*, 19(1):1–10, 2019.

[31] Hussam M Daghistani, Bodour S Rajab, and Ashraf Kitmitto. Three-dimensional electron microscopy techniques for unravelling mitochondrial dysfunction in heart failure and identification of new pharmacological targets. *British Journal of Pharmacology*, 176(22):4340–4359, 2019.

[32] Dassault Systèmes Simulia Corp. Abaqus, 2021.

[33] Pieter P de Tombe. Cardiac myofilaments: mechanics and regulation. *Journal of biomechanics*, 36(5):721–730, 2003.

[34] PIETER P De Tombe, STEVEN Jones, DANIEL Burkhoff, WILLIAM C Hunter, and DAVID A Kass. Ventricular stroke work and efficiency both remain nearly optimal

despite altered vascular loading. *American Journal of Physiology-Heart and Circulatory Physiology*, 264(6):H1817–H1824, 1993.

[35] Linda L Demer and FC Yin. Passive biaxial mechanical properties of isolated canine myocardium. *The Journal of physiology*, 339(1):615–630, 1983.

[36] Shannon M Dunlay, Veronique L Roger, and Margaret M Redfield. Epidemiology of heart failure with preserved ejection fraction. *Nature Reviews Cardiology*, 14(10):591–602, 2017.

[37] Thor Edvardsen, Boaz D Rosen, Li Pan, Michael Jerosch-Herold, Shenghan Lai, W Gregory Hundley, Shantanu Sinha, Richard A Kronmal, David A Bluemke, and João AC Lima. Regional diastolic dysfunction in individuals with left ventricular hypertrophy measured by tagged magnetic resonance imaging—the multi-ethnic study of atherosclerosis (mesa). *American heart journal*, 151(1):109–114, 2006.

[38] Ramona Emig, Callum M Zgierski-Johnston, Viviane Timmermann, Andrew J Taberner, Martyn P Nash, Peter Kohl, and Rémi Peyronnet. Passive myocardial mechanical properties: meaning, measurement, models. *Biophysical Reviews*, pages 1–24, 2021.

[39] Mads Ersbøll, Mads J Andersen, Nana Valeur, Ulrik M Mogensen, Yama Fahkri, Jens J Thune, Jacob E Møller, Christian Hassager, Peter Søgaard, and Lars Køber. Early diastolic strain rate in relation to systolic and diastolic function and prognosis in acute myocardial infarction: a two-dimensional speckle-tracking study. *European heart journal*, 35(10):648–656, 2014.

[40] Zhi You Fang, Rodel Leano, and Thomas H Marwick. Relationship between longitudinal and radial contractility in subclinical diabetic heart disease. *Clinical science*, 106(1):53–60, 2004.

[41] ZY Fang, R Schull-Meade, M Downey, J Prins, and TH Marwick. Determinants of subclinical diabetic heart disease. *Diabetologia*, 48:394–402, 2005.

[42] Franz Faul, Edgar Erdfelder, Albert-Georg Lang, and Axel Buchner. G* power 3: A flexible statistical power analysis program for the social, behavioral, and biomedical sciences. *Behavior research methods*, 39(2):175–191, 2007.

[43] Andriy Fedorov, Reinhard Beichel, Jayashree Kalpathy-Cramer, Julien Finet, Jean-Christophe Fillion-Robin, Sonia Pujol, Christian Bauer, Dominique Jennings, Fiona Fennessy, Milan Sonka, et al. 3d slicer as an image computing platform for the quantitative imaging network. *Magnetic resonance imaging*, 30(9):1323–1341, 2012.

[44] Thomas A Foley, Sunil V Mankad, Nandan S Anavekar, Crystal R Bonnichsen, Michael F Morris, Todd D Miller, and Philip A Araoz. Measuring left ventricular ejection fraction–techniques and potential pitfalls. *Eur Cardiol*, 8(2):108–114, 2012.

[45] Gregory M Fomovsky, Stavros Thomopoulos, and Jeffrey W Holmes. Contribution of extracellular matrix to the mechanical properties of the heart. *Journal of molecular and cellular cardiology*, 48(3):490–496, 2010.

[46] National Center for Health Statistics et al. National vital statistics system: public use data file documentation: mortality multiple cause-of-death micro-data files, 2017. *Centers for Disease Control and Prevention website. https://www. cdc. gov/nchs/nvss/mortality_public_use_data. htm. Accessed April*, 1, 2019.

[47] James S Forrester, George Diamond, William W Parmley, HJC Swan, et al. Early increase in left ventricular compliance after myocardial infarction. *The Journal of clinical investigation*, 51(3):598–603, 1972.

[48] Pieter R Fourie, André R Coetzee, and Chris T Bolliger. Pulmonary artery compliance: its role in right ventricular-arterial coupling. *Cardiovascular research*, 26(9):839–844, 1992.

[49] Bianca Freytag, Vicky Y Wang, Debbie Zhao, Kathleen Gilbert, Gina Quill, Abdallah I Hasaballa, Thiranja P Babarenda Gamage, Robert N Doughty, Malcolm E Legget, Peter Ruygrok, et al. In vivo pressure-volume loops and chamber stiffness estimation using real-time 3d echocardiography and left ventricular catheterization–application to post-heart transplant patients. In *International Conference on Functional Imaging and Modeling of the Heart*, pages 396–405. Springer, 2021.

[50] Hidekatsu Fukuta and William C Little. The cardiac cycle and the physiologic basis of left ventricular contraction, ejection, relaxation, and filling. *Heart failure clinics*, 4(1):1–11, 2008.

[51] Yuan Cheng Fung. What are the residual stresses doing in our blood vessels? *Annals of biomedical engineering*, 19:237–249, 1991.

[52] WILLIAM H GAAscH, WILLIAM E BATTLE, ALLEN A OBOLER, JOHN S BANAS JR, and HERBERT J LEVINE. Left ventricular stress and compliance in man: with special reference to normalized ventricular function curves. *Circulation*, 45(4):746–762, 1972.

[53] WILLIAXi H Gaasch, JAMES S Cole, Miguel A Quiñones, and JK Alexander. Dynamic determinants of letf ventricular diastolic pressure-volume relations in man. *Circulation*, 51(2):317–323, 1975.

[54] Jin Kyu Gahm, Nicholas Wisniewski, Gordon Kindlmann, Geoffrey L Kung, William S Klug, Alan Garfinkel, and Daniel B Ennis. Linear invariant tensor interpolation applied to cardiac diffusion tensor mri. In *Medical Image Computing and Computer-Assisted Intervention–MICCAI 2012: 15th International Conference, Nice, France, October 1-5, 2012, Proceedings, Part II 15*, pages 494–501. Springer, 2012.

[55] Manuel Ignacio Monge García and Arnoldo Santos. Understanding ventriculo-arterial coupling. *Annals of Translational Medicine*, 8(12), 2020.

[56] Holly Geyer, Giuseppe Caracciolo, Haruhiko Abe, Susan Wilansky, Scipione Carerj, Federico Gentile, Hans-Joachim Nesser, Bijoy Khandheria, Jagat Narula, and Partho P Sengupta. Assessment of myocardial mechanics using speckle tracking echocardiography: fundamentals and clinical applications. *Journal of the American Society of Echocardiography*, 23(4):351–369, 2010.

[57] Derek G Gibson and Darrel P Francis. Clinical assessment of left ventricular diastolic function. *Heart*, 89(2):231–238, 2003.

[58] Andrew Gilliam and Jonathan Suever. denseanalysis/denseanalysis, 2020.

[59] St A Glantz and WW Parmley. Factors which affect the diastolic pressure-volume curve. *Circulation research*, 42(2):171–180, 1978.

[60] Henk L Granzier and Thomas C Irving. Passive tension in cardiac muscle: contribution of collagen, titin, microtubules, and intermediate filaments. *Biophysical journal*, 68(3):1027–1044, 1995.

[61] WILLIAM GROSSMAN and LAMBERT P McLAURIN. Diastolic properties of the left ventricle. *Annals of internal medicine*, 84(3):316–326, 1976.

[62] Julius M Guccione, Andrew D McCulloch, and LK Waldman. Passive material properties of intact ventricular myocardium determined from a cylindrical model. 1991.

[63] Arthur C Guyton. Textbook of medical physiology. *Academic Medicine*, 36(5):556, 1961.

[64] Nazha Hamdani and Walter J Paulus. Myocardial titin and collagen in cardiac diastolic dysfunction: partners in crime, 2013.

[65] Einar Heiberg, Martin Ugander, Henrik Engblom, Matthias Gotberg, Goran K Olivecrona, David Erlinge, and Hakan Arheden. Automated quantification of myocardial infarction from mr images by accounting for partial volume effects: animal, phantom, and human study. *Radiology*, 246(2):581–588, 2008.

[66] Ulrike Herberg, Eva Gatzweiler, Thomas Breuer, and Johannes Breuer. Ventricular pressure–volume loops obtained by 3d real-time echocardiography and mini pressure wire—a feasibility study. *Clinical Research in Cardiology*, 102(6):427–438, 2013.

[67] Melanie P Heron. Deaths: leading causes for 2017. *National Vital Statistics Reports*, 68(6):1–113, 2019.

[68] Michinari Hieda and Yoichi Goto. Cardiac mechanoenergetics in patients with acute myocardial infarction: From pressure-volume loop diagram related to cardiac oxygen consumption. *Heart Failure Clinics*, 16(3):255–269, 2020.

[69] Brian D Hoit. Left ventricular diastolic function. *Critical care medicine*, 35(8):S340–S347, 2007.

[70] Gerhard A Holzapfel and Ray W Ogden. Constitutive modelling of passive myocardium: a structurally based framework for material characterization. *Philosophical Transactions of the Royal Society A: Mathematical, Physical and Engineering Sciences*, 367(1902):3445–3475, 2009.

[71] Avinash Kali, Ivan Cokic, Richard LQ Tang, Hsin-Jung Yang, Behzad Sharif, Eduardo Marbán, Debiao Li, Daniel S Berman, and Rohan Dharmakumar. Determination of location, size, and transmurality of chronic myocardial infarction without exogenous contrast media by using cardiac magnetic resonance imaging at 3 t. *Circulation: Cardiovascular Imaging*, 7(3):471–481, 2014.

[72] Hyun Kang. Sample size determination and power analysis using the g* power software. *Journal of educational evaluation for health professions*, 18, 2021.

[73] David A Kass. Assessment of diastolic dysfunction: invasive modalities. *Cardiology clinics*, 18(3):571–586, 2000.

[74] Keigo Kawaji, Noel CF Codella, Martin R Prince, Christopher W Chu, Aqsa Shakoor, Troy M LaBounty, James K Min, Rajesh V Swaminathan, Richard B Devereux, Yi Wang, et al. Automated segmentation of routine clinical cardiac magnetic resonance imaging for assessment of left ventricular diastolic dysfunction. *Circulation: Cardiovascular Imaging*, 2(6):476–484, 2009.

[75] Indu Khurana. Essentials of medical physiology. *Intia: Elsevier India*, 2008.

[76] Stefan Klotz, Marc L Dickstein, and Daniel Burkhoff. A computational method of prediction of the end-diastolic pressure–volume relationship by single beat. *Nature protocols*, 2(9):2152–2158, 2007.

[77] Fikunwa O Kolawole, Vicky Y Wang, Bianca Freytag, Michael Loecher, Tyler E Cork, Martyn P Nash, Ellen Kuhl, and Daniel B Ennis. Evaluating passive myocardial stiffness using in vivo cine, cdti, and tagged mri. In *International Conference on Functional Imaging and Modeling of the Heart*, pages 527–536. Springer, 2023.

[78] Attila Kovács, Attila Oláh, Árpád Lux, Csaba Mátyás, Balázs Tamás Németh, Dalma Kellermayer, Mihály Ruppert, Marianna Török, Lilla Szabó, Anna Meltzer, et al. Strain and strain rate by speckle-tracking echocardiography correlate with pressure-volume loop-derived contractility indices in a rat model of athlete's heart. *American Journal of Physiology-Heart and Circulatory Physiology*, 308(7):H743–H748, 2015.

[79] SJ Kovács Jr, B Barzilai, and JE Perez. Evaluation of diastolic function with doppler echocardiography: the pdf formalism. *American Journal of Physiology-Heart and Circulatory Physiology*, 252(1):H178–H187, 1987.

[80] Gaurav Krishnamurthy, Daniel B Ennis, Akinobu Itoh, Wolfgang Bothe, Julia C Swanson, Matts Karlsson, Ellen Kuhl, D Craig Miller, and Neil B Ingels Jr. Material properties of the ovine mitral valve anterior leaflet in vivo from inverse finite element analysis. *American Journal of Physiology-Heart and Circulatory Physiology*, 295(3):H1141–H1149, 2008.

[81] Sophie Lalande, Patrick J Mueller, and Charles S Chung. The link between exercise and titin passive stiffness. *Experimental physiology*, 102(9):1055–1066, 2017.

[82] Adelino F Leite-Moreira. Current perspectives in diastolic dysfunction and diastolic heart failure. *Heart*, 92(5):712–718, 2006.

[83] Andreas Lervik, Joanna Raszplewicz, Birgit Ranheim, Susanna Solbak, Simen F Toverud, and Henning A Haga. Dexmedetomidine or fentanyl? cardiovascular stability and analgesia during propofol-ketamine total intravenous anaesthesia in experimental pigs. *Veterinary anaesthesia and analgesia*, 45(3):295–308, 2018.

[84] Howard R Levin, Mehmet C Oz, Jonathan M Chen, Milton Packer, Eric A Rose, and Daniel Burkhoff. Reversal of chronic ventricular dilation in patients with end-stage cardiomyopathy by prolonged mechanical unloading. *Circulation*, 91(11):2717–2720, 1995.

[85] Martin M LeWinter and Henk Granzier. Cardiac titin: a multifunctional giant. *Circulation*, 121(19):2137–2145, 2010.

[86] Bo Li, Yingmin Liu, Christopher J Occleshaw, Brett R Cowan, and Alistair A Young. In-line automated tracking for ventricular function with magnetic resonance imaging. *JACC: Cardiovascular Imaging*, 3(8):860–866, 2010.

[87] Xinzhou Li, Luigi E Perotti, Jessica A Martinez, Sandra M Duarte-Vogel, Daniel B Ennis, and Holden H Wu. Real-time 3t mri-guided cardiovascular catheterization in a porcine model using a glass-fiber epoxy-based guidewire. *PloS one*, 15(2):e0229711, 2020.

[88] Kai Lin, Leng Meng, Jeremy D Collins, Varun Chowdhary, Michael Markl, and James C Carr. Reproducibility of cine displacement encoding with stimulated echoes (dense) in human subjects. *Magnetic resonance imaging*, 35:148–153, 2017.

[89] William C Little and Jae K Oh. Echocardiographic evaluation of diastolic function can be used to guide clinical care. *Circulation*, 120(9):802–809, 2009.

[90] Beverly H Lorell. Significance of diastolic dysfunction of the heart. *Annual review of medicine*, 42(1):411–436, 1991.

[91] MATLAB. *version 7.10.0 (R2010a)*. The MathWorks Inc., Natick, Massachusetts, 2010.

[92] Hiromi Matsubara, Miyako Takaki, Shingo Yasuhara, Junichi Araki, and Hiroyuki Suga. Logistic time constant of isovolumic relaxation pressure–time curve in the canine left ventricle: better alternative to exponential time constant. *Circulation*, 92(8):2318–2326, 1995.

[93] Mathew S Maurer, Daniel Spevack, Daniel Burkhoff, and Itzhak Kronzon. Diastolic dysfunction: can it be diagnosed by doppler echocardiography? *Journal of the American College of Cardiology*, 44(8):1543–1549, 2004.

[94] Robert J Mentz and Michel G Khouri. Longitudinal strain in heart failure with preserved ejection fraction: is there a role for prognostication?, 2015.

[95] Agata Milewska, Andrzej Minczykowski, Tomasz Krauze, Jarosław Piskorski, James Heathers, Adam Szczepanik, Agnieszka Banaszak, Przemyslaw Guzik, and Andrzej

Wykretowicz. Prognosis after acute coronary syndrome in relation with ventricular–arterial coupling and left ventricular strain. *International journal of cardiology*, 220:343–348, 2016.

[96] ISRAEL Mirsky. Assessment of diastolic function: suggested methods and future considerations. *Circulation*, 69(4):836–841, 1984.

[97] Hirokazu Miyoshi, Yukio Mizuguchi, Yoshifumi Oishi, Arata Iuchi, Norio Nagase, Nusrat Ara, and Takashi Oki. Early detection of abnormal left atrial–left ventricular–arterial coupling in preclinical patients with cardiovascular risk factors: evaluation by two-dimensional speckle-tracking echocardiography. *European Journal of Echocardiography*, 12(6):431–439, 2011.

[98] Hirokazu Miyoshi, Yoshifumi Oishi, Yukio Mizuguchi, Arata Iuchi, Norio Nagase, Nusrat Ara, and Takashi Oki. Association of left atrial reservoir function with left atrial structural remodeling related to left ventricular dysfunction in asymptomatic patients with hypertension: evaluation by two-dimensional speckle-tracking echocardiography. *Clinical and Experimental Hypertension*, 37(2):155–165, 2015.

[99] Yukio Mizuguchi, Yoshifumi Oishi, Hirokazu Miyoshi, Arata Iuchi, Norio Nagase, and Takashi Oki. The functional role of longitudinal, circumferential, and radial myocardial deformation for regulating the early impairment of left ventricular contraction and relaxation in patients with cardiovascular risk factors: a study with two-dimensional strain imaging. *Journal of the American Society of Echocardiography*, 21(10):1138–1144, 2008.

[100] Yukio Mizuguchi, Yoshifumi Oishi, Hirokazu Miyoshi, Arata Iuchi, Norio Nagase, and Takashi Oki. Concentric left ventricular hypertrophy brings deterioration of systolic longitudinal, circumferential, and radial myocardial deformation in hypertensive patients with preserved left ventricular pump function. *Journal of cardiology*, 55(1):23–33, 2010.

[101] Yngvar Myreng and Otto A Smiseth. Assessment of left ventricular relaxation by doppler echocardiography. comparison of isovolumic relaxation time and transmitral flow velocities with time constant of isovolumic relaxation. *Circulation*, 81(1):260–266, 1990.

[102] Marcelo S Nacif, Andre LC Almeida, Alistair A Young, Brett R Cowan, Anderson C Armstrong, Eunice Yang, Christopher T Sibley, W Gregory Hundley, Songtao Liu, Joao AC Lima, et al. Three-dimensional volumetric assessment of diastolic function by cardiac magnetic resonance imaging: the multi-ethnic study of atherosclerosis (mesa). *Arquivos brasileiros de cardiologia*, 108:552–563, 2017.

[103] Fulufhelo Nemavhola. Study of biaxial mechanical properties of the passive pig heart: material characterisation and categorisation of regional differences. *International Journal of Mechanical and Materials Engineering*, 16(1):6, 2021.

[104] Arnold CT Ng, Victoria Delgado, Matteo Bertini, Rutger W van der Meer, Luuk J Rijzewijk, Miriam Shanks, Gaetano Nucifora, Johannes WA Smit, Michaela Diamant, Johannes A Romijn, et al. Findings from left ventricular strain and strain rate imaging in asymptomatic patients with type 2 diabetes mellitus. *The American journal of cardiology*, 104(10):1398–1401, 2009.

[105] Amir Nikou, Shauna M Dorsey, Jeremy R McGarvey, Joseph H Gorman, Jason A Burdick, James J Pilla, Robert C Gorman, and Jonathan F Wenk. Computational modeling of healthy myocardium in diastole. *Annals of biomedical engineering*, 44(4):980–992, 2016.

[106] Leslie M Ogilvie, Brittany A Edgett, Jason S Huber, Mathew J Platt, Hermann J Eberl, Sohrab Lutchmedial, Keith R Brunt, and Jeremy A Simpson. Hemodynamic assessment of diastolic function for experimental models. *American Journal of Physiology-Heart and Circulatory Physiology*, 318(5):H1139–H1158, 2020.

[107] RJ Okamoto, MJ Moulton, SJ Peterson, D Li, MK Pasque, and JM Guccione. Epicardial suction: a new approach to mechanical testing of the passive ventricular wall. *J. Biomech. Eng.*, 122(5):479–487, 2000.

[108] A Afşin Oktay, Jonathan D Rich, and Sanjiv J Shah. The emerging epidemic of heart failure with preserved ejection fraction. *Current heart failure reports*, 10(4):401–410, 2013.

[109] Jeffrey H Omens, Deidre A MacKenna, and Andrew D McCulloch. Measurement of strain and analysis of stress in resting rat left ventricular myocardium. *Journal of biomechanics*, 26(6):665–676, 1993.

[110] American Heart Association Writing Group on Myocardial Segmentation, Registration for Cardiac Imaging:, Manuel D Cerqueira, Neil J Weissman, Vasken Dilsizian, Alice K Jacobs, Sanjiv Kaul, Warren K Laskey, Dudley J Pennell, John A Rumberger, Thomas Ryan, et al. Standardized myocardial segmentation and nomenclature for tomographic imaging of the heart: a statement for healthcare professionals from the cardiac imaging committee of the council on clinical cardiology of the american heart association. *Circulation*, 105(4):539–542, 2002.

[111] Seong-Mi Park, Abhiram Prasad, Charanjit Rihal, Malcolm R Bell, and Jae K Oh. Left ventricular systolic and diastolic function in patients with apical ballooning syndrome compared with patients with acute anterior st-segment elevation myocardial infarction: a functional paradox. In *Mayo Clinic Proceedings*, volume 84, pages 514–521. Elsevier, 2009.

[112] Ares Pasipoularides. Right and left ventricular diastolic pressure–volume relations: a comprehensive review. *Journal of Cardiovascular Translational Research*, 6(2):239–252, 2013.

[113] Hena N Patel, Tatsuya Miyoshi, Karima Addetia, Michael P Henry, Rodolfo Citro, Masao Daimon, Pedro Gutierrez Fajardo, Ravi R Kasliwal, James N Kirkpatrick, Mark J Monaghan, et al. Normal values of cardiac output and stroke volume according to measurement technique, age, sex, and ethnicity: results of the world alliance of societies of echocardiography study. *Journal of the American Society of Echocardiography*, 34(10):1077–1085, 2021.

[114] Walter J Paulus and Carsten Tschöpe. A novel paradigm for heart failure with preserved ejection fraction: comorbidities drive myocardial dysfunction and remodeling through coronary microvascular endothelial inflammation. *Journal of the American College of Cardiology*, 62(4):263–271, 2013.

[115] Luigi E Perotti, Aditya VS Ponnaluri, Shankarjee Krishnamoorthi, Daniel Balzani, Daniel B Ennis, and William S Klug. Method for the unique identification of hyperelastic material properties using full-field measures. application to the passive myocardium material response. *International journal for numerical methods in biomedical engineering*, 33(11):e2866, 2017.

[116] JANICE M Pfeffer, Marc A Pfeffer, PETER J Fletcher, and E Braunwald. Progressive ventricular remodeling in rat with myocardial infarction. *American Journal of Physiology-Heart and Circulatory Physiology*, 260(5):H1406–H1414, 1991.

[117] AVS Ponnaluri, LE Perotti, DB Ennis, and WS Klug. A viscoactive constitutive modeling framework with variational updates for the myocardium. *Computer methods in applied mechanics and engineering*, 314:85–101, 2017.

[118] Uwe Primessnig, Patrick Schönleitner, Alexander Höll, Susanne Pfeiffer, Taja Bracic, Thomas Rau, Martin Kapl, Tatjana Stojakovic, Toma Glasnov, Kirsten Leineweber, et al.

Novel pathomechanisms of cardiomyocyte dysfunction in a model of heart failure with preserved ejection fraction. *European journal of heart failure*, 18(8):987–997, 2016.

[119] Jose A Rosado-Toro, Ryan J Avery, Maria I Altbach, Franz Rischard, and Rebecca Vanderpool. Feasibility of mri-rhc based pressure volume loops in control and pah patients. *Circulation*, 136(suppl_1):A19444–A19444, 2017.

[120] Daniel Rueckert, Luke I Sonoda, Carmel Hayes, Derek LG Hill, Martin O Leach, and David J Hawkes. Nonrigid registration using free-form deformations: application to breast mr images. *IEEE transactions on medical imaging*, 18(8):712–721, 1999.

[121] KIICHI Sagawa. The ventricular pressure-volume diagram revisited. *Circulation Research*, 43(5):677–687, 1978.

[122] Kiichi Sagawa, Hiroyuki Suga, Artin A Shoukas, and Kenneth M Bakalar. End-systolic pressure/volume ratio: a new index of ventricular contractility. *The American journal of cardiology*, 40(5):748–753, 1977.

[123] Arnd Schaefer, Gunnar Klein, Birgit Brand, Peter Lippolt, Helmut Drexler, and Gerd Peter Meyer. Evaluation of left ventricular diastolic function by pulsed doppler tissue imaging in mice. *Journal of the American Society of Echocardiography*, 16(11):1144–1149, 2003.

[124] Dominik Schüttler, Philipp Tomsits, Christina Bleyer, Julia Vlcek, Valerie Pauly, Nora Hesse, Moritz Sinner, Daphne Merkus, Jules Hamers, Stefan Kääb, et al. A practical guide to setting up pig models for cardiovascular catheterization, electrophysiological assessment and heart disease research. *Lab Animal*, 51(2):46–67, 2022.

[125] Felicia Seemann, Per Arvidsson, David Nordlund, Sascha Kopic, Marcus Carlsson, Håkan Arheden, and Einar Heiberg. Noninvasive quantification of pressure-volume loops from

brachial pressure and cardiovascular magnetic resonance. *Circulation: Cardiovascular Imaging*, 12(1):e008493, 2019.

[126] Hideaki Senzaki, Chen-Huan Chen, and David A Kass. Single-beat estimation of end-systolic pressure-volume relation in humans: a new method with the potential for noninvasive application. *Circulation*, 94(10):2497–2506, 1996.

[127] Pia Sjöberg, Felicia Seemann, Hakan Arheden, and Einar Heiberg. Non-invasive quantification of pressure-volume loops from cardiovascular magnetic resonance at rest and during dobutamine stress. *Clinical physiology and functional imaging*, 2021.

[128] Otto A Smiseth, Hans Torp, Anders Opdahl, Kristina H Haugaa, and Stig Urheim. Myocardial strain imaging: how useful is it in clinical decision making? *European heart journal*, 37(15):1196–1207, 2015.

[129] Steven B Solomon, Paolo Barbier, and Stanton A Glantz. Changes in porcine transmitral flow velocity pattern and its diastolic determinants during partial coronary occlusion. *Journal of the American College of Cardiology*, 33(3):854–866, 1999.

[130] Bruce S Spottiswoode, Xiaodong Zhong, Aaron T Hess, CM Kramer, Ernesta M Meintjes, Bongani M Mayosi, and Frederick H Epstein. Tracking myocardial motion from cine dense images using spatiotemporal phase unwrapping and temporal fitting. *IEEE transactions on medical imaging*, 26(1):15–30, 2006.

[131] Mark R Starling. Left ventricular-arterial coupling relations in the normal human heart. *American heart journal*, 125(6):1659–1666, 1993.

[132] Kenji Sunagawa, W Lowell Maughan, and Kiichi Sagawa. Optimal arterial resistance for the maximal stroke work studied in isolated canine left ventricle. *Circulation research*, 56(4):586–595, 1985.

[133] Kiyohiro Takigiku, Masaaki Takeuchi, Chisato Izumi, Satoshi Yuda, Konomi Sakata, Nobuyuki Ohte, Kazuaki Tanabe, Satoshi Nakatani, JUSTICE investigators, et al. Normal range of left ventricular 2-dimensional strain–japanese ultrasound speckle tracking of the left ventricle (justice) study–. *Circulation Journal*, 76(11):2623–2632, 2012.

[134] Ellen A Ten Brinke, Daniel Burkhoff, Robert J Klautz, Carsten Tschöpe, Martin J Schalij, Jeroen J Bax, Ernst E van der Wall, Robert A Dion, and Paul Steendijk. Single-beat estimation of the left ventricular end-diastolic pressure–volume relationship in patients with heart failure. *Heart*, 96(3):213–219, 2010.

[135] Jens Jakob Thune and Scott D Solomon. Left ventricular diastolic function following myocardial infarction. *Current heart failure reports*, 3(4):170–174, 2006.

[136] Laurens F Tops, Victoria Delgado, Nina Ajmone Marsan, and Jeroen J Bax. Myocardial strain to detect subtle left ventricular systolic dysfunction. *European journal of heart failure*, 19(3):307–313, 2017.

[137] William M Torres, Julia Jacobs, Heather Doviak, Shayne C Barlow, Michael R Zile, Tarek Shazly, and Francis G Spinale. Regional and temporal changes in left ventricular strain and stiffness in a porcine model of myocardial infarction. *American Journal of Physiology-Heart and Circulatory Physiology*, 315(4):H958–H967, 2018.

[138] Mark L Trew, Bryan J Caldwell, Gregory B Sands, Darren A Hooks, Dean C-S Tai, Travis M Austin, Ian J LeGrice, Andrew J Pullan, and Bruce H Smaill. Cardiac electrophysiology and tissue structure: bridging the scale gap with a joint measurement and modelling paradigm. *Experimental physiology*, 91(2):355–370, 2006.

[139] TP Usyk, R Mazhari, and AD McCulloch. Effect of laminar orthotropic myofiber architecture on regional stress and strain in the canine left ventricle. *Journal of elasticity and the physical science of solids*, 61:143–164, 2000.

[140] Loek van Heerebeek, Nazha Hamdani, Inês Falcão-Pires, Adelino F Leite-Moreira, Mark PV Begieneman, Jean GF Bronzwaer, Jolanda van der Velden, Ger JM Stienen, Gerrit J Laarman, Aernout Somsen, et al. Low myocardial protein kinase g activity in heart failure with preserved ejection fraction. *Circulation*, 126(7):830–839, 2012.

[141] Ilya A Verzhbinsky, Luigi E Perotti, Kévin Moulin, Tyler E Cork, Michael Loecher, and Daniel B Ennis. Estimating aggregate cardiomyocyte strain using $i\tilde{n}vivo$ diffusion and displacement encoded mri. *IEEE transactions on medical imaging*, 39(3):656–667, 2019.

[142] José Carlos Villalobos Lizardi, Jerome Baranger, Minh B Nguyen, Atef Asnacios, Aimen Malik, Joost Lumens, Luc Mertens, Mark K Friedberg, Craig A Simmons, Mathieu Pernot, et al. A guide for assessment of myocardial stiffness in health and disease. *Nature Cardiovascular Research*, 1(1):8–22, 2022.

[143] Dragos Vinereanu, Eleftherios Nicolaides, Ann C Tweddel, Christoph K MÄDLER, Ben Holst, Lucy E Boden, Mircea Cinteza, Alan E Rees, and Alan G Fraser. Subclinical left ventricular dysfunction in asymptomatic patients with type ii diabetes mellitus, related to serum lipids and glycated haemoglobin. *Clinical Science*, 105(5):591–599, 2003.

[144] Jens-Uwe Voigt, Gianni Pedrizzetti, Peter Lysyansky, Tom H Marwick, Helen Houle, Rolf Baumann, Stefano Pedri, Yasuhiro Ito, Yasuhiko Abe, Stephen Metz, et al. Definitions for a common standard for 2d speckle tracking echocardiography: consensus document of the eacvi/ase/industry task force to standardize deformation imaging. *European Heart Journal-Cardiovascular Imaging*, 16(1):1–11, 2015.

[145] Jianwen Wang, Dirar S Khoury, Yong Yue, Guillermo Torre-Amione, and Sherif F Nagueh. Preserved left ventricular twist and circumferential deformation, but depressed longitudinal and radial deformation in patients with diastolic heart failure. *European heart journal*, 29(10):1283–1289, 2008.

[146] Vicky Y Wang, HI Lam, Daniel B Ennis, Brett R Cowan, Alistair A Young, and Martyn P Nash. Modelling passive diastolic mechanics with quantitative mri of cardiac structure and function. *Medical image analysis*, 13(5):773–784, 2009.

[147] Zhinuo J Wang, Vicky Y Wang, Chris P Bradley, Martyn P Nash, Alistair A Young, and J Jane Cao. Left ventricular diastolic myocardial stiffness and end-diastolic myofibre stress in human heart failure using personalised biomechanical analysis. *Journal of cardiovascular translational research*, 11(4):346–356, 2018.

[148] Gregory J Wehner, Linyuan Jing, Christopher M Haggerty, Jonathan D Suever, Jing Chen, Sean M Hamlet, Jared A Feindt, W Dimitri Mojsejenko, Mark A Fogel, and Brandon K Fornwalt. Comparison of left ventricular strains and torsion derived from feature tracking and dense cmr. *Journal of Cardiovascular Magnetic Resonance*, 20(1):1–11, 2018.

[149] Brian R Weil, George Techiryan, Gen Suzuki, Filip Konecny, and John M Canty. Adaptive reductions in left ventricular diastolic compliance protect the heart from stretch-induced stunning. *JACC: Basic to Translational Science*, 4(4):527–541, 2019.

[150] James L Weiss, James W Frederiksen, Myron L Weisfeldt, et al. Hemodynamic determinants of the time-course of fall in canine left ventricular pressure. *The Journal of clinical investigation*, 58(3):751–760, 1976.

[151] Dirk Westermann, Mario Kasner, Paul Steendijk, Frank Spillmann, Alexander Riad, Kerstin Weitmann, Wolfgang Hoffmann, Wolfgang Poller, Matthias Pauschinger, Heinz-Peter Schultheiss, et al. Role of left ventricular stiffness in heart failure with normal ejection fraction. *Circulation*, 117(16):2051–2060, 2008.

[152] Alexander J Wilson, Gregory B Sands, Ian J LeGrice, Alistair A Young, and Daniel B Ennis. Myocardial mesostructure and mesofunction. *American Journal of Physiology-Heart and Circulatory Physiology*, 323(2):H257–H275, 2022.

[153] Frank CP Yin, Robert K Strumpf, Paul H Chew, and Scott L Zeger. Quantification of the mechanical properties of noncontracting canine myocardium under simultaneous biaxial loading. *Journal of biomechanics*, 20(6):577–589, 1987.

[154] Alistair A Young, Brett R Cowan, Steven F Thrupp, Warren J Hedley, and Louis J Dell'Italia. Left ventricular mass and volume: fast calculation with guide-point modeling on mr images. *Radiology*, 216(2):597–602, 2000.

[155] Diana Zaliaduonyte-Peksiene, Jolanta Justina Vaskelyte, Vaida Mizariene, Renaldas Jurkevicius, and Remigijus Zaliunas. Does longitudinal strain predict left ventricular remodeling after myocardial infarction? *Echocardiography*, 29(4):419–427, 2012.

[156] Wei Zhang and Sándor J Kovács. The diastatic pressure-volume relationship is not the same as the end-diastolic pressure-volume relationship. *American Journal of Physiology-Heart and Circulatory Physiology*, 294(6):H2750–H2760, 2008.

[157] Michael R Zile, Catalin F Baicu, and William H Gaasch. Diastolic heart failure—abnormalities in active relaxation and passive stiffness of the left ventricle. *New England Journal of Medicine*, 350(19):1953–1959, 2004.

[158] Michael R Zile, Catalin F Baicu, John S. Ikonomidis, Robert E Stroud, Paul J Nietert, Amy D Bradshaw, Rebecca Slater, Bradley M Palmer, Peter Van Buren, Markus Meyer, et al. Myocardial stiffness in patients with heart failure and a preserved ejection fraction: contributions of collagen and titin. *Circulation*, 131(14):1247–1259, 2015.

[159] Michael R Zile and Dirk L Brutsaert. New concepts in diastolic dysfunction and diastolic heart failure: Part i: diagnosis, prognosis, and measurements of diastolic function. *Circulation*, 105(11):1387–1393, 2002.

[160] Michael R Zile and Dirk L Brutsaert. New concepts in diastolic dysfunction and diastolic heart failure: Part ii: causal mechanisms and treatment. *Circulation*, 105(12):1503–1508, 2002.